

People's Democratic and Popular Republic of Algeria

Ministry of Higher Education and Scientific Research

El-Hadj Lakhdar University of Batna

Faculty of Sciences

Department of matter science

Dissertation

Presented by

Faiza Si belkhir

In partial fulfillment of the requirements for the degree of Magister in Physics

Option: Astrophysics

Theme

Cosmic Ray Dosimetry

Jury Members:

Chairman:	Mr. A. BOULDJEDRI	Prof, University of Batna
Reporter:	Mr. R. ATTALLAH	Prof, University of Annaba
Examiners:	Mr. J. MIMOUNI	Prof, University of Constantine
	Mr. A. SID	M.C. University of Batna

République Algérienne Démocratique et Populaire
Ministère de l'Enseignement Supérieur et de la Recherche Scientifique

Faculté des Sciences
Département de Science la Matière

Mémoire

Présenté par

Faiza Si belkhir

En vue de l'obtention du Diplôme de Magistère en physique

Option: Astrophysique

Thème

Cosmic Ray Dosimetry

Devant le Jury :

Président :	Mr. A. BOULDJEDRI	Prof, Université of Batna
Rapporteur:	Mr. R. ATTALLAH	Prof, Université of Annaba
Examineurs:	Mr. J. MIMOUNI	Prof, Université of Constantine
	Mr. A. SID	M.C. Université of Batna

CONTENTS

List of figures	vi
List of tables	viii
Acknowledgments	x
Introduction	1

Chapter 1 Cosmic Rays

1.1. History	3
1.2. The main properties of cosmic rays	5
1.2.1. Composition	5
1.2.2. Energy spectrum	7
1.2.3. Isotropy	11
1.3. Origin and acceleration mechanisms	13
1.3.1. Acceleration mechanisms	14
1.3.2. Cosmic ray sources	18
1.4. Air shower	21
1.4.1. Electromagnetic shower	21
1.4.2. Hadronic shower	22
1.5. Detection of cosmic rays	25
1.5.1. Direct detection	25
1.5.2. Indirect detection	26

Chapter 2

Dosimetry

2.1. Introduction	31
2.2. Ionizing radiation	31
2.3. Biological effects of ionizing radiation	33
2.3.1. Stochastic effects	33
2.3.2. Deterministic effects	34
2.4. Dosimetric quantities and units	34
2.4.1. Physical quantities	35
2.4.2. Protection quantities	41
2.4.3. Operational quantities	43
2.5. Dosimetric methods	45
2.5.1. Ionizing method	47
2.5.2. Thermoluminescence method	49
2.5.3. Chemical method	51
2.5.4. Calorimetric method	52

Chapter 3

Cosmic ray dosimetry

3.1. Cosmic ray spectra in the atmosphere.	55
3.1.1. Neutron spectra	60
3.1.2. Proton and helium ion spectra	64
3.1.3. Electron, positron and photon spectra	70
3.1.4. Secondary muon spectra	71
3.2. Cosmic ray dosimetry in the atmosphere.	78

3.2.1. Fluence to dose conversion coefficients.	78
3.2.2. Cosmic ray dosimetry at ground level	79
3.2.3. Cosmic ray dosimetry at high altitude.	80
3.2.4. Comparison between the experimental and calculated data	84
Conclusion	93
Bibliography	94

List of figures

Chapter 1

- 1.1 Relative abundances of primary cosmic rays for $1 \leq Z \leq 100$.
- 1.2 Energy spectrum of all particles primary cosmic rays.
- 1.3 Modulation of primary spectrum by the 11-year cycle of the sun.
- 1.4 Energy spectrum of primary cosmic rays scaled by a factor E^3 .
- 1.5 Sources directions of UHECRs measured by AGASA.
- 1.6 Map in galactic coordinates with the positions of the AGNs within 71 Mpc (stars) and the 27 events with $E > 57$ EeV (circles of 3.2° radius). Shading indicates regions of equal exposure.
- 1.7 Sketch of a collision of a charged particle with moving magnetic cloud.
- 1.9 Pulsar of Crab. This image is a composition of images optical (red) and X (blue), observed respectively by the space telescope Hubble and the Chandra observatory.
- 1.10 Schematic view of the creation of electromagnetic shower in the atmosphere.
- 1.11 Schematic view of the creation of hadronic shower in the atmosphere.
- 1.12 Vertical fluxes of cosmic rays in the atmosphere with $E > 1$ GeV.
- 1.13 Detection of γ -ray through Cerenkov radiation.
- 1.14 One telescope of HESS experiment.
- 1.15 KASCADE experiment.
- 1.16 Pierre Auger Observatory array in the Argentinean Pampa.

Chapter 2

- 2.1 Schema of a gas filled detector.
- 2.2 Typical behavior at atmospheric pressure for a gas-filled counter.

- 2.3 Schematic illustration of processes of produced in the crystal by irradiation and a successive heat treatment.
- 2.4 Thermoluminescence glow curve of LiF phosphor activated with trace amounts of Mg^{+2} and Ti^{+4} (TLD-100).

Chapter 3

- 3.1 The cosmic ray neutron spectra obtained by our program. The left and right panels show the atmospheric depth and cut-off rigidity dependence of the spectra, respectively.
- 3.2 The cosmic ray proton and helium ion spectra obtained by our program. The left and right panels show the atmospheric depth and the cut-off rigidity dependence of the spectra, respectively.
- 3.3 The cosmic ray electron, positron and photon obtained by our program. The left and right panels show the atmospheric depth and cut-off rigidity dependence of the spectra, respectively.
- 3.4 The cosmic ray muon spectra obtained by our program. The left and right panels show the atmospheric depth and cut-off rigidity dependence of the spectra, respectively.
- 3.5 Effective dose rate of different places for solar minimum and maximum conditions at ground level.
- 3.6 Average yearly Exposure to Ionizing Radiation.
- 3.7 Calculated ambient dose equivalent rate, $dH^*(10)/dt$, for conditions close to solar maximum activity (December.1999) and close to solar minimum (December. 2009), both at equator and pole regions.
- 3.8 Effective dose rate as a function of altitude.
- 3.9 Ambient dose equivalent rate as a function of vertical cut off rigidity r_c between May 1992 and May 2003 for altitude 10668 m.
- 3.10 Ambient dose equivalent rate as a function of vertical cut off rigidity r_c between May 1992 and May 2003 for altitude 11277 m.
- 3.11 Ambient dose equivalent rate as a function of vertical cut off rigidity r_c between May 1992 and May 2003 for altitude 11887 m.

- 3.12 Ambient dose equivalent rate as a function of altitude d between May 1992 and May 2003 for vertical cut off rigidity $r_c \leq 2$ GV.
- 3.13 Ambient dose equivalent rate as a function of altitude d between May 1992 and May 2003 for vertical cut off rigidity $r_c \geq 12$ GV.
- 3.14 Ambient neutron dose equivalent rate as a function of altitude d in comparison with measured data of Kawatari et al.

List of tables

Chapter 2

- 2.1 Radiation weighting factors w_R
- 2.2 Recommended tissue weighting factors.

Chapter 3

- 3.1 Numerical values of the parameters b^2
- 3.2 Numerical values of the parameters c
- 3.3 Numerical values of the parameters a and b .
- 3.4 Numerical values of the parameters g
- 3.5 Numerical values of the parameters h
- 3.6 Numerical values of the parameters a_i ($i = 1, 2, \dots, 16$).
- 3.7 Numerical values of the parameters c
- 3.8 Numerical values of the parameters h used in Eq (3.7) for expressing the cut-off rigidity dependence of the g data.
- 3.9 Numerical values of the parameters u_i , w_{ijk} and h_{ij} used in Eqs. (3.33), (3.32) and (3.7), respectively, to estimate the atmospheric muon spectra.

Acknowledgements

First and foremost all praise and thanks go to Allah, who has given me the strength and blessings to complete this work.

I am sincerely and heartily grateful to my teacher and advisor, Reda Attallah, for the support and guidance he showed me throughout my dissertation writing. I am sure it would have not been possible without his help.

I particularly grateful to professors: Mimouni, Bouldjedri and Seghouani who oversaw on the establishment of EDA and its organization. I wish to thank all teachers of EDA: Abdellatif, sid, kahlouche, Benslama, Mebarki, and those who came to teach us from outside Algeria.

I am also thankful to Mr. Sato Tatsuhiko, Japan Atomic Energy Agency, without his corporation I could not have gotten such relevant data.

I would like to show my gratitude to Abderrahmane Zoghbi, University of Cambridge, and Ali Behloul, University of Batna, always helpful.

I wish to thank Ms. Sihem Kalli, Msila University, for encouragement and for advising me.

Thanks to my classmates and friends of EDA and the Physics Department at the University of Batna, with special thanks to my best friend Sabra Lamri.

Lastly, and most importantly, it is a pleasure to thank my parent, my husband, Kouider Ayache, my sisters, and my brothers who gave me the moral support I required.

Faiza

Introduction

The Earth is constantly showered by radiation from outer space, known as cosmic rays (CRs). This radiation actually consists of charged particles (mostly protons $\sim 85\%$, helium ions $\sim 12\%$, electrons $\sim 2\%$, and a small fraction of heavier elements). Cosmic ray particles are conceived to originate from several possible sources and recent research proposes that the bulk of them originate from the gas and the dust of interstellar medium and are accelerated by strong shock waves driven by supernova explosions. They are influenced by the time dependent magnetic field inside the heliosphere, which corresponds to the 11-year solar activity cycle. Cosmic rays are partly deflected towards the poles when they enter the magnetic field of Earth. A very complicated radiation field develops as particles are generated by successive interactions of primary and secondary nuclei when penetrating deeply into the Earth's atmosphere. The intensity of particles reaches its maximum at about 20 km above sea level and then decreases due to the processes of absorption. Therefore the radiation field is much more intense in the upper atmosphere and is thus of particular concern for airline crews and frequent passengers, who spent many hours in the year at high altitudes.

In 1990, for the first time, the International Commission on Radiological Protection (ICRP) included exposure to cosmic radiation as an occupational exposure. This coincided with a significant increase in air travel and flying at high altitudes for long periods of time. It recommended that the occupational exposure limit for workers should not exceed an effective dose of 20 mSv per year and the exposure limit for the general public should not exceed an effective dose of 1 mSv per year. Several calculation codes have been developed for estimating the doses received by aircrews. This estimation is based on the calculation of the cosmic ray spectra in the atmosphere. For this purpose, several analytical models have been established such as: PARMA, FLUKA, CARI,...

The aim of this work is to estimate the cosmic ray spectra in the atmosphere based on the analytical formula of PARMA model and transpose them to doses using the dose conversion coefficients. For this purpose, we have built a program in C++ language which calculates the cosmic ray spectra of neutrons, protons, helium ions, electrons, positrons, photons, and muons, and estimates the effective dose rate of each of them for any time and location in the atmosphere at altitudes up to 20 km.

This thesis is divided into three main chapters:

The first one is an overview of our current knowledge about cosmic rays and the acceleration mechanisms proposed to explain their origin. The characteristics of air showers produced by the interaction of cosmic rays with the Earth's atmosphere and the detection methods at different energies are also presented.

The second chapter is entirely devoted to dosimetry: the process of determining the energy absorbed in a specified target from a radiation field. We start by the different kinds of ionizing radiation and the biological effects that can be produced in the human body. Then we describe the principal concepts upon which radiation dosimetry is based and the ways in which ionizing radiation can be detected and measured.

Chapter three which is the main part of this work is allocated to the calculation of the cosmic ray spectra and dose rates in any location in the atmosphere at altitudes up to 20 km using the program we built on the basis of the PARMA model. The obtained results are compared with a set of experimental data of EURADOS working group.

Chapter 1

Cosmic rays

Cosmic rays (CRs) are particles pervading the Universe, much more energetic than the ones created in our best accelerators. In this chapter, I briefly review the history of their discovery, the main results of their observation, their origin and acceleration mechanisms, and finally the detection methods at different energies.

1.1 History

The story of cosmic rays began around 1900 with some people interested by measuring the remnant conductivity of air. They found that their electroscopes which measured the amount of ionization discharged even if they were protected from any visible radiation. They assumed that the radioactivity of certain ores present in the Earth's crust was responsible for this effect. This assumption was apparently confirmed in 1910 by Wulf when he made precise measurements on the top of the Eiffel Tower. He observed that discharging rate was decreasing more slowly with altitude. But during 1911-1912 the Austrian physicist Victor Hess made a series of high altitude balloon flights and found that above 1.5 km the ionization rate was stronger. Hess was convinced that the explanation was an extraterrestrial origin of "pen-

etrating radiation”. Hess was awarded the Nobel Prize in 1936 for the discovery of cosmic rays.

Before trying to identify the actual sources of this penetrating radiation, the big issue was to know its nature. In 1925 Millikan thought that these radiations were γ -photons with greater penetrating power than those observed in natural radioactivity. They were coined the term “cosmic-rays”. However, in 1927 Clay demonstrated that cosmic rays intensity depends on the geomagnetic latitude. This was a clear indication of the charged particle nature of cosmic rays, since photons would not have been influenced by the Earth’s magnetic field.

In February 1938, Kollhörster measured coincident signals in Geiger Muller counters set as 75 m apart. He concluded that the counters were hit by secondary particles or showers generated by cosmic rays in the atmosphere. In the late 1930s Pierre Auger undertook investigations of cosmic radiation at the Jungfrauoch (Switzerland) at 3500 m above sea level [1]. Similar to Kollhörster, Auger concluded that the registered particles are secondaries generated from a single primary cosmic ray when it penetrates the Earth’s atmosphere. Subsequent experiments showed that the coincidences continued to be observed even at a distance of 200 m. This led Auger in 1939 to conclude that the energy spectrum of cosmic rays can extend up to 10^{15} eV.

Pierre Auger could not precisely measure the energy of cosmic rays and their arrival directions. These will be done twenty-four years later (1962) by John Linsley through Volcano Ranch array in New Mexico (the set-up comprised 20 stations equipped with scintillation counters arranged on a triangular grid and covering a total area of 12 km^2). With this instrument we recorded for the first time a cosmic ray with an energy of 10^{20} eV.

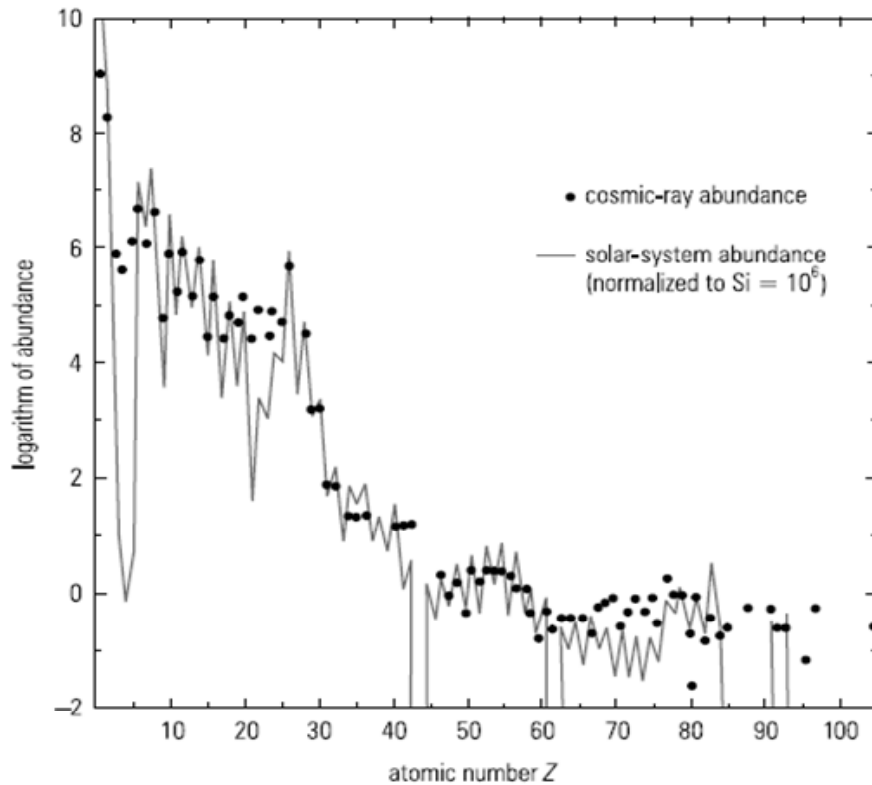


Figure 1.1: Relative abundances of primary cosmic rays for $1 \leq Z \leq 100$ [2].

1.2 Properties of cosmic rays

1.2.1 Composition

The study of the chemical abundances of cosmic rays provides important clues to their origin and to the propagation processes from their birth place to the Earth. The composition of cosmic rays up to energy of 1 TeV is well known. They consist principally of protons (85%), α -particles (12%), nuclei of heavier elements up to uranium (1%), and electrons (2%). The relative abundances of the different cosmic rays elements are shown on figure 1.1.

As one can see the chemical composition of cosmic rays is similar to those of the solar system which are deduced from absorption lines in the solar photosphere. Thus, it appears

that cosmic rays are made up of quite standard interstellar medium. However, significant differences are observed for light elements such as lithium, beryllium and boron ($Z = 3-5$), and for elements with atomic mass numbers just less than those of iron ($Z = 26$). This overabundance of rare species indicates that the cosmic rays have undergone nuclear spallation reactions in which nucleons have been removed from the nucleus before reaching the earth. Such reactions break up the heavier nuclei, such as carbon, oxygen and iron, forming fragments (secondary particles) concentrated just below the parent elements. For example, the fragmentation of the heavier nuclei carbon ($Z = 6$), oxygen ($Z = 8$) in galactic matter forms the lithium, beryllium and boron. In the same way the fragmentation or spallation is also responsible for the abundances of elements below the iron group in cosmic rays. Thus the cosmic rays observed at the earth are a mixture between particles accelerated at the cosmic ray sources (usually called primordial cosmic rays) and nuclei produced by fragmentation reactions in the interstellar space. Unlike the low energy cosmic rays, the determination of the chemical composition of cosmic rays with energies greater than 10^{15} eV is still an open problem. Several recent experiments suggest that there is a transition from a heavier component, iron nuclei, at 10^{17} eV to a lighter component, probably protons, at the highest energies $\sim 10^{20}$ eV [3].

Another component of the primary cosmic rays is the antiparticles, but the latter are extremely rare. The measured primary antiprotons are presumably generated in interactions of primary charged cosmic rays with the interstellar gas [2]. Antiprotons can be readily produced according to:



The flux of primary antiprotons for energies > 10 GeV has been measured to be [2]:

$$\frac{N(\bar{p})}{N(p)} \Big|_{>10 \text{ GeV}} \approx 10^{-4}$$

On the other hand, positrons are most easily formed in pair production by energetic photons via the interaction:

$$\gamma \rightarrow e^+ + e^-$$

As what we have seen above, the fraction of primary electrons in relation to primary protons is only 2%. Primary positrons constitute only 10% of electrons at energies around 10 GeV. Secondary production of anti-nuclei with $Z \geq 2$ by cosmic rays is practically excluded. The non-observation of primary anti-matter with $Z \geq 2$ is a strong hint that our universe is matter dominated [2].

1.2.2 Energy spectrum

The best known characteristic of cosmic radiation is certainly its energy spectrum (figure 1.2). It follows a power law:

$$\frac{dN(E)}{dE} \propto E^{-\gamma} \quad (1.1)$$

over at least 12 orders of magnitudes in energy and 32 orders of magnitudes in intensity (N is the number of particles at an energy E and γ is the spectral index).

The flux of cosmic rays falls off rapidly as the cosmic ray energy increases. At low energies the primary spectrum is deformed because of the sun's magnetic field. The incoming charged particles with energies below about 10 GeV are repelled by the solar wind, the expanding magnetized plasma generated by the sun, which is not constant due to changes in solar activity. Thus the flux of low energy primary cosmic ray particles is correlated to the solar activity which has an alternating eleven year cycle (figure 1.3).

In addition, the lower energy cosmic rays are deflected by the geomagnetic field, which they must penetrate to reach the top of the atmosphere. Thus the intensity of any component of the cosmic radiation in the GeV range depends both on the location and time

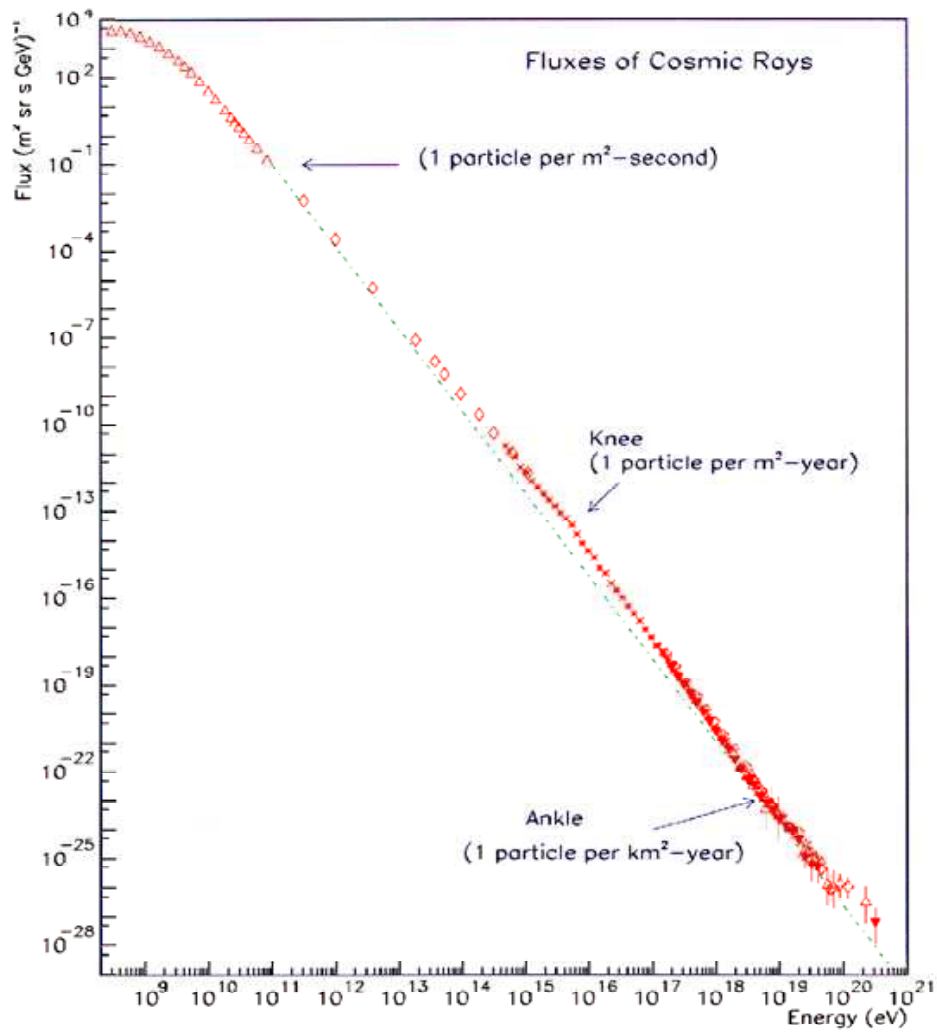


Figure 1.2: Energy spectrum of all particles primary cosmic rays [4].

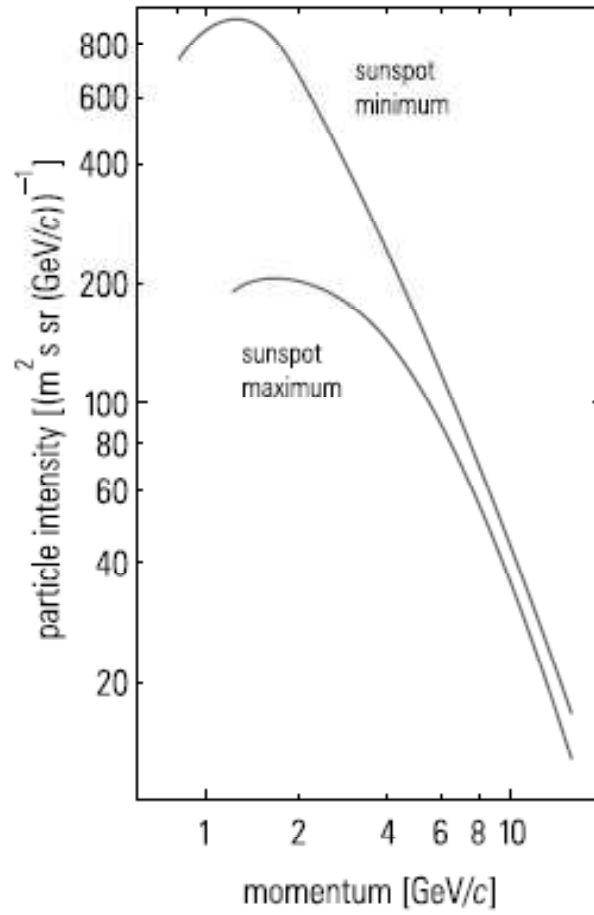


Figure 1.3: Modulation of the primary cosmic ray spectrum by the 11-year cycle of the sun [2].

[5].

From 10 GeV to a few PeV the cosmic rays spectrum is well described by a power law ($\sim E^{-2.7}$). However, around 4 PeV it has a steeping, the knee, characterized by a sudden variation of the spectral index from 2.7 to 3.1. The flux around this energy is of roughly 1 particle per m^2 per year. At about 3 EeV the spectrum softens again in the so called “second knee” to $\gamma = 3.3$. The exact reason of these breaks is not fully understood. Several experiments try to explain their origin from astrophysical scenarios like the change of acceleration mechanisms at the sources, the escape of particles from the magnetic confinement of the galaxy, particle-physics models like the interaction with relic neutrinos during transport or new processes in the atmosphere during air-shower development.

All these models lead to the prediction of a change in the chemical composition over the knee regions. At an energy above 10^{18} eV the spectrum flattens to $\gamma = 2.7$ at what is called the ankle. The flux now is about 1 particle per km^2 per year. This feature is often interpreted as an extragalactic component beginning to dominate over the galactic component.

At energies of order 10^{20} eV and above, the flux of cosmic rays is strongly attenuated. This is in accord with the 1966 prediction of Greisen and of Zatsepin and Kuzmin (GZK) that protons and nuclei will lose a fraction of their energy over distances of a few tens of Mpc on their journey to us, namely they will undergo photopion production process when interacting with the cosmic microwave background radiations. This process limit the distance from which ultra-high energy cosmic rays can arrive to the Earth. Thus cosmic rays with energies above ~ 60 EeV should mostly come from nearby sources (≤ 50 Mpc). Hence the expectation of a sudden break in the spectrum, a so called the GZK cut-off which has been reported by the HiRes and Auger experiments, but not by the AGASA one as

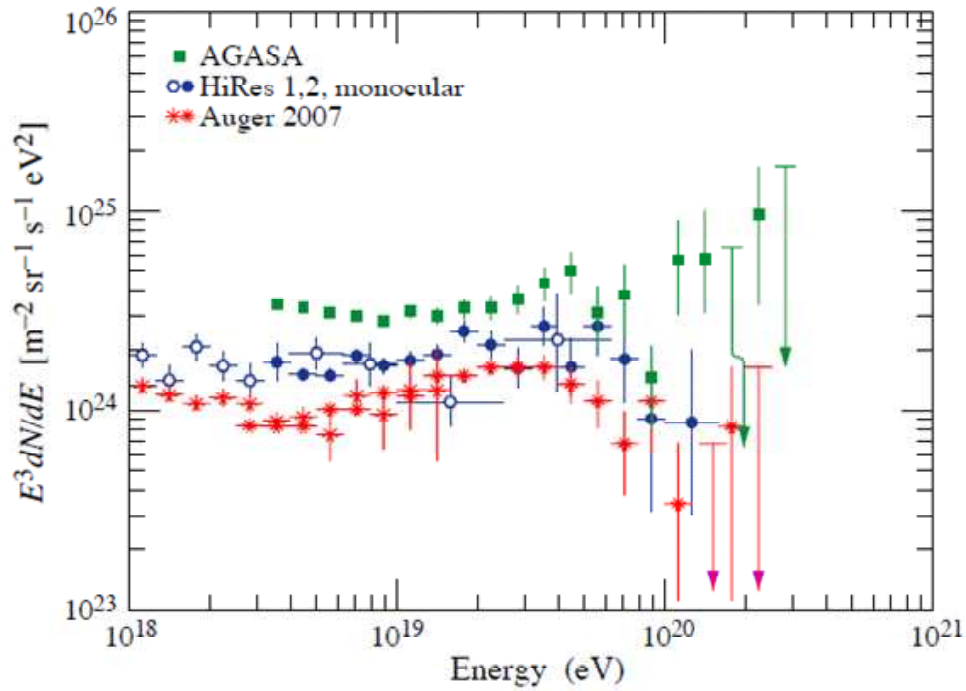


Figure 1.4: Energy spectrum of primary cosmic rays scaled by a factor E^{-3} [5].

shown in figure 1.4

1.2.3 Isotropy

Cosmic rays are mostly charged particles, whose trajectory is deviated by galactic magnetic fields. These latter consist of a large-scale regular and a chaotic, irregular component. The topology of them is poorly known. The few measurements of polarized radio emission from galactic and extragalactic pulsars show that the regular magnetic field is about 2-3 μG . A CR of charge Ze and energy E in a constant field B describes a circle of Larmor radius:

$$R_L(\text{pc}) = \frac{(E/Z) \mu\text{G}}{10^{15} \text{ eV } B} \quad (1.2)$$

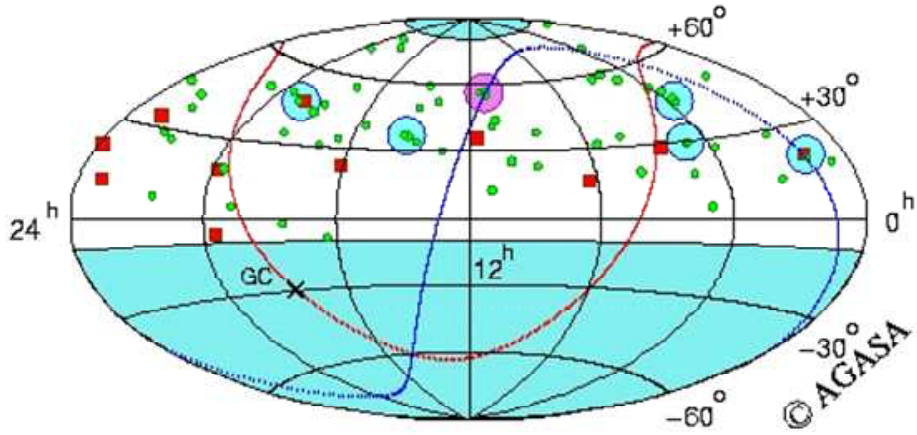


Figure 1.5: Source directions of ultra high energy cosmic rays measured by AGASA [6].

According to the relation (1.2), cosmic rays are confined in the galaxy by the galactic magnetic field until the second knee (~ 3 EeV). They scatter off the turbulent magnetic field irregularities and make a random walk. Thus the cosmic ray flux has to be very close to isotropic and no point sources are expected to be seen. At large energies ($E > 3$ EeV) the deflections in the magnetic field are expected to become smaller than a few degrees and CRs are not confined in the galaxy. The observation of clustering of events (one triplet and five doublets) from individual point sources by the Akeno Giant Air Shower Array (AGASA) collaboration (figure 1.5) can be explained by the assumption that the arrival directions of cosmic rays are anisotropic.

In fact, the recent results of Auger collaboration confirm this expectation through a correlation found between the arrival directions of showers and a catalog of active galactic nucleus (AGNs). Figure 1.6 shows a sky map in galactic coordinates with 27 events of 57 EeV for the full data set with circles of 3.2° around each of them, as well as the positions of the 442 AGNs. The results of AGASA and Auger observatory have demonstrated the feasibility of charged particle astronomy.

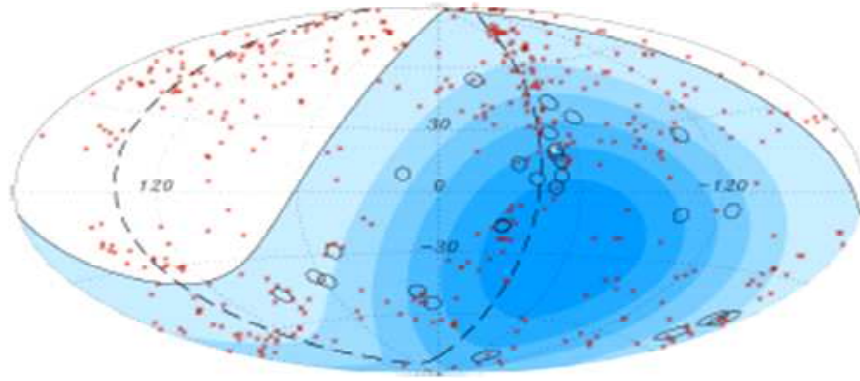


Figure 1.6: Map in galactic coordinates with the positions of the AGNs within 71 Mpc (stars) and the 27 events with $E > 57$ EeV (circles of 3.2° radius). Shading indicates regions of equal exposure [7].

1.3 Origin and acceleration mechanisms

The origin of cosmic rays is one of the main unsolved problems in astroparticle physics. At energies below 1 GeV the flux of CRs observed at Earth exhibits a temporal correlation with the solar activity which is a direct evidence for an origin at the sun. However, at high energy the influence of the solar wind decreases, indicating an origin outside the solar system. The existence of heavy nuclei in cosmic ray components gives us an idea about the sources of CRs which can be identified as the stars which highly evolved like supernova. However, cosmic rays have been observed at much higher energies than supernova remnants can generate, and the big question is where these ultra-high energies cosmic rays come from? Nowadays, several researches assume that in most cases cosmic ray particles are not only produced in the sources but also accelerated to high energies in or near the source. Many celestial objects are suggested to be sites of acceleration such as supernova remnants, pulsars, accreting black holes, the centers of active galactic nuclei, and γ -ray bursts.

1.3.1 Acceleration mechanisms

There are basically two kinds of acceleration mechanisms considered in connection with CR acceleration: (1) direct acceleration of charged particles by electric field, and (2) statistical acceleration (Fermi acceleration) in magnetized plasma [8].

a) Direct acceleration

The acceleration of charged particles by a quasi-static electric field is the simplest conceivable acceleration mechanism. The electric field in question can be due, for example, to a rotating accretion disk threaded by a magnetic field or rotating magnetic neutron stars (pulsars), etc. Nowadays, these acceleration mechanisms are not widely favored as the CR acceleration mechanism; the particle acceleration arises only if the charged particles move in the same direction as the electric field. In addition a disadvantage of this mechanism is that it is difficult to obtain the characteristic power law spectrum of the observed CRs in any natural way.

b) Indirect acceleration

Second order Fermi acceleration In this model Fermi proposed that CRs are accelerated through encounters with moving magnetic clouds. When a particle enters a cloud it changes its energy: it can gain energy in head-on (velocity v of magnetic clouds towards the incoming particle) collisions and loses energy in overtaking (v away from the incoming particle) collisions. The probability of head-on collisions is higher than that overtaking, so the particle gains more energy than loses energy. Let us consider a relativistic particle with energy E_1 in the laboratory frame that is entering a slowly moving magnetic cloud with

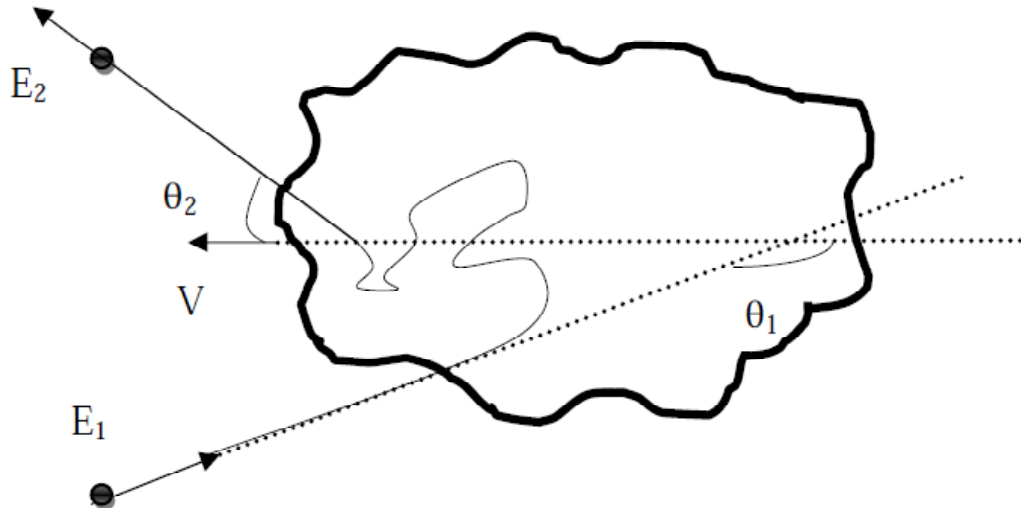


Figure 1.7: Sketch of a collision of a charged particle with moving magnetic cloud.

velocity V (figure 1.7). Lorentz transformations give

$$E'_1 = \gamma E_1 (1 - \beta \cos \theta_1) \quad (1.3)$$

where $\beta = \frac{v}{c}$ and $\gamma = (1 - \beta^2)^{-1/2}$ are the relative speed and Lorentz factor of the cloud, and θ_1 is the angle between the speed vectors of the particle and the cloud. When the particle comes out of the cloud, it has energy E'_2 and angle θ'_2 in the cloud rest frame. Transforming back to the laboratory frame, one can obtain

$$E_2 = \gamma E'_2 (1 + \beta \cos \theta'_2) \quad (1.4)$$

We assume that the scattering is elastic (meaning that the particle energy doesn't vary when moving inside the cloud, so that

$$E'_2 = E'_1 \quad (1.5)$$

Combining equations (1.3), (1.4), and (1.5) one obtains the energy change $\Delta E = E_2 - E_1$, as

$$\frac{\Delta E}{E} = \frac{(1 - \beta \cos \theta_1)(1 + \beta \cos \theta'_2)}{1 - \beta^2} - 1 \quad (1.6)$$

Because of the random walk of particle inside the cloud, all θ'_2 have equal probability, resulting to $\langle \cos \theta'_2 \rangle = 0$.

Since the movement of the cloud is random, the probability of a particle to enter the cloud with $\cos \theta_1$ (for relativistic particle and slow cloud) is proportional to $\frac{c-V \cos^2 \theta_1}{2c}$, from which we derive $\langle \cos \theta_1 \rangle = -\frac{1}{3}\beta$.

Averaging equation (1.6) we obtain:

$$\left\langle \frac{\Delta E}{E} \right\rangle = \frac{1 + \frac{\beta^2}{3}}{1 - \beta^2} - 1 \approx \frac{4}{3}\beta^2 \quad (1.7)$$

Since the mean energy gain per collision is dependent on the cloud velocity squared (equation (1.7)), this model is called the 2^{nd} order Fermi acceleration. As we have seen above the cloud velocity is low compared to the particle velocity ($V \ll v$), this means that the energy gain per collision ($\sim \beta^2$) is very small. Therefore, the 2^{nd} order Fermi acceleration is not a very efficient acceleration process because it requires a very long time. Another important aspect is that cosmic-ray particles will lose some of their gained energy by interactions with the interstellar or intergalactic gas between two collisions [2]. This indicates that this mechanism requires a minimum injection energy above which particles can only be effectively accelerated. These injection energies could be provided by the Fermi mechanism of 1^{st} order [2].

First order Fermi acceleration In this mechanism CR particles are accelerated in shock waves like those associated with supernova explosions. These shocks are formed when a material point propagates in a medium at a speed higher than the reaction speed of this

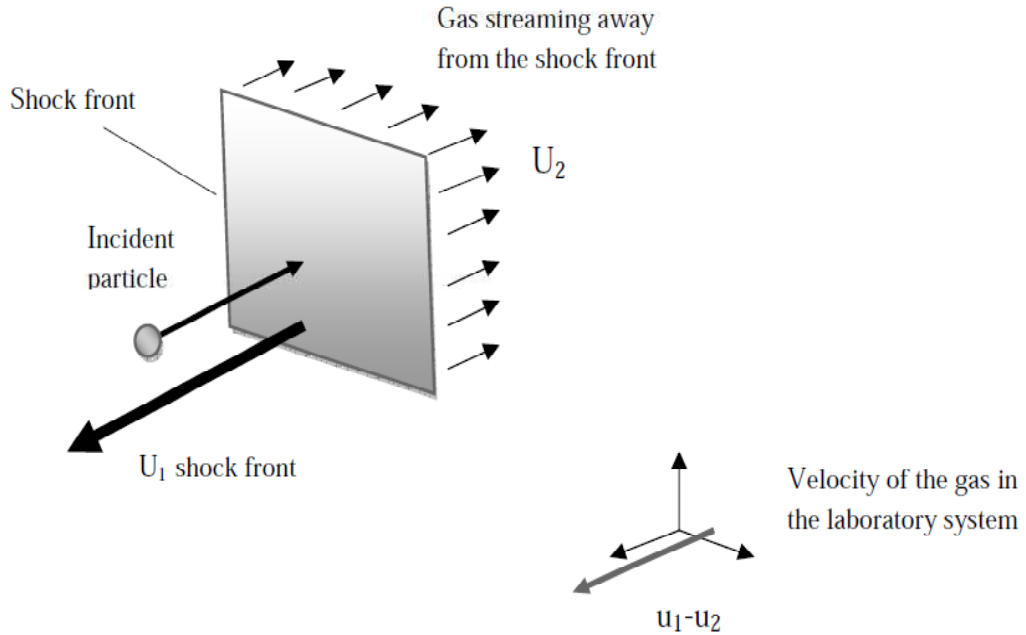


Figure 1.8: Schematics of shock-wave acceleration.

medium. Consider now a large plane shock front moving with a velocity u_1 . Behind the shock front the gas recedes with a velocity u_2 . This means that in the laboratory system the gas has a velocity $V = u_1 - u_2$ (figure 1.8). Only face-on collisions occur, the probability of a particle to hit the shock with $\cos \theta_1$ is proportional to $2\cos^2 \theta_1$ ($-1 \leq \cos \theta_1 \leq 0$) leading to $\langle \cos \theta_1 \rangle = -2/3$. Similarly, $\langle \cos \theta'_2 \rangle = 2/3$, and then

$$\left\langle \frac{\Delta E}{E} \right\rangle = \frac{1 + \frac{4}{3}\beta + \frac{4}{9}\beta^2}{1 - \beta^2} - 1 \approx \frac{4}{3}\beta \quad (1.8)$$

We have again $\langle \Delta E \rangle > 0$, but now we have a first order dependence on the velocity of the cloud (this gives the name to the effect). So that this last kind of Fermi acceleration is more efficient than the second order one simply because β is always less than one.

Suppose that, in each cycle of acceleration at the shock front, the particle gets an energy gain εE_0 . After n cycles its energy becomes

$$E_n = E_0(1 + \varepsilon)^n \quad (1.9)$$

Thus, the number of acceleration cycles which is required to obtain the final energy $E_n = E$ is

$$n = \frac{\ln\left(\frac{E}{E_0}\right)}{\ln(1 + \varepsilon)} \quad (1.10)$$

At each stage of the acceleration the particle has a probability P to escape further the acceleration site. The probability that particles still take part in the acceleration mechanism after n cycles is $(1 - P)^n$ [2]. Thus the number of particles that have energies in excess of E :

$$N(> E) \sim \sum_{m=n}^{\infty} (1 - P)^m \quad (1.11)$$

Because of:

$$\sum_{m=0}^{\infty} x^m = \frac{1}{1 - x} \quad (\text{for } x < 1) \quad (1.12)$$

One gets:

$$N(> E) \sim \frac{(1 - P)^n}{P} \sim \frac{1}{P} \left(\frac{E}{E_0}\right)^{\gamma} \sim E^{-\gamma} \quad (1.13)$$

Where

$$\gamma \approx -\frac{\ln(1 - P)}{\ln(1 + \varepsilon)}$$

In the case of a non-relativistic shock ($\varepsilon \ll 1$ and $P \ll 1$), we have:

$$\gamma \approx -\frac{\ln(1 - P)}{\ln(1 + \varepsilon)} \approx -\frac{P}{\varepsilon}$$

Experimentally one finds that the spectral index up to energies of 10^{15} eV is $\gamma = 1.7$. For higher energies the primary cosmic-ray-particle spectrum steepens with $\gamma = 2$ [2].

1.3.2 Cosmic ray sources

From observations combined with astrophysical theory work, several candidate sites are proposed to be the sources of relativistic particles.

Supernova remnants

All massive stars (stars having masses more than 8 solar masses) are expected to explode at the end of their life time, after they have exhausted their hydrogen. They produce consecutively in their centers heavy nuclei such as He, C, Ne, and others via fusion processes dependent on the central temperature, and finally central cores consisting mainly of iron nuclei are formed. When the fusion process stops at iron, the massive star will collapse under its own gravity which increases both temperature and pressure in the center. Thus, this star explodes violently ejecting several solar matter masses at high speeds. A strong shock wave is formed then in the interstellar medium. Charged particles can be accelerated in this shock according to the first order Fermi mechanism explained above. In addition, the measurements of heavy nuclei in galactic cosmic rays imply that the hypothesis of supernova origin of cosmic rays is the most plausible. In fact, in the course of supernova explosion an enormous number of neutrons are produced. They are first absorbed successively by iron nuclei group and through β -decay processes various nuclei heavier than iron group are synthesized.

Pulsars

Pulsars are rapidly rotating neutron stars, with rotation periods as short as milliseconds for an object with a mass comparable to the mass of the sun yet much more compact with typical radius of ~ 10 Km [9].

In general, the rotational axis of pulsar does not coincide with the direction of the magnetic field. The rotation of this latter around the non-aligned axis can generate an electric field able to accelerate charged particles to ultra-high energies.

Recently, several theories have suggested that iron ions from the crust of newly formed



Figure 1.9: Pulsar of Crab. This image is a composition of images optical (red) and X (blue), observed respectively by the space telescope Hubble and the Chandra observatory [10], [11].

strongly magnetized pulsars may be accelerated through relativistic winds (as in the center of the Crab nebula in figure 1.9). It is claimed that pulsars whose rotational period $T < 10$ ms and magnetic field $B \sim 10^{12-14}$ G, can accelerate iron ions to greater than $\sim 10^{20}$ eV. These ions can pass through the remnant of the supernova explosion that produced the pulsar without suffering significant spallation reactions [8].

Active galactic nuclei

Active galactic nuclei (AGN) are galaxies which have in their centers massive black holes with a particularly intense activity. The accretion disk (disk forms of the accumulation of matter from stars and gas that surround black hole) in fast rotation around the black hole ejects jets of ultra relativistic particles which can reach hundreds of kilo parsec. When the ejected plasma meets the matter clouds it creates hot points which emit a strong radiation in radio waves. Particles can be accelerated up to 10^{21} eV in the relativistic shock waves of jets or on the level of hot points. There are many types of AGN, which are particularly

interesting candidates like sources of UHECRs as radio galaxies FR2¹ and blazard.

1.4 Air showers

After crossing a part of the Universe, primary cosmic rays enter the atmosphere of Earth where they are strongly modified by interactions with atomic nuclei. These interactions depend on the energy and on the nature of the incident primary particle. Indeed:

- A photon or an electron will interact electromagnetically in the atmosphere (pair production, bremsstrahlung) generating a cascade of electromagnetic particles, a so-called electromagnetic shower.

- Hadrons (nucleons, nuclei) will produce by strong interactions with the atmospheric nuclei a cascade of electromagnetic and hadronic nuclei (hadronic shower).

In the following we briefly present the various interactions happening in the atmosphere which lead to the formation of air showers, by specifying the development of the electromagnetic shower, then by explaining the formation of hadron cascades.

1.4.1 Electromagnetic showers

When a high energy electron, positron or photon enters the Earth's atmosphere, it will interact with the electromagnetic field of the air's molecules and causes a cascade of electromagnetic particles. This shower is governed mainly by two processes: pair production and bremsstrahlung.

– *Pair production*

In the presence of an electromagnetic field, a photon of energy higher than $2 m_e c^2 = 1.022$ MeV (rest mass of electron-positron pair) will split into an electron positron pair via

¹ Types of active galaxy that are brightest at the edges.

the interaction:

$$\gamma \rightarrow e^+ e^-$$

– *Bremsstrahlung*

Bremsstrahlung or braking-radiation is an electromagnetic radiation produced when a charged particle changes its velocity. It arises predominantly from collision between electrons and ions. For heavy particles, the bremsstrahlung energy loss is suppressed by the factor $\frac{1}{m^2}$ [5]. The charged particles in the shower are accelerated or decelerated by the Columbian field of air's nuclei which leads to the emission of γ -photons (Bremsstrahlung). We discuss now the longitudinal development of an electromagnetic shower using the simplest toy model (figure 1.10). Consider an electron of initial energy E_0 traversing the atmosphere. In the first interaction length, the electron radiates a photon of energy $E_0/2$ via the bremsstrahlung process. In the next interaction length the photon splits via the pair production into electron positron pair, each with energy $E_0/4$, and that the original electron emits a further photon of energy $E_0/4$ which, in turns, will interact in the next radiation length, and so on. The number of particles along the shower profile coordinate X can be written as $N(X) = 2^{X/\lambda}$, where λ is the average distance between interactions and it is roughly 37 g/cm^2 . The particle number increases with shower depth until the energy of the secondary particles is smaller than the critical energy E_c , below which the absorptive processes like ionization for charged particles, Compton scattering and photoelectric effect for photons start to dominate and cause the shower to die out.

1.4.2 Hadronic shower

A hadronic shower is produced when a high energy hadron interacts with the atmospheric nuclei via the strong force. It is initiated only if the primary cosmic ray is a hadron. Primary protons and nuclei have mainly two ways to develop as shown in figure 1.11. The

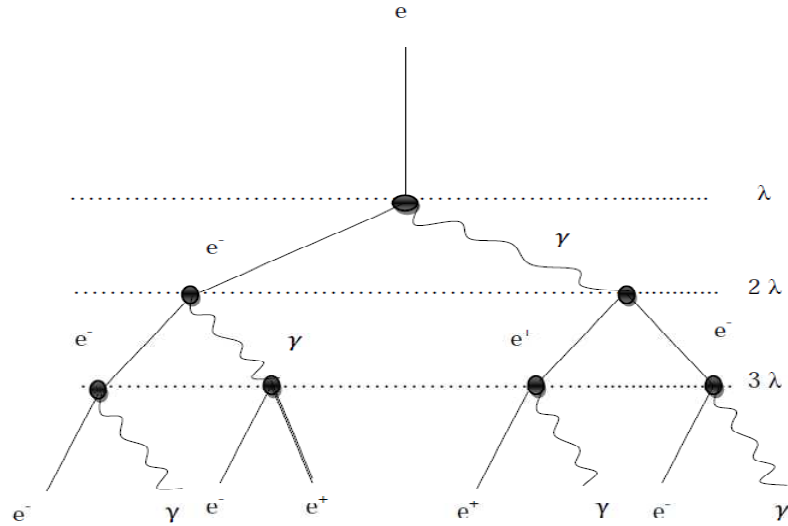


Figure 1.10: Schematic view of the creation of electromagnetic shower in the atmosphere.

first possibility is the so-called nuclear coalescence. A primary proton or nucleus collides with the air's nuclei producing mesons (K^0 , K^\pm , Π^0 , Π^\pm), nuclear debris such as protons, neutrons, antiprotons, and light nuclei.

- Neutral pions (π_0) can disintegrate producing photons which initiate so the electromagnetic shower as describing in the precedent paragraph.

$$\pi_0 \rightarrow \gamma \gamma$$

- The charged pions π^\pm decay into muons and neutrinos which propagate in a straight line until the ground level without interaction:

$$\left\{ \begin{array}{l} \pi^+ \rightarrow \mu^+ + \nu_\mu \\ \pi^- \rightarrow \mu^- + \bar{\nu}_\mu \end{array} \right.$$

- The kaons, with their variety of disintegration channels, contribute to the muonic component, and to the electromagnetic component. The relativistic muons travel to ground level (relativistic dilatation of their life time) and they are called the hard component of CRs. The so called "soft component" is made up of electrons and positrons from muons

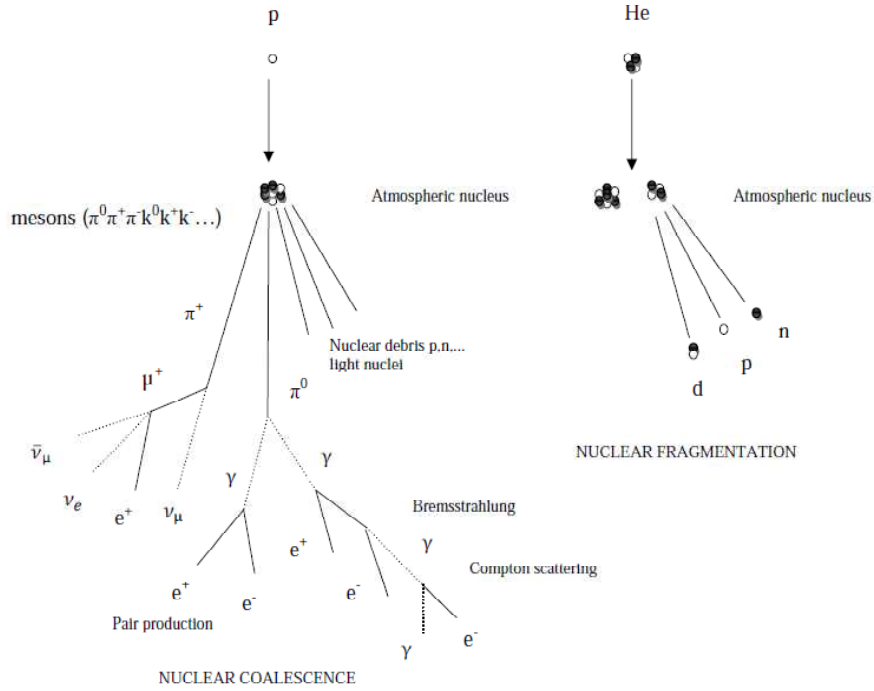


Figure 1.11: Schematic view of the creation of hadronic shower in the atmosphere.

decay and from the electromagnetic showers [12].

$$\begin{cases} \mu^+ \rightarrow e^+ + \bar{\nu}_\mu + \nu_e \\ \mu^- \rightarrow e^- + \nu_\mu + \bar{\nu}_e \end{cases}$$

The other products of nuclear coalescence interact with air's nuclei initiating further secondaries or lose energy through ionization, depending on their energy.

The second possible interaction of primary nuclei is “nuclear fragmentation” or spallation. The primary nucleus interacts with the atmospheric nucleus leading to the breakage of it into other nuclei. These latter themselves produce a cascade of particle through nuclear coalescence process or nuclear fragmentation if the primary nucleus is heavy. Figure 1.12 shows the vertical fluxes of the major cosmic ray components in the atmosphere with kinetic energy $E > 1$ GeV as a function of the atmospheric depth. An air shower can be described by three components, electromagnetic, muonic and hadronic [12]. The predominant component at sea level is the muonic component (80%) with a mean energy of ~ 4 GeV. Their

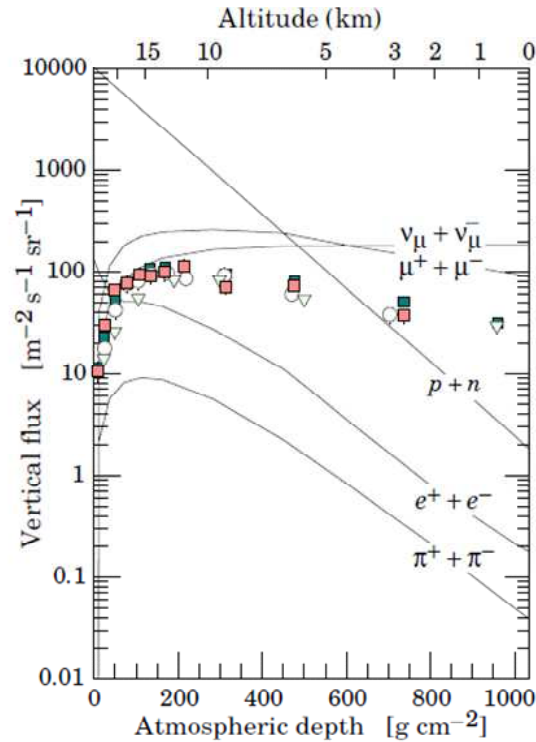


Figure 1.12: Vertical fluxes of cosmic rays in the atmosphere with $E > 1$ GeV [5].

flux through a horizontal is roughly one particle per cm^2 and minute [5].

In conclusion, the particle number grows with increasing altitude until it reaches a maximum at about 100 -120 g/cm^2 of residual atmospheric depth.

1.5 Detection of cosmic rays

1.5.1 Direct detection

Direct measurements of the chemical composition and the fluxes of CRs up to the highest energies are the goals of several experiments. The aim is to understand the acceleration mechanisms of primary cosmic rays in order to identify their sources and to clarify their interactions with the interstellar medium. We have seen in subsection 1.2.2 that the cosmic ray particle flux decreases with energy in form of a power law, this means that the direct

detection of cosmic rays is possible only at low energies ($< 10^{14}$ eV). The experiments that study cosmic rays directly are done on board of balloons in the upper atmosphere (JACEE, Runjob, Bess...) or in space such as AMS experiment. The direct detection of CRs enables us to study all their characteristics: mass, energy, and charge, which therefore allows identifying their nature. Current measurements inform us that at low energy, cosmic rays consist of approximately 2% of electrons and 98% of hadrons including 85% of protons and 12% of alpha particles and 1% of heavier nuclei (C, O, N...). At high energies ($E > 10^{14}$ eV), the flux of CRs is so low and their measurement requires large detectors. In this case, it is not possible to install heavy detectors on balloon or satellite. They are placed on the ground level and measure the cascade of particles that primary cosmic rays produce when they interact with the Earth's atmosphere.

1.5.2 Indirect detection

The indirect detection of cosmic rays is based on the observation of extensive air showers with ground-based experiments [13]. An air shower is a cascade of particles generated through the interaction of primary cosmic ray with the atmospheric nuclei. It consists mainly of three components: the electromagnetic, muonic, and hadronic component. The detection of air showers has been performed by a variety of techniques: Cerenkov, fluorescence, and detector-array techniques.

a) Cerenkov technique

Cerenkov radiation is an electromagnetic radiation emitted when the velocity v of a charged particle is greater than the speed of light in a medium with a given refractive index n :

$$v > \frac{c}{n}$$

The Cerenkov radiation forms a cone around the axis of the air shower (figure 1.13).

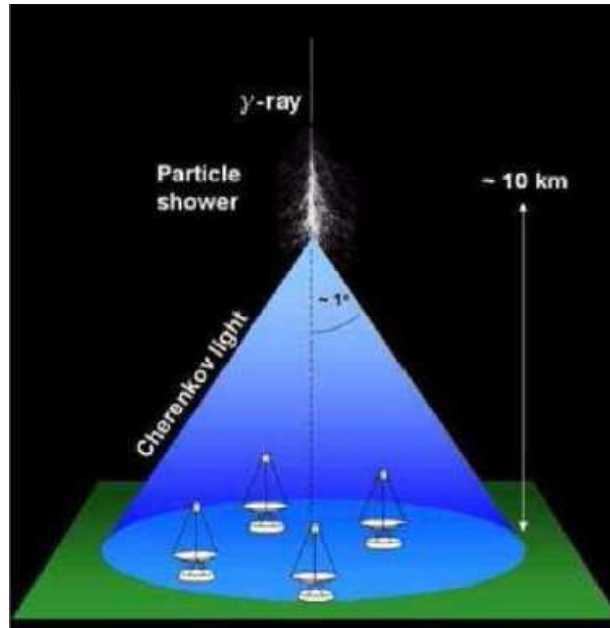


Figure 1.13: Detection of γ -ray through cerenkov radiation.

The angle θ of this cone is given by:

$$\theta = \cos^{-1} \left(\frac{1}{n\beta} \right), \quad \beta = \frac{v}{c} \quad (1.14)$$

n increases slightly as the shower develops in the atmosphere, consequently, θ also increases: the Cerenkov cone created by a particle with $\beta = 1$ widens from 1.06° at 5 km of altitude to 1.36° at sea level [14]. An air shower produces a great quantity of Cerenkov radiation. The number of this radiation for a primary particle with an energy of 1 TeV amounts to about 10^6 photons which arrive to the ground level at the same time as the particle shower. We use Cerenkov radiation to detect CRs at low energy where the flux is important and where few particles arrive until the ground level.

The detection of these radiations is made by means of large spherical mirror arrays which direct it to photomultiplier placed at the focus (figure 1.14). But, the principal use of Cerenkov technique is in high energy gamma astronomy (of the order of TeV). One of the most important experiments which use this technique is HESS (figure 1.14 represents



Figure 1.14: One telescope of HESS experiment [15].

one Cerenkov telescope of HESS experiment). A disadvantage of this technique is that the observation can be done only in nights without moon and clouds.

b) The fluorescence technique

When the charged particles in an air shower traverse the atmosphere, they excite the air nitrogen causing it to emit an isotropic radiation in the ultraviolet range (300-400 nm) via a process called fluorescence. The quantity of fluorescence photons produced by showers is proportional to the charged particle number. Whenever this last is large, whenever the fluorescence radiation is intense. Thus, this technique is more effective in ultra-high energy cosmic rays. The basic function of the fluorescence detections is to measure the longitudinal profile of the extensive air showers [13]. The observation of this radiation can be done either since the ground level by looking at the sky (HiRes, AUGER ...), or observing the atmosphere from space (EUSO ...). A disadvantage of this technique is that the observation is done in moonless nights to avoid a contribution of any other photon sources.

c) **Detector-arrays technique**

This technique consists of the study of particle fluxes resulting from the interaction of primary cosmic ray with the upper atmosphere. Indeed, when a primary cosmic ray penetrates the Earth's atmosphere, it interacts with the air nuclei producing a cascade of secondary particles. They mainly consist of muons, electrons, positrons, neutrinos, and photons. The observation of extensive air shower is performed by using a great number of detectors, distributed over a large area. These detectors sample the charged particles in the shower, usually by means of tanks containing liquid scintillator or water Cerenkov counters.

The detected particles at ground level are mainly muons; they are produced from disintegration of charged pions. The measurement of their arrival direction time permits to determine the energy and the arrival direction of the primary cosmic ray. Many experiments are based on this technique among them: KASCADE experiment (figure 1.15) which is composed of about 252 detectors installed in Karlsruhe on a restricted site of 0.05 km^2 and AUGER experiment (figure 1.16), which is composed of 1600 detectors with 4 fluorescence stations distributed on a large area in Argentina (3000 km^2).



Figure 1.15: KASCADE experiment [16].



Figure 1.16: Pierre Auger Observatory array in the Argentinean Pampa [17].

Chapter 2

Dosimetry

After the discovery of X rays in 1895 by Roentgen and radioactivity in 1896 by Becquerel, it has been known that exposure to ionizing radiation can be harmful to humans. In any use of ionizing radiation, one must prevent or minimize the risks of the use of radiation while allowing its beneficial applications [18]. For this purpose, two international commissions, the International Commission on Radiation Units and measurements (ICRU) and the International Commission on Radiological Protection (ICRP) were established. ICRU is charged to define units concerning radioactivity and their effects and ICRP is charged to define protection criteria against ionizing radiation. The field of work of these two commissions has widened from protection in medical radiology to all aspects of protection against ionizing radiation. In this chapter we describe the principal concepts upon which radiation dosimetry is based, biological effects that can ionizing radiation produce in the human body, and the ways in which ionizing radiation can be detected and measured.

2.1 Ionizing radiation

According to the ability to ionize matter, radiation can be classified into two main categories, non-ionizing radiation which has enough energy to move or vibrate atoms in a molecule, but not enough to change them chemically, and ionizing radiation which has enough energy to

actually break the chemical bonds. The ionizing radiation falls into two categories: direct ionizing radiation (charged particles such as protons, electrons, α -particles, and heavy ions) and indirect ionizing radiation (uncharged particles such as high energy photons and neutrons). When a charged particle passes in a medium it loses a fraction of its energy through direct coulomb interactions between the charged particle and the orbital electrons of atoms or molecules. The transferred energy causes the affected electrons to move into higher orbital energy levels (excitation) or to escape the orbital atomic structure completely (ionization). The loss of energy continues until the remaining energy of charged particles is not sufficient to produce additional excitation or ionization. In addition, a charged particle may lose energy by emission of electromagnetic radiation during deceleration (bremsstrahlung radiation).

Unlike the directly ionizing radiation, indirectly ionizing radiation deposit energy in the medium through two step processes. In the first step, charged particles are released in the medium (photons release electrons or positrons, neutrons release protons or heavy ions), whereas, in the second step these released charged particles deposit energy in the medium through direct coulomb interactions as what we have seen in the case of directly ionizing radiation.

A most important property of ionizing radiation is its ability to penetrate matter. The depth of penetration depends on both energy and type of ionizing radiation. For a particular type of radiation it increases with the energy of radiation, however for the same amount of energy the depth varies from one type of radiation to another. For equal energies the depth of penetration of β -particle is greater than of α -particle. An α -particle has a short range (several centimeters) in air and cannot penetrate the outer layer of skin whereas a β -particle can penetrate further into materials or tissue and can be absorbed completely

by sheets of plastic, glass, or metal. For indirectly ionizing radiation such as high energy photons and neutrons, the degree of penetration depends on the nature of their interactions with matter. Gamma radiation can be absorbed as it penetrates a substantial thickness of dense materials such as steel or lead. Neutrons can also be very penetrating and blocked only when using material consisting of light elements, like hydrogen which slows or captures them.

Ionizing radiation comes from a variety of natural and artificial sources. The natural sources include cosmic rays in which we are interested in this thesis, and natural radioactive elements. Some of the latter are primordial radioactive elements that were created when the Earth was born, and others are cosmogenic radionuclides that resulted from the interaction of cosmic radiation with the upper atmosphere. The artificial sources include fallout from the testing of nuclear weapons in atmosphere, discharges of radioactive waste from the nuclear industry, industrial gamma rays...

2.2 Biological effects of ionizing radiation

The basic structure of living matter is the cell. An interaction of ionizing radiation with living matter can potentially affect the normal operation of cell. There are two categories of health effect that can ionizing radiation produce when it interacts with the human body: stochastic effects and deterministic effects.

2.2.1 Stochastic effects

Stochastic effects are those that are, as the name implies, probabilistic. They are not certain to occur in any given exposed individual. These effects are associated with low level exposure to radiation, and often show up years, even decades, after exposure (and were once called late effects). Exposure to ionizing radiation, even at low doses may cause

a biochemical changes in cell leading to cell modification or cell killing. If one cell or a small number of cells are killed by ionizing radiation there will be no consequences for the irradiated organism. However, if the cell is modified in a way leading to a cancer induction or genetic changes the result may have serious consequences for the irradiated organism and for future generations. The likelihood that cancer or genetic effect will happen increases as the dose increases, but the severity of the effects will remain constant (the irradiated individual will either get cancer or not). Because ionizing radiation is not the only known cause of most of stochastic effects, it is normally impossible to determine clinically whether an occurrence of cancer or genetic effect was due to a specific radiation exposure or not.

2.2.2 Deterministic effects

Deterministic or non-stochastic effects are those that are generally observed soon after exposure to ionizing radiation. They appear in case of exposure to high levels of radiation in which the number of cells destroyed increases, and occur only if the dose or dose rate is greater than some threshold value, below which the effects will not be observed. Unlike stochastic effects, the severity of the damage of non stochastic effects will increase when the absorbed dose is increased. Therefore, the occurrence of these effects is clearly associated with the radiation exposure. Deterministic effects will often be evident within hours or days. Examples of these effects include erythema (reddening of the skin), skin and tissue burns, cataract formation and death.

2.3 Dosimetric quantities and units

The quantities used in dosimetry of ionizing radiation are divided into physical quantities which are employed for the description of the radiation field and its interactions with matter, and quantities in radiation protection dosimetry which includes the protection quantities

and the operational quantities.

2.3.1 Physical quantities

a) Stopping power

Stopping power is widely used in radiation physics and dosimetry. It is often defined as the average linear rate of energy loss per unit path length that a charged particle suffers as the result of variety of electromagnetic interactions with the medium in which it propagates. Common unit of stopping power is MeV/cm. According to the interaction occurring in the medium, stopping power can be classified into two categories: collisional (ionization) and radiative (bremsstrahlung).

Collisional stopping power is defined as the mean energy loss per unit path length that charged particles suffer as the result of interactions with atomic orbital electrons of the absorbing medium. The interaction of heavy charged particles with atomic orbital electrons causes them to lose energy through ionization and atomic excitation. In a single electronic collision they can transfer only a small fraction of their energy, and they scatter through small angles by nuclei. The collisional energy losses vary logarithmically with energy, and for relativistic heavy charged particle it can be described by the Bethe-Bloch equation [19]:

$$-\frac{dE}{dx} = \frac{4\pi k_0^2 z^2 e^4 n}{m_e c^2 \beta^2} \left[\ln \frac{2m_e c^2 \beta^2}{I(1 - \beta^2)} - \beta^2 \right] \quad (2.1)$$

where

- ◆ $k_0 = 8.99 \times 10^9 \text{Nm}^2\text{C}^{-2}$.
- ◆ z : atomic number of the heavy particle.
- ◆ e : magnitude of the electron charge.
- ◆ $n = \frac{N_A \cdot Z \cdot \rho}{A}$ is the electron density of the absorber.
- ◆ N_A : Avogadro's number.

- ◆ Z : atomic number of the absorber.
- ◆ ρ : mass density of the absorber.
- ◆ A : the atomic weight of absorber.
- ◆ m_e : mass of the electron.
- ◆ I : mean excitation energy of the absorber[eV].

The following approximate empirical formulas can be used to estimate the I value in eV

for an element with an atomic number Z [19]:

$$\left\{ \begin{array}{ll} I(\text{eV}) \approx 19.0 & \text{for } Z=1 \text{ (hydrogen)} \\ I(\text{eV}) \approx 11.2+11.7 \times Z & \text{for } 2 \leq Z \leq 13 \\ I(\text{eV}) \approx 52.8+8.71 \times Z & \text{for } Z>13 \end{array} \right.$$

Like heavy charged particles, electrons and positrons can excite and ionize atoms as they traverse matter. However, they can deposit a large fraction of their energy in a single collision with atomic electrons of the same mass, and they suffer relatively large deflections. Therefore, their path is very erratic. The mean energy loss per electron or positron can be written as [19]:

$$\left[-\frac{dE}{dx} \right]_{\text{col}} = \frac{4\pi k_0^2 e^4 n}{m_e c^2 \beta^2} \left[\ln \frac{m_e c^2 \tau \sqrt{\tau+2}}{\sqrt{2I}} + F^\pm(\beta) \right] \quad (2.2)$$

where $F^-(\beta)$ is used for electrons, and is given by [19]:

$$F^-(\beta) = \frac{1-\beta^2}{2} \left[1 + \frac{\tau^2}{8} - (2\tau+1) \ln 2 \right] \quad (2.3)$$

and $F^+(\beta)$ is used for positrons [19]:

$$F^+(\beta) = \ln 2 - \frac{\beta^2}{24} \left[23 + \frac{14}{\tau+2} + \frac{10}{(\tau+2)^2} + \frac{4}{(\tau+2)^3} \right] \quad (2.4)$$

here $\tau = \frac{T}{m_e c^2}$ is the kinetic energy T of the electron or positron expressed in multiples of the electron rest energy $m_e c^2$.

Radiative stopping power is defined as the average energy loss per unit path length that a charged particle suffers as a result of the interaction with atomic nuclei when penetrating a material. The interaction of a charged particle with atomic nuclei causes it to lose energy through bremsstrahlung process. The radiative cross section of charged particle of mass M and velocity v , emitting photons of energy $h\nu$ is expressed as [20]:

$$\frac{d\sigma}{d(h\nu)} = 5 \cdot \frac{e^2 Z^2}{\hbar c} \left[\frac{m_e c^2}{Mv} \right]^2 \cdot \frac{r_e^2}{h\nu} \ln \left[\frac{Mv^2 \gamma^2}{h\nu} \right] \quad (2.5)$$

The cross section is inversely proportional to the mass square projectile; thereby, the radiative energy loss rate is important only in the case of electrons and muons of high energies. In addition, bremsstrahlung losses increase with atomic number Z of the absorbing medium: the energy loss rate in high- Z materials is greater than in low- Z materials. Unlike collisional energy losses, the radiative energy loss rate increases with kinetic energy. For electrons with energy greater than MeV, it is given by the Bethe-Heitler equation [20]:

$$\left[\frac{dE}{dx} \right]_{\text{rad}} = 4\alpha \frac{Z^2}{A} r_e^2 n \cdot E \cdot \ln \left[\frac{183}{Z^{1/3}} \right] \quad (2.6)$$

where $\alpha = \frac{e^2}{4\pi \epsilon_0 \hbar c} = \frac{1}{137}$ is the fine structure constant.

The total stopping power for electrons or positrons is equal to the sum of both collisional and radiative stopping powers.

$$\left(-\frac{dE}{dx} \right)_{\text{tot}}^{\pm} = \left(-\frac{dE}{dx} \right)_{\text{col}}^{\pm} + \left(-\frac{dE}{dx} \right)_{\text{rad}}^{\pm} \quad (2.7)$$

The energy at which the energy loss by ionization and bremsstrahlung are equal is called critical energy, E_c . At low energies collisional effects dominate over radiative ones and above the critical energy, radiative energy loss begins to be important. The critical energy E_c of electrons propagating in material Z is given by

$$E_c = \frac{1600}{Z} (m_e c^2) = \frac{817}{Z} \text{ MeV} \quad (2.8)$$

Very often the concept of mass stopping power is used in calculations. It is defined as the stopping power, $-\frac{dE}{dx}$, divided by mass density, ρ , of the absorbing medium. Division by mass density eliminates the dependence of mass stopping power on mass density of the medium. Typical unit of mass stopping power is $\text{MeV} \cdot \text{cm}^2/\text{g}$.

b) Linear Energy Transfer (LET)

The linear energy transfer (LET) is defined as the rate of energy transferred per unit distance along a charged particle track. It has the same dimensions of stopping power, but it is not the same quantity. Stopping power is concerned with the energy transferred from the charged particle in a target, whereas LET is the energy actually absorbed there (secondary δ -electrons can transport a fraction of the energy out of the target, especially if the target is small compared with the ranges of secondary electrons). The LET is often defined as restricted linear stopping power, the linear rate of energy loss due only to collisions in which the energy transfer does not exceed a certain value Δ , $(-\frac{dE}{dx})_\Delta$, and it is written

$$L_\Delta = \frac{dE_\Delta}{dx} \quad (2.9)$$

where dE_Δ represents the total energy lost by the charged particle due to electronic collisions minus the kinetic energies of all secondary electrons with energies in excess of Δ . When Δ increases the linear energy transfer tends to the usual (unrestricted) collisional stopping power.

c) Activity

Activity, A , is the expectation value of the number of atoms that decay in a given quantity of material per unit time. The unit of activity is the becquerel (Bq), defined as one disinte-

gration per second ($1 \text{ Bq} = 1 \text{ s}^{-1}$). The traditional unit of activity is the curie (Ci), $1\text{Ci} = 3.7 \times 10^{10} \text{ Bq}$.

d) Fluence

The particle fluence is defined as the number of particles dN incident upon a small sphere of sectional area da

$$\Phi = \frac{dN}{da} \quad (2.10)$$

e) Exposure

Exposure radiation is defined as the amount of ionization produced by an electromagnetic radiation in a unit mass of air, at normal atmospheric conditions (temperature and pressure). The measurement of exposure is difficult at energy less than several KeV and more than several MeV. Accordingly, the use of exposure is limited to X and γ -rays whose energies do not exceed 3 MeV. The unit of exposure is the Roentgen; it was originally defined as the amount of γ or X radiations that produce in 0.001293 g of air 1 electrostatic unit ($1 \text{ esu} = 3.336 \times 10^{-10} \text{ C}$) of charge either sign. This last includes both the ions produced directly by the incident photons as well as ions produced by all secondary electrons. Since 1962, exposure has been defined by the ICRU as the quotient $\Delta Q/\Delta m$, where ΔQ is the sum of all charges in a mass Δm of air. Therefore, the new unit used to measure exposure radiation is the X unit, defined as the production of 1 C of charge in 1 Kg of air. The modern definition of unit Roentgen in this case is the amount of X -radiation or γ -radiation that produces $2.58 \times 10^{-4} \text{ C}$ of charge in 1 Kg of air, that is

$$\begin{aligned} 1 \text{ R} &= \frac{1 \text{ esu} \times 3.336 \times 10^{-10} \text{ C/esu}}{0.001293 \text{ g}} \times 10^3 \text{ g/kg} \\ &= 2.58 \times 10^{-4} \text{ C/kg of air} \end{aligned}$$

The amount of energy required to produce 1 single ion pair in air is 34 eV on average, since the charge of an electron is equal to 1.6×10^{-19} C, an association can be established between X unit and the energy measured in Joules, deposited in 1 Kg of air. Hence the X unit corresponds to deposition of 34 J/Kg.

f) Kerma

Kerma is the acronym for kinetic energy released per unit mass. It is applicable only for uncharged particles such as neutrons and photons and often defined as the sum of the initial kinetic energies of all charged particles dE_{tr} liberated by indirectly ionizing radiation per unit mass dm of a specified material:

$$K = \frac{dE_{tr}}{dm} \quad (2.11)$$

The SI unit of kerma is the Gray (Gy), where 1 Gy= 1 J/Kg. In the traditional system of units, kerma is measured in rad (radiation absorbed dose) which is equal to the absorption of 100 erg (1 erg= 10^{-7} J) of energy in 1 g of absorbing medium.

g) Absorbed dose

The fundamental physical quantity used in radiation dosimetry is the absorbed dose. In contrast to the exposure and Kerma, absorbed dose applies to all kinds of ionizing radiation (directly and indirectly). It is generally defined as the ratio of mean energy, $d\bar{\epsilon}$, imparted by ionizing radiation to matter of mass, dm , in a volume element. It is given by

$$D = \frac{d\bar{\epsilon}}{dm} \quad (2.12)$$

where the imparted energy $d\bar{\epsilon}$ is the sum of all particle energies entering the volume of interest minus all particle energies leaving that volume, taking into account any mass-energy transformation within the volume. The absorbed dose has the same unit of kerma,

Gray, but it is not the same quantity. Kerma is a measure of the energy transferred to the medium, whereas absorbed dose is a measure of the energy that actually remains in the medium.

2.3.2 Protection quantities

Protection quantities are dose quantities developed by the ICRP for the specification of limits on exposure of human body to ionizing radiation from both whole and partial body external and internal irradiation.

Table 2.1: Radiation weighting factors w_R [21].

Radiation type	w_R
Photons, electrons and muons	1
protons and charged pions	2
Alpha particles, fission Fragments, heavy ions	20
Neutrons, $E_n < 1$ MeV	$2.5 + 18.2 \times \exp \left[-(\ln E_n)^2 / 6 \right]$
$1 \text{ MeV} \leq E_n \leq 50 \text{ MeV}$	$5.0 + 17.0 \times \exp \left[-(\ln (2E_n))^2 / 6 \right]$
$E_n > 50 \text{ MeV}$	$2.5 + 3.25 \times \exp \left[-(\ln (0.04E_n))^2 / 6 \right]$

a) Equivalent dose

The degree of biological damage differs from radiation particle to another, even for the same amount of absorbed dose. Thus, to reflect the harm that different types of ionizing radiation can do in biological systems, the concept equivalent dose is used. The equivalent dose, H_T , of an organ or tissue is defined as the sum of absorbed doses $D_{T,R}$ caused by different radiation types R weighted with radiation weighting factor w_R :

$$H_T = \sum_R w_R \cdot D_{T,R} \quad (2.13)$$

The SI unit of equivalent dose is Sievert (Sv). The values for w_R recommended by the ICRP in its publication 103 are given in table 2.1.

b) Effective dose

Various tissues or organs exhibit different sensitivities to a kind of radiation. The lung, for example, reacts more dramatically than thyroid. To take into account the specific organs and areas of the human body that are exposed to ionizing radiation, equivalent dose must be weighted by dimensionless factors, w_T :

$$E = \sum_T w_T H_T \quad (2.14)$$

The values for w_T recommended by ICRP in its publication 103 are shown in table 2.2. Effective dose E is used as a measure of likelihood of stochastic health effects in human body that exposed to ionizing radiation. The SI unit of effective dose is Sievert. To keep the risk of occurrence of stochastic health effects to acceptable levels and for avoiding tissue reactions in workers and members of the public, the ICRP in its publication 103 recommended that workers should not be exposed more than 20 mSv per year, and members of the public to not more than 1 mSv per year of effective dose. It also recommended that the dose limit of an unborn child of pregnant aircrew members is 1 mSv during period of the pregnancy.

Table 2.2: Recommended tissue weighting factors [21].

Tissue	w_T	$\sum w_T$
Bone-marrow, colon, lung, stomach, breast, remainder tissues*.	0.12	0.72
Gonads	0.08	0.08
Bladder, oesophagus, liver, thyroid.	0.04	0.16
Bonesurface, brain, salivaryglands, skin	0.01	0.04

*Remainder Tissues: Adrenals, Extrathoracic (ET) region, gall bladder, heart,...[21].

2.3.3 Operational quantities

The doses in tissues or organs within the human body, equivalent dose and effective dose, are difficult to assess and impossible to measure directly. Therefore, practical quantities, measurable outside the body, are needed. For external exposures, measurable quantities, called operational quantities, have been recommended by the ICRU. These quantities aim to provide an estimate or upper limit for the value of the protection quantities related to an exposure, or potential exposure of persons under most irradiation conditions [21]. The operational quantities were specified before the introduction of the radiation weighting factor, hence their definition is based on the concept dose equivalent which is defined from ICRP in its publication 26 (1977) as the product of the absorbed dose D and a dimensionless quality factor Q . This last is defined as a function of linear energy transfer, L . The dependence of Q on L is given by the following equation:

$$\left\{ \begin{array}{ll} Q(L) = 1 & \text{for } L < 10 \text{ KeV}/\mu\text{m} \\ Q(L) = 0.32 L - 2.2 & \text{for } 10 \leq L \leq 100 \text{ KeV}/\mu\text{m} \\ Q(L) = 300/\sqrt{L} & \text{for } L > 100 \text{ KeV}/\mu\text{m} \end{array} \right.$$

The radiation incident on a human body can be characterized as either “low penetrating” or “penetrating”, depending on the ratio of the skin dose to effective dose. Radiation is considered to be low penetrating when the dose equivalent received by the skin (dose received at depth of 0.07 mm) in the case of normal incidence of a broad radiation beam is higher than ten times the effective dose otherwise it is considered to be penetrating [22]. The determination of operational quantities was made separately for area monitoring and for individual monitoring.

a) Operational quantities for area monitoring

For all types of radiation the operational quantities for area monitoring are defined on the basis of a phantom approximating the human body, called the ICRU sphere. It is a sphere with a diameter of 30 cm constituted from tissue equivalent material with density 1 g cm^{-3} consisting of oxygen of 72.2%, carbon of 11.1%, hydrogen of 10.1%, and nitrogen of 2.6%. An expanded radiation field is a radiation field in which fluence and its directional and energy distributions have the same value throughout the volume of interest as in the actual field at the point of reference. In the expanded and aligned field, the fluence and its energy distribution are the same as in the expanded field, but the sphere ICRU is homogeneously irradiated from one direction.

Two concepts binding the external radiation field to the effective dose and to the equivalent dose in the skin are introduced for area monitoring. The first of these concepts, the ambient dose equivalent, $H^*(d)$, appropriated to penetrating radiation, and the second, the directional equivalent dose, $H'(d, \Omega)$, refers to the low penetrating radiation.

Ambient dose equivalent The ambient dose equivalent, $H^*(d)$, at a point in a radiation field, is the dose equivalent that would be produced by the corresponding expanded and aligned field, in the ICRU sphere at depth d , on the radius opposing the direction of the aligned field [23]. The SI unit of ambient dose is Sievert. For penetrating radiation, a depth of 10 mm is employed. Thus the ambient dose equivalent for this depth is denoted by $H^*(10)$.

Directional dose equivalent The directional dose equivalent, $H'(d, \Omega)$, at a point of interest in the actual radiation field, is the dose equivalent that would be produced by the corresponding expanded field, in the ICRU sphere at a depth d , on a radius in a specified

direction Ω [22]. For low penetrating radiation, depths of 0.07 mm and 3 mm are employed for the skin and eye respectively. In the particular case of a unidirectional field, the direction can be specified in terms of the angle α between the radius opposing the incident field and the specified radius [23].

b) Operational quantities for individual monitoring

Individual monitoring is usually performed with personal dosimeters worn on the body and the operational quantity defined for this application takes this situation into account [23]. For individual monitoring the concept individual or personal dose equivalent is recommended for both penetrating and low penetrating radiations.

Personal dose equivalent The personal dose equivalent, $H_p(d)$, is the dose equivalent in ICRU tissue at a depth d in a human body below the position where an individual dosimeter is worn [22]. For low penetrating radiation, depths of 0.07 mm and 3 mm are used for monitoring the skin and eye doses respectively. The personal dose equivalent for these depths is then denoted by $H_p(0.07)$ and $H_p(3)$, respectively. For penetrating radiation, a depth of 10 mm is recommended. Thus, to obtain an approximate value for the effective dose we use the ambient dose equivalent, $H^*(10)$, or the personal dose equivalent, $H_p(10)$; while, to obtain an approximate values for the equivalent dose to the skin the operational quantities $H_p(0.07)$ or , $H'(0.07)$ are used.

2.4 Dosimetric methods

2.4.1 Ionizing method

The most widely used method for determining radiation exposure and absorbing dose is based on ionization. Radiation loses energy as it passes through a medium by producing charged particles, electrons and ions or holes. Radiation instruments that are based on this

technique may be either gas filled detectors or solid state detectors.

a) Gas filled detectors

A gas filled detector is usually cylindrical in shape (figure 2.1), with an outer wall (cathode), a central collecting electrode (anode), well insulated from each other, and a sensitive volume of gas. When an ionizing radiation is absorbed in the gas contained by the chamber, electron-ion pairs are produced. The average energy required to create an electron-ion pair is about 30-35 eV. Both electrons and ions move under the influence of an electric field producing an electric current that can be measured, or, through appropriate electronics, the charge produced by the radiation may be converted into an electrical pulse, in which case particles are counted individually. The collection of electron-ion pairs in the gas filled detector is a function of the potential applied to the anode as shown in figure 2.2: curve (a) is for 1 MeV β particles, and curve (b) for 100 keV β particles. If the electric field is too weak, ions that are produced by ionizing radiation can recombine before they are swept to the electrodes, so there will be only partial collection of the charge and no gas amplification occur. This corresponds to the part of the graph A in the figure 2.2. Increasing the applied voltage, the ions and electrons can be accelerated to energies at which they themselves can ionize the gas, thus producing more electrons and ions. This multiplication of electrons called gas amplification or Townsend avalanche. It is most useful in producing a measurable current from a few ions. Various types of gas filled detectors can be classified according to the part of graph where they operate.

Ionization chamber The ionization chamber is operated with the applied voltage in the region B of the graph. It is characterized by complete collections without gas amplification of all the ions produced by the incident radiation. Electrodes are either cylindrical or

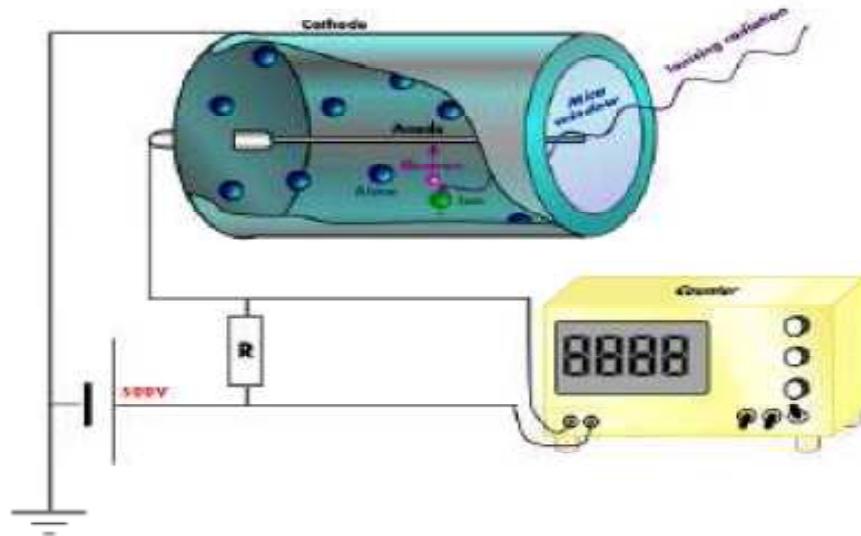


Figure 2.1: Schema of a gas filled detector.

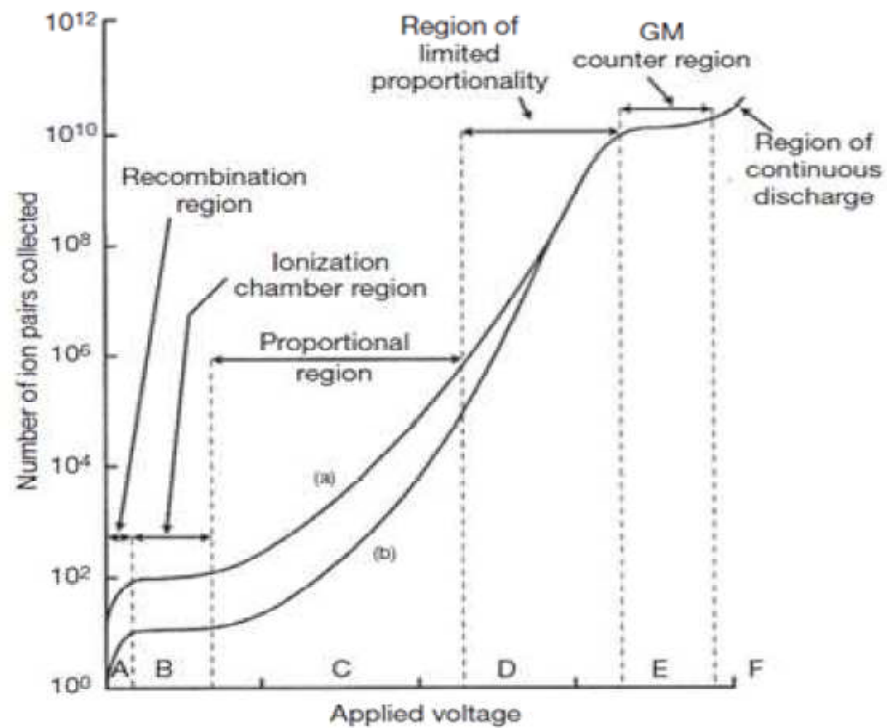


Figure 2.2: Typical behavior at atmospheric pressure for a gas-filled counter [24].

parallel-plate design. The applied voltage is selected to ensure collection of all the ions formed; i.e., it is high enough to prevent recombination of ions created but still on the plateau where the current amplification does not occur. In the ionization chamber the pulse size (the number of ions collected) is always equal to the number of ionizing events produced by the incident radiation, and proportional to the particle energy. The collected charge can be used directly to determine the total energy absorption in the chamber, E_{abs} , whereas:

$$E_{\text{abs}} = \frac{Q \cdot W}{e} \quad (2.15)$$

where Q is the ionization charge and W is the mean energy needed to produce an ion-electron pair. The energy range of ionization chamber is $E > 10$ KeV.

Proportional counter Proportional counter is often cylindrical and contains a mixture of inert and organic gas, but other fillings may be used to form special detectors (e.g. incorporating boron trifluoride (BF_3) allows the detection of neutrons). It is operated at a voltage in the region C of the graph. In this region the applied field is sufficiently high that drifting electrons gain enough energy in neighborhood of the thin central electrode to produce further ion pairs when they collide with other neutral atoms of the gas. So that gas amplification will occur. This amplification makes the detection instrument sensitive to low levels of radiation ($E < 10$ KeV). The amount of charge collected at the electrodes is larger than that in an ionization chamber and it is roughly proportional to the amount of energy deposited in the gas of the counter by the incident radiation. Proportional counters and ionization chambers have both the ability to discriminate between different types and energies of ionizing radiation.

Geiger Mueller counters Geiger Mueller counter (GM) is similar in construction to proportional counter. The voltage applied between a GM's electrodes is high and sufficient to cause an almost complete ionization of the counter gas. The gas amplification avalanche is terminated when the density of secondary ions becomes larger enough so that their field, when added to the applied field, reduces the effective field to less than that needed to sustain gas amplification. The output current is independent of the primary ionization or the energy of interacting particles. Unlike the ionization chambers and proportional counters, Geiger Mueller counters cannot be used to identify the type of radiation being detected.

b) Solid state detectors

It was soon realized that the use of a solid detection medium instead of a gas would be of great advantage in radiation detection applications, as solids are about 1000 times denser than gases and the dimensions of solid detectors could be kept much smaller than those of equivalent gas filled detectors. Semiconductor detectors are solid state devices of crystalline structure that operate essentially as ionization chambers. The charge carriers in semiconductors are not electrons and ions, as in the gas filled detectors, but electrons and holes. The ionizing particle incident upon the semiconducting junction creates electron-hole pairs as it passes through it. Electrons and holes are swept to the anode and cathode electrodes respectively under the influence of an electric field, producing an output pulse that can be recorded. In contrast to gas filled detector, the average energy required to produce an ionizing event in semiconductor detector is 3.5 eV.

2.4.2 Thermoluminescence method

Thermoluminescence (TL) is thermally stimulated phosphorescence; it has found great use in dosimetry. The TL dosimeters (TLD's) are insulators or semiconductors with a crys-

talline structure; therefore the theoretical explanation of thermoluminescence is based on the electron band theory. In an ideal crystal the electrons occupy the valence band which is separated from the conduction band by the so called forbidden band gap [25] (figure 2.3). In reality crystals are not pure; they are doped with impurities or so called activators which allow the electrons to possess forbidden energies. When a radiation interacts with the TL material, it can produce electron-hole pairs (step a). Some of these electrons fall back to the valence band (recombine with holes under emission of light), while the others fall into a trap in the forbidden gap (step b). Putting energy to the TL material (heating) the electron of the trap can be excited to the conduction band again and from there it undergoes recombination with the hole (step e, d) in recombination center R accompanying by emission of thermoluminescence radiation. The latter is detected using a photomultiplier tube. When the reading is done, TLD can be reset by heating it to a high temperature (annealing) to empty all the traps. After proper annealing, the crystal has the same sensitivity as previously, so it can be reused again. The emitted light is a characteristic of the material and a function of the temperature. The intensity of this light is proportional to the number of electrons that are trapped in the holes. The plot of thermoluminescence output versus temperature is known as the glow curve for that particular material. The area under the glow curve gives us an information about the absorbed dose. A schematic glow curve of LiF TLD is shown in figure 2.4. Usually the absorbed dose is determined using the highest peak. The total light output or the area under the glow curve can be compared with that from calibrated TLDs to infer radiation dose [19]. Typically, several peaks occur as traps at different energy levels are emptied [19]. TLDs are at present the most widely used for individual monitoring. Examples of TLD materials are compounds of LiF; $\text{Li}_2\text{B}_3\text{O}_7$, CaSO_4 , Al_2O_3 and CaF_2 doped with various activators. LiF:Mg, Cu, P

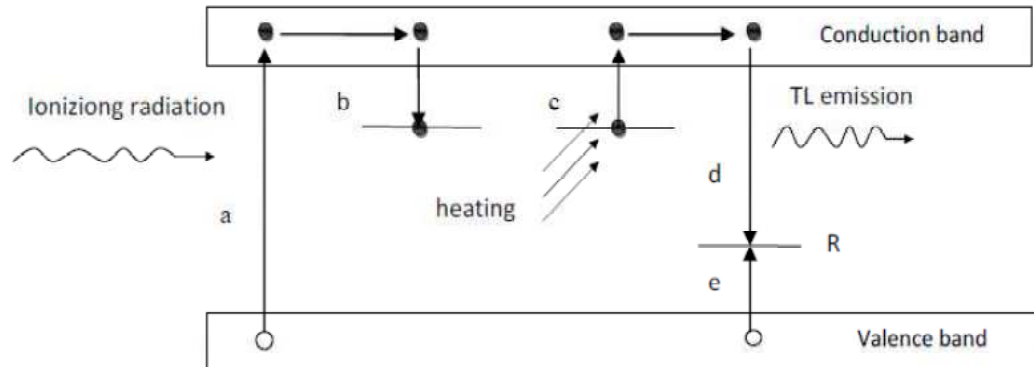


Figure 2.3: Schematic illustration of processes of produced in the crystal by irradiation and a successive heat treatment.

and $\text{Li}_2\text{B}_4\text{O}_7:\text{Mn}$ are commonly used in medical application because of their nearly tissue equivalent. $\text{CaSO}_4:\text{Dy}$, $\text{Al}_2\text{O}_3:\text{C}$ and $\text{CaF}_2:\text{Mn}$ are used because of their high sensitivity. The useful range of TLDs is from about a few mGy to $10^2\text{-}10^3$ Gy.

2.4.3 Chemical method

This technique involves the determination of the absorbed dose by the measurement of chemical changes produced in the medium by ionizing radiation. The best known and most useful chemical dosimeter is the Fricke dosimeter, also called the ferrous sulfate, initiated by Fricke in 1927. The latter consists of an aerated dilute solution of ferrous sulfate in 0.8 N sulfuric acid: 0.001 M FeSO_4 or $\text{Fe}(\text{NH}_4)_2(\text{SO}_4)_2 + 0.8 \text{NH}_2\text{SO}_4$ air saturated. The irradiated of the Fricke solution produces free radicals (e.g. H and OH), which are highly reactive. These radicals can oxidize the ferrous ions Fe^{+2} into the ferric ions Fe^{+3} . The latter exhibits a strong absorption peak at $\lambda = 304$ nm, whereas ferrous ions do not show any absorption at this wavelength. The production of ferric ions is directly proportional to the absorbed dose. The ferric ion concentration can be determined using spectrophotometer, which measures the absorbance of light in the solution. The dose absorbed in the dosimeter

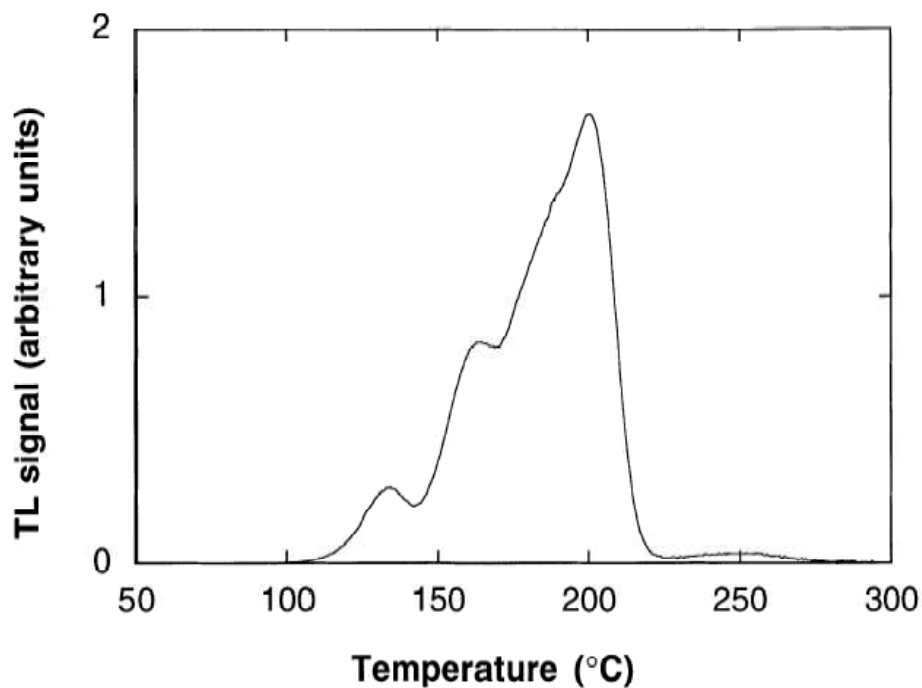


Figure 2.4: Thermoluminescence glow curve of LiF phosphor activated with trace amounts of Mg^{+2} and Ti^{+4} (TLD-100) [26].

solution, D , can be calculated according to the equation:

$$D = \frac{\Delta M}{\rho G(Fe^{+3})} \quad (2.16)$$

where ΔM is the change in molar concentration of product Fe^{+3} due to the irradiation, ρ the density of the Fricke solution ($\rho = 1.024 \times 10^3 \text{ kg/m}^3$), and $G(Fe^{+3})$ the radiation chemical yield of ferric ions, the number of moles of ferric ions produced per joule of the energy absorbed in the solution. The useful range of Fricke dosimeter is from about 40 to 400 Gray [19].

2.4.4 Calorimetric method

Calorimetry is the most fundamental technique for determining absorbed dose quantity. The basic assumption is that all of the energy imparted to the irradiated medium appears as heat, so that the measurement of the absorbed dose reduces to a measurement of a

temperature rise. In an ideal dosimeter, the average energy deposited by ionizing radiation must be equal to the thermal energy. In reality, different materials have either endothermic or exothermic radiochemical reactions which may necessitate a correction factor, called heat defect, to relate the measured temperature change to the energy absorbed. If ΔT is the measured temperature change in the medium, then the absorbed dose of material, D_m , is given by:

$$D_m = C_m \Delta T / (1 - k_{HD})$$

where C_m is the specific heat capacity, the amount of heat required raising the temperature of the entire calorimeter by 1 K, of the calorimetric material and k_{HD} is the heat defect. The heat defect can be positive or negative, and it is given by

$$k_{HD} = (E_a - E_h) / E_a$$

where E_a is the energy absorbed by the irradiated material and E_h is the energy which appears as heat. The absorbed dose depends on both the radiation field and the material in which it interacts. Knowledge of absorbed dose is required for different applied fields involving ionizing radiation, but the most demanding in terms of accuracy is radiotherapy. In this case, the material of interest is tissue and the goal of treatment planning is to predict accurately the absorbed dose received by all irradiated tissues [27]. For this purpose, the water calorimeter has been used. Water is chosen because its radiation absorption characteristics are similar to those of tissue, and because the special distribution of absorbed dose can be measured easily using a movable probe [27]. However, this calorimeter is not widely used to establish directly the absorbed dose to water because of the presence of conductive heat loss (or gain), and the disadvantage of constructing a thermally isolated segment. The most accurate dosimeter is that constructed from graphite. The latter has the same radiation absorption characteristics of water without any loss of heat in other mechanisms (such

as the heat defect). Given the absorbed dose to graphite, the dose to water is obtained using a conversion which usually is based on ionization chamber measurements [27].

Chapter 3

Cosmic ray dosimetry

All living things on Earth are exposed to various forms of ionizing radiation. The main sources of this radiation at ground level are radioactive elements, medical X-ray examinations, and about 10% to 15% of it is due to the by-products of cosmic ray interactions in the atmosphere. The first two sources are absent at high altitudes while the intensity of cosmic radiation is significantly higher than that at ground level. The crew of commercial aircraft spend a large proportion of their working hours at high altitudes, which cause them to be subjected to high level of ionizing radiation. Additional exposure may also occur from solar particle events, particularly at supersonic altitudes at latitudes close to the magnetic poles.

In this chapter we first estimate the cosmic ray spectra (fluence) in the atmosphere with the help of the PARMA¹ model [28-29]. Then we calculate the doses induced by cosmic rays under any global conditions (altitude, cut-off rigidity, and solar activity) using the conversion coefficients from fluence to effective dose. All the results shown in this chapter were obtained by C⁺⁺ code we developed on the basis of the PARMA model. The obtained results are compared with EURADOS experimental data.

¹ PHITS-based Analytical Radiation Model in the Atmosphere

3.1 Cosmic ray spectra in the atmosphere

The radiation field in the Earth's atmosphere is formed by several types of ionizing radiation of a wide range of energies originating mainly from two sources: energetic particles from the Universe, usually referred to as galactic cosmic radiation (GCR), and from the Sun. GCRs in the interstellar space are modulated by solar activity and partly deflected towards the poles when they penetrate the Earth's magnetic field. They undergo a variety of interactions when they enter the the Earth's atmosphere resulting in a cluster of particles such as protons, helium ions, electrons, positrons, photons, neutrons, muons, and pions. The energy of particles coming from the sun is not sufficient to play an important role at ground level, but at flight altitudes the solar particle events may increase the radiation field. However, any rise in dose rate associated with an event is quite rapid, usually taking place in minutes, and substantial solar particle events only occur once every so many years. Based on these considerations, the radiation field at aircraft altitudes can be expressed as a function of three variables, altitude, solar modulation strength, and cut-off rigidity.

PARMA is an analytical model proposed by Sato, *et al* [28-29] for estimating the atmospheric cosmic ray spectra for neutrons, protons, helium ions, muons, electrons, positrons and photons with energies up to 200 GeV/nucleon. It is based on a comprehensive analysis of the results obtained by performing Monte Carlo simulation of cosmic ray propagation in the atmosphere by the Particle and Heavy Ion Transport code System (PHITS) [30]. The unit of the obtained spectra is $\text{cm}^{-2} \text{s}^{-1} \text{MeV}^{-1}$, supplying the force field potential in MV, the vertical cut-off rigidity in GV, and the kinetic energy in MeV except for the case of helium ions, where the kinetic energy is given in MeV/nucleon to estimate its spectra in $\text{cm}^{-2} \text{s}^{-1}(\text{MeV}/\text{nucleon})^{-1}$. In the development of PARMA, the Monte Carlo obtained spectra for the force field potentials 400 and 1200 MV were regarded as the data for the solar

minimum and maximum conditions, respectively, although the highest force field potential adopted in the Monte Carlo simulation was 1800 MV. The Monte Carlo obtained spectra at the altitudes above 20 km ($\sim 59 \text{ g/cm}^2$) were not considered in the derivation of PARMA for the following two reasons: (1) the equilibrium between the numbers of incoming and outgoing particles, which is a necessary condition for calculating lower-energy particle fluxes by our program, is not established at the higher altitudes, and (2) commercial flights never exceed an altitude of 20 km.

3.1.1 Neutron spectra

Figure 3.1 shows the cosmic ray neutron spectra obtained by the code we developed on the basis of the PARMA model. The left and right panels show the atmospheric depth and cut-off rigidity dependence of the spectra, respectively. The flux of neutron in this figure is expressed in terms of per unit of lethargy (Lethargy is the differential of the logarithm of the energy bin, i.e. $\log(E_{\text{up}}) - \log(E_{\text{low}})$). Two peaks around 1 MeV and 100 MeV can be observed in the spectra. The former is attributed to neutrons emitted by the evaporation process, while the latter is attributed to those produced by pre-equilibrium and intranuclear cascade processes. Another peak at thermal energy can be observed only in spectrum at ground level, since it is composed predominantly of the Earth's albedo neutrons.

a) Global condition dependence of cosmic-ray neutron spectrum

To analyze the dependences of the cosmic-ray neutron spectra on the global conditions, the simulations of the atmospheric propagation in semi-infinite atmosphere were performed to obtain reference spectra without the disturbance of the local geometry effects. The semi-infinite atmosphere consists of the dry air only, even at subterranean regions down to 1000 g/cm^2 below sea level. The neutron spectra in the semi-infinite atmosphere, Φ_{Inf} , can be

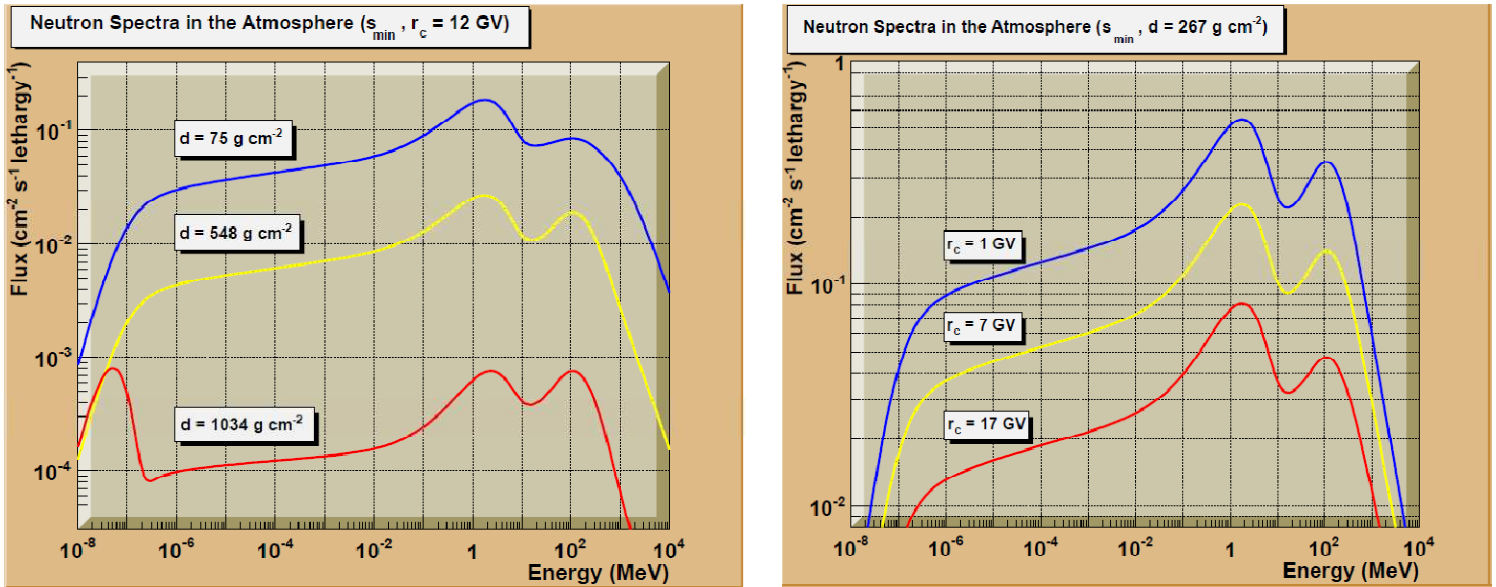


Figure 3.1: The cosmic ray neutron spectra obtained by our program. The left and right panels show the atmospheric depth and cut-off rigidity dependence of the spectra, respectively.

expressed by [29]

$$\Phi_{\text{Inf}}(s, r_c, d, E) = \Phi_{\text{B}}(s, r_c, d, E) \Phi_{\text{L}}(s, r_c, d) \quad (3.1)$$

where Φ_{B} represents the basic spectrum and Φ_{L} is the integrated neutron flux below 15 MeV. s, r_c, d and E denote the solar modulation potential, vertical cut-off rigidity, atmospheric depth and neutron energy, respectively.

Low-energy neutron flux

The low energy neutron fluxes Φ_{L} depends on the atmospheric depth d and it can be expressed by [29]

$$\Phi_{\text{L}}(s, r_c, d) = a_1(s, r_c) \{ \exp[-a_2(s, r_c)d] - a_3(s, r_c) \exp[-a_4(s, r_c)d] \} \quad (3.2)$$

where a_i ($i = 1, 2, \dots$) are the parameters depending on the solar modulation potential and the cut-off rigidity. Their numerical values for each condition were determined by least squares fitting of the Φ_{L} data and they can be written by the equation [29]

$$a_i(s, r_c) = b_{i1}(s) + \frac{b_{i2}(s)}{1 + \exp[(r_c - b_{i3})/b_{i4}]} \quad (3.3)$$

where b_{ij} are parameters related to the solar modulation. The numerical values of b_{ij} are summarized in table 3.1. To estimate Φ_{L} the same calculation procedures of secondary cosmic ray spectra are followed.

Mean basic spectrum

The basic spectrum Φ_{B} depends on the global conditions and it can be expressed by [29]

$$\Phi_{\text{B}}(E) = c_1 \left(\frac{E}{c_2} \right)^{c_3} \exp\left(\frac{-E}{c_2} \right) + c_4 \exp\left\{ \frac{-[\log_{10}(E) - \log_{10}(c_5)]^2}{2[\log_{10}(c_6)]^2} \right\} \quad (3.4)$$

$$+c_7 \log_{10} \left(\frac{E}{c_8} \right) \left\{ 1 + \tanh \left[c_9 \log_{10} \left(\frac{E}{c_{10}} \right) \right] \right\} \\ \times \left\{ 1 - \tanh \left[c_{11} \log_{10} \left(\frac{E}{c_{12}} \right) \right] \right\}$$

where c_i are constant parameters. The numerical values of the parameters c are listed in table 3.2. At energies above 15 MeV, where the basic spectrum Φ_B depends on the global conditions, the parameters c_4 and c_{12} are related to the atmospheric depth and the cut-off rigidity, and they can be expressed by [29]

$$c_4(r_c, d) = a_5(r_c) + \frac{a_6 d}{1 + a_7 \exp(a_8 d)} \quad (3.5)$$

Table 3.1: Numerical values of the parameters b^2 [29].

unit of a_i	b_{i1}	$b_{i2}(\text{GV}^{-1})$	b_{i3}	$b_{i4}(\text{GV})$	$b_{i5}(\text{GV})$
$a_1(\text{cm}^{-2}\text{s}^{-1})$	25.7	-0.509	7.47	12.3	1.05
	(-6.92)	(1.13)	(27)	(11.7)	(2.62)
$a_2(\text{cm}^{-2}\text{g}^{-1})$	6.51×10^{-3}	3.35×10^{-5}	9.44×10^{-4}	12.1	2.78
	(5.32×10^{-3})	(8.49×10^{-5})	(2.07×10^{-3})	(11.7)	(3.81)
a_3	0.984	1.50×10^{-4}	-0.732	-1.44	2.74
	(0.975)	(6.47×10^{-4})	(-0.228)	(2.07)	(2.17)
$a_4(\text{cm}^{-2}\text{g}^{-1})$	8.87×10^{-3}	-4.33×10^{-5}	1.73×10^{-2}	-1.08	2.66
	(9.14×10^{-3})	(-6.49×10^{-5})	(5.82×10^{-3})	(1.02)	(2.45)

$$c_{12}(r_c, d) = a_9(r_c) \{ \exp[-a_{10}(r_c)d] + a_{11}(r_c) \exp(-a_{12}d) \} \quad (3.6)$$

where a_5 to a_{12} are free parameters, and only a_5 , a_9 , a_{10} and a_{11} are related to the cut-off rigidity. The numerical values of the parameters can be obtained by the least-squares fitting of the parameters c_4 and c_{12} . The parameters a_5 , a_9 , a_{10} and a_{11} can be estimated using Eq

² The values in parentheses are the data for the solar maximum, while the others are those for the solar minimum.

(3.3). Table 3.3 summarizes the numerical values of the parameters b . The basic spectrum Φ_B can be determined for each condition by replacing the parameters listed in table 3.2 and the c_4 and c_{12} values obtained from Eqs. (3.5) and (3.6), respectively into Eq (3.4). The neutron spectra in the semi-infinite atmosphere Φ_{Inf} can be predicted by multiplying Φ_B by Φ_L obtained from Eq (3.2), as indicated by Eq (3.1).

b) Local geometry condition dependence of cosmic-ray neutron spectrum

Table 3.2: Numerical values of the parameters c [29].

unit of c_i	c_i
$c_1(\text{lethargy}^{-1})$	0.236
$c_2(\text{MeV})$	2.38
c_3	0.726
* $c_4(\text{lethargy}^{-1})$	0.0536
$c_5(\text{MeV})$	124
$c_6(\text{MeV})$	2.23
$c_7(\text{lethargy}^{-1})$	0.00108
$c_8(\text{MeV})$	3.64×10^{-12}
c_9	1.66
$c_{10}(\text{MeV})$	8.48×10^{-8}
c_{11}	1.51
* $c_{12}(\text{MeV})$	302

*Dependent on the global conditions assumed for estimating Φ_B .

In practice, the cosmic-ray neutron spectra are influenced on the water density around the point of interest at ground level and the structure of the aircraft at higher altitudes. For the purpose of reproducing the neutron spectra at the ground level Φ_G by an analytical

function, the following equation was proposed by [29]

$$\Phi_G(s, r_c, d, E, w) = \Phi_L(s, r_c, d) [\Phi_B(s, r_c, d, E) f_G(E, w) + \Phi_T(E, w)] \quad (3.7)$$

where w is weight fraction of water, $f_G(E, w)$ denotes the functions representing the disturbance of the spectrum due to the local geometry effect, and $\Phi_T(E, w)$ expresses the thermal neutron peak. The function $f_G(E, w)$ can be estimated by [29]

Table 3.3: Numerical values of the parameters a and b [29].

unit of a_i	function	a_i or b_{i1}	b_{i2} (GV ⁻¹)	b_{i3}	b_{i4} (GV)	b_{i5} (GV)
a_5 (lethargy ⁻¹)	Eq. (3.20)	9.73×10^{-4}	-9.66×10^{-5}	1.21×10^{-2}	7.17	1.46
a_6 (cm ² g ⁻¹ lethargy ⁻¹)	constant	1.89×10^{-4}				
a_7	constant	0.448				
a_8 (cm ² g ⁻¹)	constant	0.00144				
a_9 (MeV)	Eq. (3.20)	5.72×10^2	7.13	-1.07×10^2	1.85	1.21
a_{10} (cm ² g ⁻¹)	Eq. (3.20)	6.86×10^{-4}	2.71×10^{-5}	5.78×10^{-4}	8.85	3.64
a_{11}	Eq. (3.20)	-0.508	0.148	1.01	9.16	1.64
a_{12} (cm ² g ⁻¹)	constant	0.0141				

$$\log_{10} [f_G(E, w)] = g_1 + g_2 \log_{10} \left[\frac{E}{g_3(w)} \right] \left[1 - \tanh \left\{ g_4 \log_{10} \left[\frac{E}{g_5(w)} \right] \right\} \right] \quad (3.8)$$

where g_1, g_2, g_4 are constant parameters and their numerical values are listed in table 3.4.

The parameters g_3, g_5 and g_6 are related to the weight fraction of water, w , and they can be determined by [29]

$$\log_{10} [g_3(w)] = h_{31} \frac{h_{32}}{w + h_{33}} \quad (3.9)$$

$$g_5(w) = h_{51} + h_{52}w + h_{53}w^2 \quad (3.10)$$

$$g_6(w) = \frac{h_{61} + h_{62} \exp(-h_{63}w)}{1 + h_{64} \exp(-h_{65}w)} \quad (3.11)$$

where h_{3j} , h_{5j} , h_{6j} are fitting constants determined by the least-squares fitting of the parameters g_3 , g_5 , g_6 data respectively. Table 3.5 summarizes the numerical values of the parameters h . The spectrum of the thermal neutron peak can be expressed by [29]

$$\Phi_T(E, w) = g_6(w) \left(\frac{E}{E_T}\right)^2 \exp\left(\frac{-E}{E_T}\right) \quad (3.12)$$

where $E_T = 2.5 \times 10^{-8}$ MeV represents the thermal energy. The neutron spectra at ground level is determined by substituting the values of Φ_L , Φ_B , Φ_T and $f_G(E, w)$ into Eq (3.7).

Table 3.4: Numerical values of the parameters g [29].

unit of g_i	g_i	³ g_{i1}	⁴ g_{i2}
g_1	-0.0235	-0.0379	-0.121
g_2	-0.0129	-0.0179	-0.0220
g_3 (MeV)	Eq.(3.26)	6.03×10^{-8}	5.42×10^{-10}
g_4	0.969	1.36	1.40
g_5 (MeV)	Eq.(3.27)	5.52	6.45

At high altitudes the cosmic ray neutron spectra are influenced by the configuration of aircraft. To represent the disturbance of the spectrum due to aircraft, the function f_{A1} , similar to that describing f_G is written by [29]

Table 3.5: Numerical values of the parameters h [29].

unit of g_i	h_{i1}	h_{i2}	h_{i3}	h_{i4}	h_{i5}
g_3 (MeV)	-25.2	2.73	0.0715		
g_5 (MeV)	0.348	3.35	-1.57		
g_6 (lethargy ⁻¹)	0.118	0.144	3.87	0.653	42.8

³ Location of a pilot.

⁴ Location of a cabin passenger.

$$\log_{10} [f_{Al}(E, m_A)] = g_{1l} + g_{2l} \log_{10} \left[\frac{E}{g_{3l}} \right] \left[1 - \tanh \left\{ g_{4l} \log_{10} \left[\frac{E}{g_{5l}} \right] \right\} \right] \quad (3.13)$$

where l indicates the location of interest, i.e. of a pilot or a passenger, g_{1l} to g_{5l} are the fitting constants, and m_A and m_{A340} denote the mass of the aircraft being considered, and Airbus-340, respectively. The numerical values of g_{il} are listed in table 3.4. The cosmic ray neutron spectra in aircraft is given by

$$\Phi_{AL}(s, r_c, d, m_A) = \Phi_L(s, r_c, d) \Phi_B(s, r_c, d, E) f_{Al}(E, m_A) \quad (3.14)$$

3.1.2 Proton and helium ion spectra

Figure 3.2 shows the cosmic ray proton and helium ion spectra obtained by our program. The left and right panels show the atmospheric depth and the cut-off rigidity dependence of the spectra, respectively. It is evident from the data in the figure that the spectra can be divided into higher and lower energy components, although they are not clearly distinguished in the case of protons. The two components consist predominantly of primary cosmic rays and their secondary particles that are produced in atmosphere. The gap between the two components is generated by the cut-off effect of primary cosmic rays due to the magnetosphere. We first introduce the analytical functions used for estimation of primary cosmic rays then the secondary particles and finally the combination between them.

a) Primary spectra

Considering the energy loss and nuclear interactions in the atmosphere, the primary proton and helium-ion spectra Φ_{pri} can be assumed to be expressed by [28]

$$\Phi_{pri}(s, d, E) = \Phi_{TOA}(s, E + a_1 d) \times [a_2 \exp(-a_3 d) + (1 - a_2) \exp(-a_4 d)] \quad (3.15)$$

where s , d and E denote the force field potential, the atmospheric depth and the kinetic

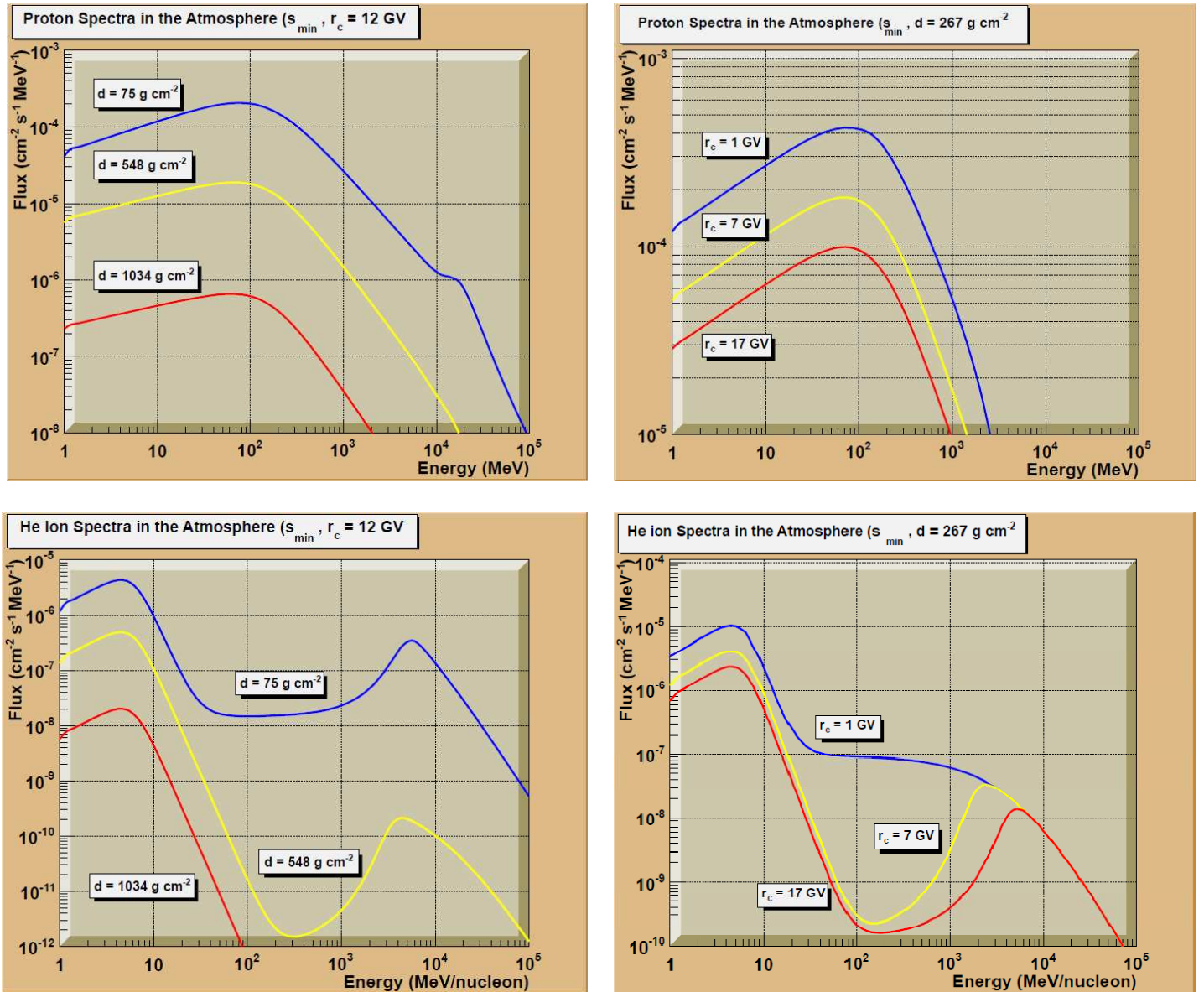


Figure 3.2: The cosmic ray proton and helium ion spectra obtained by our program. The left and right panels show the atmospheric depth and the cut-off rigidity dependence of the spectra, respectively.

energy per nucleon, respectively, and Φ_{TOA} is the spectra at the top of the atmosphere. The parameter a_1 is related to the particle stopping power of the atmosphere, and consequently $E + a_1 d$ indicates the kinetic energy at the top of the atmosphere. The two exponential decay terms represent the decrease in the primary-particle fluxes due to nuclear interactions, and a_i are fitting parameters. The numerical values of these parameters are summarized in table 3.6.

In the least squares fitting, Φ_{TOA} was obtained from the local interstellar (LIS) spectra calculated by the Nymmik model [31] coupled with modified parameters. It can be expressed by [28]

$$\Phi_{\text{TOA}}(s, E) = \frac{C(E_{\text{LIS}})[\beta(E_{\text{LIS}})]^{a_5}}{[R(E_{\text{LIS}})]^{a_6}} \left[\frac{R(E)}{R(E_{\text{LIS}})} \right]^2 \quad (3.16)$$

where $E_{\text{LIS}} = E + sZ/A$ is the kinetic energy at LIS spectra, β is the speed of the particle relative to light, and R is the rigidity of the particle in GV, which can be obtained from the equation $R = 0.001 \times \sqrt{(AE)^2 + 2AE_m E} / Z$, where A , Z and E_m are the mass and charge number and the rest mass of the particle, respectively. The parameter C depends on the particle energy and it can be written by [28]

$$C(E) = a_7 + \frac{a_8}{1 + \exp[(E - a_9)/a_{10}]} \quad (3.17)$$

It should be noted that Eqs (3.16) and (3.17) coupled with the parameters listed in table 3.6 give the particle spectra in the unit of $\text{s}^{-1}\text{m}^{-2} \text{sr}^{-1} \text{GV}^{-1}$. Thus they should be multiplied by $(4\pi - \Omega_E) \times (A/Z)/\beta \times 10^{-7}$, where $\Omega_E = 1.675\pi$ is the solid angle of the Earth from a point at the top of the atmosphere, to convert that unit into the one used in the least squares fitting of terrestrial proton and helium ion spectra, $\text{cm}^{-2}\text{s}^{-1}(\text{MeV}/\text{nucleon})^{-1}$.

b) Secondary spectra

To estimate the dependences of the secondary proton and helium ion spectra on the global conditions, Φ_{sec} was introduced by [28]

$$\Phi_{\text{sec}}(s, r_c, d) = \Phi_N(s, r_c, d) + \frac{b_1(d) E^{b_2(d)}}{1 + b_3(d) E^{b_4(d)}} \quad (3.18)$$

Table 3.6: Numerical values of the parameters $a_i (i = 1, 2, \dots, 16)$ [28].

Parameter	Protons	Helium ions
$a_1(\text{cm}^2 \text{g}^{-1} \text{MeV/nucleon})$	2.12	17.6
a_2	0.445	0.438
$a_3(\text{cm}^2 \text{g}^{-1})$	0.0101	0.0121
$a_4(\text{cm}^2 \text{g}^{-1})$	00396	0.0434
a_5	2.924	1.841
a_6	2.708	2.646
$a_7(\text{s}^{-1} \text{m}^{-2} \text{sr}^{-1} \text{GV}^{-1})$	1.27×10^4	2.36×10^3
$a_8(\text{s}^{-1} \text{m}^{-2} \text{sr}^{-1} \text{GV}^{-1})$	4.83×10^3	432
$a_9(\text{MeV/nucleon})$	3.28×10^4	6.06×10^3
$a_{10}(\text{MeV/nucleon})$	7.44×10^3	2.41×10^3
a_{11}	3.46	3.33
a_{12}	1.68	11.7
a_{13}	1.37	0.967
$a_{14}(\text{cm}^2 \text{g}^{-1} \text{MeV/nucleon})$	2.07	3.20
$a_{15}(\text{MeV/nucleon})$	108	15.0
$a_{16}(\text{MeV/nucleon})$	2.30×10^3	853

where b_i are free fitting parameters and they are assumed to be dependent on d and is

given by [28]

$$b_i(d) = c_{i1} + c_{i2}d + c_{i3}d^2 + c_{i4}d^3 \quad (3.19)$$

where the parameters c_{ij} are the fitting constants. Table 3.7 summarizes the numerical values of the parameters c_{ij} obtained from the least-squares fitting of the b_i data. Φ_N represents the flux used for the normalization of the spectra, i.e. flux at 1 MeV. For solar minimum condition (or solar maximum by replacing the subscript min with max), Φ_N can be expressed by [28]

$$\Phi_{N \min}(r_c, d) = g_{1 \min}(r_c) \{ \exp[-g_{2 \min}(r_c)d] - g_{3 \min}(r_c) \exp[-g_{4 \min}(r_c)d] \} \quad (3.20)$$

where the parameters g_{ij} depend on the cut-off rigidity r_c and can be determined by the equation

$$g_i(r_c) = h_{i1} + h_{i2}r_c + \frac{h_{i3}}{1 + \exp[(r_c - h_{i4})/h_{i5}]} \quad (3.21)$$

where h_{i1} to h_{i5} are free parameters. The numerical values of the parameters h_{ij} for the solar minimum and maximum conditions were determined from the least-squares fitting of the Monte Carlo-obtained Φ_N data for the force field potentials 400 and 1200 MV, respectively. The results of this least-squares fitting are summarized in Table 3.8. To determine Φ_N for arbitrary solar conditions, we assumed that the dependence of Φ_N on the force field potential s can be written by the equation [28]

$$\Phi_N(s, r_c, d) = f_1(r_c, d) + f_2(r_c, d) s^{f_3(r_c, d)} \quad (3.22)$$

where f_i are the parameters depending on r_c and d . The parameter, $f_3(r_c, d)$, generally increases with increasing depth, and it can be represented by the linear function [28]

$$f_3(r_c, d) = g_5(r_c) + g_6(r_c)d \quad (3.23)$$

The parameters $f_1(r_c, d)$ and $f_2(r_c, d)$ were determined by solving the simultaneous equations

$$\begin{cases} \Phi_{N\min}(s, r_c, d) = f_1(r_c, d) + f_2(r_c, d) s_{\min}^{f_3(r_c, d)} \\ \Phi_{N\max}(s, r_c, d) = f_1(r_c, d) + f_2(r_c, d) s_{\max}^{f_3(r_c, d)} \end{cases} \quad (3.24)$$

using f_3 , and $\Phi_{N\min}$ and $\Phi_{N\max}$ calculated by Eqs (3.25) and (3.20), respectively. For arbitrary solar conditions, Φ_N can be estimated by substituting the obtained f_i parameters in Eq (3.24). To estimate the secondary particle spectra, we replace b_i and Φ_N calculated by Eqs (3.19) and (3.24), respectively into Eq (3.18).

c) Combining primary and secondary spectra

Considering the influence of the cut-off rigidity, the terrestrial cosmic ray proton and helium ion spectra Φ can be estimated from their primary and secondary spectra by [28]

$$\begin{aligned} \Phi(s, r_c, d, E) = & \Phi_{\text{pri}}(s, d, E) [\tanh(a_{11} [E/E_{s1}(r_c, d) - 1]) + 1] / 2 \\ & + \Phi_{\text{sec}}(s, r_c, d, E) [\tanh(a_{12} [1 - E/E_{s2}(r_c, d)]) + 1] / 2 \end{aligned} \quad (3.25)$$

where E_{si} is the switching energy between the primary and secondary spectra and it can be determined from r_c and d by the equation [28]

$$E_s(r_c, d) = a_{13} [E_c(r_c) - a_{14}d] \quad (3.26)$$

where E_c corresponds to the cut-off energy of the particle at the top of the atmosphere and it can be obtained by $E_c = \left[\sqrt{(1000 \times r_c Z)^2 + E_m^2} - E_m \right] / A$. In general, the switching energy for the primary spectra E_{s1} is equal to that for the secondary spectra E_{s2} and they can be determined by [28]

Table 3.7: Numerical Values of the parameters c [28].

Parameter	c_{i1}	c_{i2}	c_{i3}	c_{i4}	
Protons	b_1	1.26	0.00323	-4.81×10^{-6}	2.28×10^{-9}
	b_2	0.438	-5.58×10^{-4}	7.84×10^{-7}	-3.87×10^{-10}
	b_3	1.81×10^{-4}	-5.18×10^{-7}	7.59×10^{-10}	-3.82×10^{-13}
	b_4	1.71	7.16	-9.32×10^{-7}	5.27×10^{-10}
Helium ions	b_1	1.00			
	b_2	0.881			
	b_3	1.80×10^{-4}			
	b_4	4.77			
Electrons	b_1	6.44	0.0266	-5.97×10^{-5}	4.93×10^{-8}
	b_2	-0.894	-3.58×10^{-4}	2.37×10^{-7}	5.39×10^{-11}
	b_3	0.00231	8.07×10^{-6}	-2.00×10^{-8}	1.89×10^{-11}
	b_4	1.13	6.64×10^{-4}	-1.04×10^{-6}	3.13×10^{-10}
Positrons	b_1	2.29	0.0124	-2.94×10^{-5}	2.08×10^{-8}
	b_2	-0.455	-7.14×10^{-4}	1.17×10^{-6}	-5.13×10^{-10}
	b_3	0.00387	-5.82×10^{-6}	6.76×10^{-9}	2.93×10^{-12}
	b_4	1.28	8.82×10^{-4}	-1.31×10^{-6}	4.22×10^{-10}
Photons	b_1	15.8	0.00963	-2.22×10^{-5}	2.53×10^{-8}
	b_2	-1.25	8.44×10^{-4}	-2.14×10^{-6}	1.36×10^{-9}
	b_3	0.0121	2.47×10^{-5}	-5.33×10^{-8}	2.79×10^{-11}
	b_4	0.825	0.00134	-2.18×10^{-6}	1.15×10^{-9}

$$E_{s1}(r_c, d) = \max[a_{15}, E_s(r_c, d)] \quad (3.27)$$

$$E_{s2}(r_c, d) = \max[a_{16}, E_s(r_c, d)]$$

The proton and helium-ion spectra is obtained by substituting all the parameters and equations given above into Eq. (3.27).

3.1.3 Electron, positron, photon spectra

Figure 3.3 represents the fluxes of electron, positron and photon as a function of energy obtained by our program. The left and right panels show the atmospheric depth and cut-off rigidity dependence of the spectra, respectively.

All electrons, positrons and photons were generated in the Earth system, i.e. were secondary particles, thus their spectra can be estimated in manner similar to the secondary proton spectra described before. The difference between the secondary proton spectra and the others is that the electron, positron and photon spectra are normalized to their fluxes at 10 MeV instead of those at 1 MeV. This is because the photon fluxes below a few MeV are influenced by the cut-off rigidity and thus are inadequate for use in the normalization of the spectra.

3.1.4 Muon spectra

Figure 3.4 shows the dependence of muon spectra on the atmospheric depth and cut-off rigidity. Although all of the cosmic-ray muons are secondary particles, as are the electrons, positrons and photons, while their spectra cannot be estimated by the same procedure, i.e. normalizing their spectra to their flux at a certain energy. This is because the atmospheric depth dependence of the muon fluxes even at lower energies cannot be expressed by Eq (3.20) because the strong penetrability of muons prevents equilibrium between the numbers of incoming and outgoing particles. Thus, the atmospheric muon fluxes for solar minimum condition (or solar maximum by replacing the subscript min with max) can be expressed by [28]

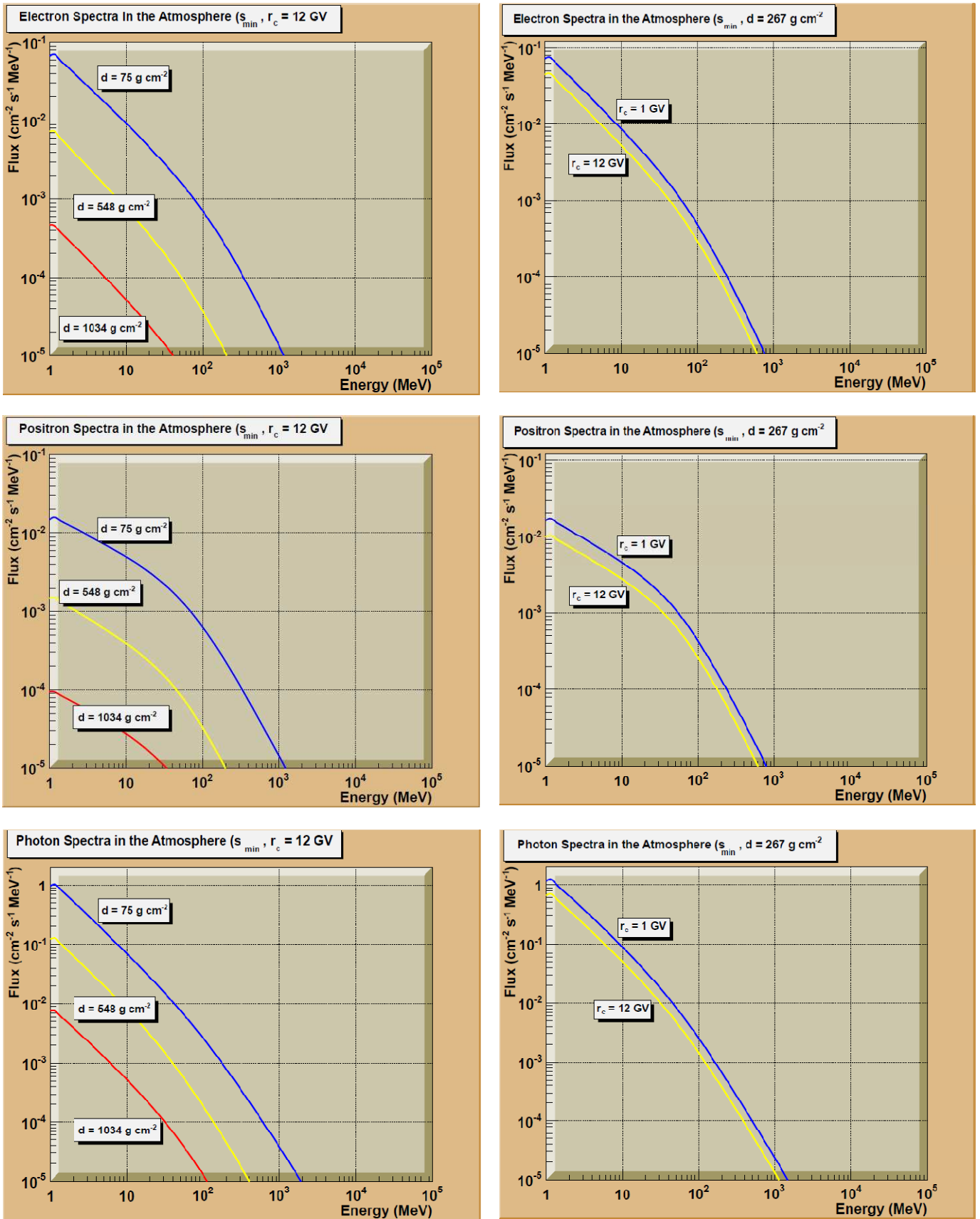


Figure 3.3: The cosmic ray electron, positron and photon obtained by our program. The left and right panels show the atmospheric depth and cut-off rigidity dependence of the spectra, respectively.

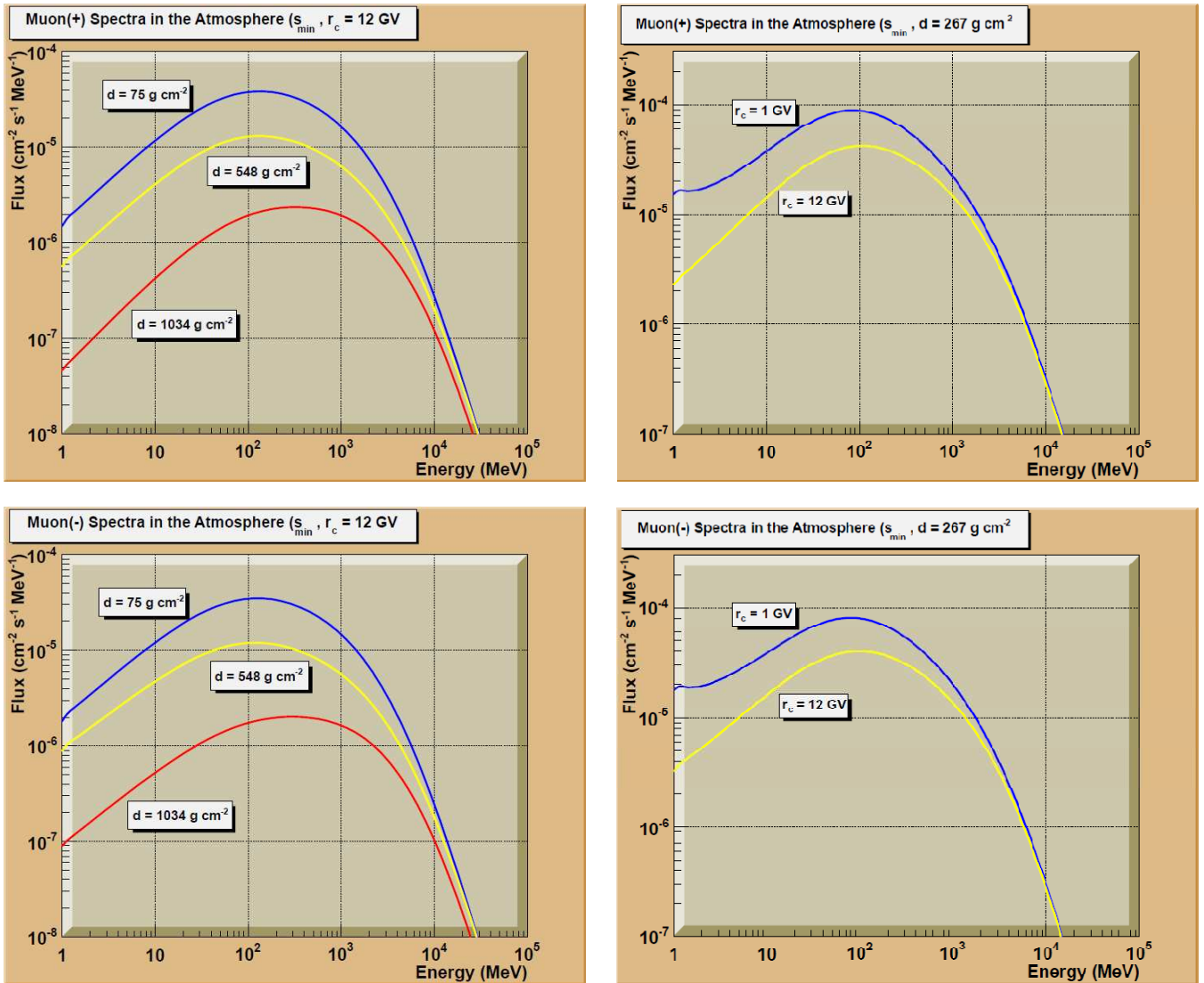


Figure 3.4: The cosmic ray muon spectra obtained by our program. The left and right panels show the atmospheric depth and cut-off rigidity dependence of the spectra, respectively.

$$\Phi_{\mu \min}(r_c, d, E) = \Phi_{\mu}(d) \left[E + \frac{t_1 \min(r_c, d) + t_2 \min(r_c, d) \log_{10}(E)}{\beta^{t_3 \min(r_c, d)}} \right]^{-\alpha_3} \quad (3.28)$$

where $\alpha_3 = 3.7$ and t_i are parameters related to the mean ionization energy loss of muons during the transport through the atmosphere. They can be expressed by [28]

$$t_i(r_c, d) = \nu_{i1}(r_c) + \nu_{i2}(r_c)d + \nu_{i3}(r_c)d^2 + \nu_{i4}(r_c)d^3 + \nu_{i5}(r_c)d^4 \quad (3.29)$$

where ν_{ij} are parameters related to the solar modulation and the cut-off rigidity. For expressing the dependence of ν_{ij} on r_c , a function with the same form as Eq. (3.21) was employed, and it can be written by [28]

$$\nu_{ij}(r_c) = w_{ij1} + w_{ij2}r_c + \frac{w_{ij3}}{1 + \exp[(r_c - w_{ij4})/w_{ij5}]} \quad (3.30)$$

where w_{ijk} are free parameters. Φ_{μ} is an index for the high-energy muon fluxes at the atmospheric depth d . For a best-fit curve to Φ_{μ} , a function with the form similar to Eq. (3.20) was introduced, and it can be written by [28]

$$\Phi_{\mu}(d) = u_1 [\exp(-u_2d) - u_3 \exp(-u_4d)] + u_5 \quad (3.31)$$

where u_i are free parameters. The numerical values of the parameters u_i together with w_{ijk} for the solar minimum and maximum conditions were determined from the least squares fitting of the Monte Carlo-obtained data for the force field potentials 400 and 1200 MV, respectively. The results of the fitting are summarized in table 3.9.

Table 3.8: Numerical values of the parameters h used in Eq. (3.7) for expressing the cut-off rigidity dependence of the g data [30].

Parameter		h_{i1}	$h_{i2}(\text{GV}^{-1})$	h_{i3}	$h_{i4}(\text{GV})$	$h_{i5}(\text{GV})$
Proton	$g_{1\text{min}}(\text{cm}^{-2}\text{s}^{-1})$	0,00244	$-6,03 \times 10^{-5}$	0,00220	6,68	0,932
	$g_{1\text{max}}(\text{cm}^{-2}\text{s}^{-1})$	0,00255	$-7,18 \times 10^{-5}$	0,00146	6,92	0,994
	$g_{2\text{min}}(\text{cm}^2\text{g}^{-1})$	0,00779	$-9,58 \times 10^{-6}$	$6,22 \times 10^{-4}$	7,78	1,85
	$g_{2\text{max}}(\text{cm}^2\text{g}^{-1})$	0,00768	$-2,41 \times 10^{-6}$	$6,64 \times 10^{-4}$	7,75	1,94
	$g_{3\text{min}}$	0,963	0,00160	-0,0712	2,23	0,788
	$g_{3\text{max}}$	0,974	0,00106	-0,0214	3,01	0,918
	$g_{4\text{min}}(\text{cm}^2\text{g}^{-1})$	0,00781	$9,71 \times 10^{-11}$	$8,24 \times 10^{-4}$	8,51	2,31
	$g_{4\text{max}}(\text{cm}^2\text{g}^{-1})$	0,00735	$2,56 \times 10^{-5}$	0,00125	8,19	2,94
	g_5	0,191	0,0703	-0,645	2,03	1,30
	$g_6(\text{cm}^2\text{g}^{-1})$	$5,71 \times 10^{-4}$	$6,13 \times 10^{-6}$	$5,47 \times 10^{-4}$	1,11	0,837
He Nucleus	$g_{1\text{min}}(\text{cm}^{-2}\text{s}^{-1})$	$-2,00 \times 10^{-5}$	$1,79 \times 10^{-6}$	$9,01 \times 10^{-5}$	6,87	4,82
	$g_{1\text{max}}(\text{cm}^{-2}\text{s}^{-1})$	$-5,21 \times 10^{-5}$	$3,81 \times 10^{-6}$	$9,88 \times 10^{-5}$	8,26	3,81
	$g_{2\text{min}}(\text{cm}^2\text{g}^{-1})$	0,00566	$7,51 \times 10^{-5}$	0,00275	8,20	4,96
	$g_{2\text{max}}(\text{cm}^2\text{g}^{-1})$	0,00524	$9,97 \times 10^{-5}$	0,00309	8,21	4,67
	$g_{3\text{min}}$	0,925	0,00260	-0,828	-0,637	1,90
	$g_{3\text{max}}$	0,918	0,00332	-0,133	2,26	1,41
	$g_{4\text{min}}(\text{cm}^2\text{g}^{-1})$	0,00893	$-5,75 \times 10^{-5}$	$7,47 \times 10^{-4}$	5,53	1,34
	$g_{4\text{max}}(\text{cm}^2\text{g}^{-1})$	0,00831	$-3,19 \times 10^{-5}$	$9,70 \times 10^{-4}$	7,85	3,74
	g_5	0,212	0,0769	-0,620	2,47	1,43
	$g_6(\text{cm}^2\text{g}^{-1})$	$5,57 \times 10^{-4}$	$-1,81 \times 10^{-4}$	$4,56 \times 10^{-4}$	0,943	1,25
Electron	$g_{1\text{min}}(\text{cm}^{-2}\text{s}^{-1})$	0,0466	-0,00111	0,0234	6,80	2,69
	$g_{1\text{max}}(\text{cm}^{-2}\text{s}^{-1})$	0,0125	$4,30 \times 10^{-4}$	0,0410	9,16	4,35
	$g_{2\text{min}}(\text{cm}^2\text{g}^{-1})$	0,00690	$-8,92 \times 10^{-6}$	$6,86 \times 10^{-4}$	7,31	3,51
	$g_{2\text{max}}(\text{cm}^2\text{g}^{-1})$	0,00648	$9,61 \times 10^{-6}$	$8,85 \times 10^{-4}$	8,93	4,22
	$g_{3\text{min}}$	1,04	0,00554	-0,0808	4,49	1,56
	$g_{3\text{max}}$	1,06	0,00416	-0,0513	5,70	2,11
	$g_{4\text{min}}(\text{cm}^2\text{g}^{-1})$	0,0161	$-1,64 \times 10^{-10}$	0,00253	4,61	3,42
	$g_{4\text{max}}(\text{cm}^2\text{g}^{-1})$	0,0166	$-3,07 \times 10^{-5}$	0,00104	6,63	1,89
	g_5	0,464	0,0255	-0,330	3,79	1,33
	$g_6(\text{cm}^2\text{g}^{-1})$	$-8,21 \times 10^{-5}$	$-1,07 \times 10^{-5}$	0,00103	1,19	4,86
Positron	$g_{1\text{min}}(\text{cm}^{-2}\text{s}^{-1})$	0,0284	$-7,92 \times 10^{-4}$	0,00963	6,43	2,16
	$g_{1\text{max}}(\text{cm}^{-2}\text{s}^{-1})$	0,00702	$2,24 \times 10^{-4}$	0,0223	8,92	4,29
	$g_{2\text{min}}(\text{cm}^2\text{g}^{-1})$	0,00655	$6,30 \times 10^{-6}$	0,00119	6,88	4,54

	$g_{2\max}(\text{cm}^2\text{g}^{-1})$	0,00633	$1,63\times 10^{-5}$	0,00109	8,61	4,47
	$g_{3\min}$	1,07	0,00536	-0,240	1,92	2,87
	$g_{3\max}$	1,07	0,00532	-0,0678	5,37	1,47
	$g_{4\min}(\text{cm}^2\text{g}^{-1})$	0,0170	$-6,99\times 10^{-6}$	0,00255	4,84	3,08
	$g_{4\max}(\text{cm}^2\text{g}^{-1})$	0,0167	$-2,52\times 10^{-8}$	0,00213	6,48	3,62
	g_5	0,463	0,0255	-0,329	3,78	1,33
	$g_6(\text{cm}^2\text{g}^{-1})$	$-7,12\times 10^{-5}$	$-1,13\times 10^{-5}$	0,00102	1,04	4,85
Photon	$g_{1\min}(\text{cm}^{-2}\text{s}^{-1})$	0,528	-0,0146	0,208	5,86	2,58
	$g_{1\max}(\text{cm}^{-2}\text{s}^{-1})$	0,150	0,00277	0,414	8,70	4,69
	$g_{2\min}(\text{cm}^2\text{g}^{-1})$	0,00532	$4,99\times 10^{-5}$	0,00271	7,90	7,21
	$g_{2\max}(\text{cm}^2\text{g}^{-1})$	0,00523	$5,20\times 10^{-5}$	0,00249	9,01	7,25
	$g_{3\min}$	1,07	0,00291	-0,145	0,00622	3,42
	$g_{3\max}$	1,06	0,00300	-0,0318	4,84	1,75
	$g_{4\min}(\text{cm}^2\text{g}^{-1})$	0,0139	$-1,71\times 10^{-5}$	0,00135	5,38	2,16
	$g_{4\max}(\text{cm}^2\text{g}^{-1})$	0,0140	$-2,47\times 10^{-5}$	$7,20\times 10^{-4}$	7,27	1,70
	g_5	0,464	0,0255	-0,329	3,79	1,33
		$g_6(\text{cm}^2\text{g}^{-1})$	$-5,75\times 10^{-5}$	$-1,19\times 10^{-5}$	$9,58\times 10^{-4}$	1,41

Table 3.9: Numerical values of the parameters u_i , w_{ijk} and h_{ij} used in Eqs. (3.32), (3.33) and (3.7), respectively, to estimate the atmospheric muon spectra [30].

Parameter	μ^+					\square	μ^-				
	u_1	u_2	u_3	u_4	u_5		u_1	u_2	u_3	u_4	u_5
Φ_μ	$6,26\times 10^9$	0,00343	1,01	0,00418	$3,75\times 10^8$		$5,82\times 10^9$	0,00362	1,02	0,00451	$3,20\times 10^8$
Parameter	w_{ij1}	$w_{ij2}(\text{GV}^{-1})$	w_{ij3}	$w_{ij4}(\text{GV})$	$w_{ij5}(\text{GV})$		w_{ij1}	$w_{ij2}(\text{GV}^{-1})$	w_{ij3}	$w_{ij4}(\text{GV})$	$w_{ij5}(\text{GV})$
$v_{11\min}$	$2,05\times 10^3$	126	$-1,01\times 10^3$	6,18	3,47		$2,09\times 10^3$	121	-929	6,86	3,29
$v_{11\max}$	$2,39\times 10^3$	118	-949	7,04	3,84		$2,42\times 10^3$	112	-895	7,45	3,55
$v_{12\min}$	-5,67	-0,655	3,59	1,31	3,22		-5,66	-0,650	3,58	0,89	3,73
$v_{12\max}$	-5,62	-0,658	3,28	1,06	3,34		-5,61	-0,651	3,31	0,78	3,76
$v_{13\min}$	0,0117	0,00157	-0,0125	3,26	3,65		0,0118	0,00158	-0,0125	3,44	3,65
$v_{13\max}$	0,0117	0,00157	-0,0124	3,31	3,58		0,0118	0,00158	-0,0125	3,48	3,59
$v_{14\min}$	$-2,31\times 10^{-6}$	$-7,60\times 10^{-7}$	$2,48\times 10^{-5}$	4,94	3,80		$-2,59\times 10^{-6}$	$-7,99\times 10^{-7}$	$2,54\times 10^{-5}$	4,95	3,72
$v_{14\max}$	$-2,24\times 10^{-6}$	$-7,56\times 10^{-7}$	$2,48\times 10^{-5}$	4,89	3,80		$-2,52\times 10^{-6}$	$-7,93\times 10^{-7}$	$2,53\times 10^{-5}$	4,92	3,74
$v_{15\min}$	$1,74\times 10^{-9}$	$-2,22\times 10^{-10}$	$-1,69\times 10^{-8}$	5,12	4,39		$1,87\times 10^{-9}$	$-1,98\times 10^{-10}$	$-1,71\times 10^{-8}$	5,12	4,24
$v_{15\max}$	$1,75\times 10^{-9}$	$-2,26\times 10^{-10}$	$-1,69\times 10^{-8}$	5,18	4,40		$1,86\times 10^{-9}$	$-2,01\times 10^{-10}$	$-1,70\times 10^{-8}$	5,14	4,27
$v_{21\min}$	84,8	-5,77	370	4,81	3,36		85,9	-5,86	369	4,82	3,30
$v_{21\max}$	87,3	-5,90	377	4,59	3,39		87,0	-5,88	372	4,68	3,30
$v_{22\min}$	3,41	0,0787	-0,520	6,87	1,09		3,42	0,0790	-0,529	6,88	1,06
$v_{22\max}$	3,41	0,0785	-0,523	6,84	1,09		3,42	0,0787	-0,532	6,86	1,09
$v_{23\min}$	-0,00332	$-1,49\times 10^{-4}$	0,00185	7,02	0,607		$-3,33\times 10^{-3}$	$-1,49\times 10^{-4}$	0,00186	7,04	0,602

$v_{23\max}$	-0,00331	$-1,49 \times 10^{-4}$	0,00185	7,02	0,611	$-3,32 \times 10^{-3}$	$-1,50 \times 10^{-4}$	0,00186	7,04	0,601
$v_{24\min}$	$-2,68 \times 10^{-6}$	$-8,88 \times 10^{-8}$	$-2,71 \times 10^{-6}$	7,04	0,4685	$-2,69 \times 10^{-6}$	$-9,00 \times 10^{-8}$	$-2,71 \times 10^{-6}$	7,05	0,464
$v_{24\max}$	$-2,68 \times 10^{-6}$	$-8,81 \times 10^{-8}$	$-2,71 \times 10^{-6}$	7,04	0,472	$-2,68 \times 10^{-6}$	$-8,93 \times 10^{-8}$	$-2,71 \times 10^{-6}$	7,05	0,465
$v_{25\min}$	$2,33 \times 10^{-9}$	$1,49 \times 10^{-10}$	$1,20 \times 10^{-9}$	7,04	0,364	$2,34 \times 10^{-9}$	$1,50 \times 10^{-10}$	$1,19 \times 10^{-9}$	7,05	0,356
$v_{25\max}$	$2,32 \times 10^{-9}$	$1,49 \times 10^{-10}$	$1,20 \times 10^{-9}$	7,05	0,367	$2,33 \times 10^{-9}$	$1,50 \times 10^{-10}$	$1,20 \times 10^{-9}$	7,04	0,362
$v_{31\min}$	0,760	-0,0180	-0,273	11,3	5,39	0,787	-0,0180	-0,304	14,5	5,61
$v_{31\max}$	0,923	-0,0296	-0,428	9,66	4,00	0,814	-0,0248	-0,311	10,6	3,61
$v_{32\min}$	0,00206	$6,17 \times 10^{-5}$	0,00178	7,55	3,93	0,00214	$4,99 \times 10^{-5}$	0,00143	8,10	3,46
$v_{32\max}$	$8,44 \times 10^{-4}$	$1,34 \times 10^{-4}$	0,00181	9,26	2,44	$6,65 \times 10^{-4}$	$1,35 \times 10^{-4}$	0,00184	9,29	2,39
$v_{33\min}$	$-5,96 \times 10^{-6}$	$-1,48 \times 10^{-7}$	$-4,13 \times 10^{-6}$	7,53	4,39	$-6,05 \times 10^{-6}$	$-1,36 \times 10^{-7}$	$-3,94 \times 10^{-6}$	7,83	4,34
$v_{33\max}$	$-3,91 \times 10^{-6}$	$-2,88 \times 10^{-7}$	$-2,49 \times 10^{-6}$	9,74	1,49	$-3,80 \times 10^{-6}$	$-2,92 \times 10^{-7}$	$-2,58 \times 10^{-6}$	9,67	1,38
$v_{34\min}$	$6,46 \times 10^{-9}$	$-9,28 \times 10^{-12}$	$1,74 \times 10^{-9}$	23,6	1,67	$6,68 \times 10^{-9}$	$1,09 \times 10^{-12}$	$1,58 \times 10^{-9}$	22,7	1,99
$v_{34\max}$	$1,99 \times 10^{-9}$	$3,57 \times 10^{-10}$	$2,95 \times 10^{-9}$	10,4	1,94	$2,75 \times 10^{-9}$	$3,35 \times 10^{-10}$	$2,31 \times 10^{-9}$	10,3	1,37
$v_{35\min}$	$-3,21 \times 10^{-12}$	$5,46 \times 10^{-14}$	$9,21 \times 10^{-13}$	7,54	2,66	$-3,10 \times 10^{-12}$	$3,80 \times 10^{-14}$	$7,46 \times 10^{-13}$	7,85	2,00
$v_{35\max}$	$-1,78 \times 10^{-12}$	$-3,17 \times 10^{-14}$	$4,79 \times 10^{-13}$	4,21	0,747	$-1,81 \times 10^{-12}$	$-4,17 \times 10^{-14}$	$4,63 \times 10^{-13}$	4,54	0,479
Parameter	h_{i1}	$h_{i2} \text{ (GV}^{-1}\text{)}$	h_{i3}	$h_{i4} \text{ (GV)}$	$h_{i5} \text{ (GV)}$	h_{i1}	$h_{i2} \text{ (GV}^{-1}\text{)}$	h_{i3}	$h_{i4} \text{ (GV)}$	$h_{i5} \text{ (GV)}$
g_5	0,506	0,0130	-0,394	4,12	1,33	0,565	0,0121	-0,357	4,73	1,46
$g_6 \text{ (cm}^2\text{g}^{-1}\text{)}$	$1,39 \times 10^{-4}$	$6,95 \times 10^{-6}$	$7,47 \times 10^{-4}$	3,72	1,97	$8,80 \times 10^{-5}$	$-3,89 \times 10^{-6}$	$4,91 \times 10^{-4}$	4,51	1,72

The atmospheric muon spectra for arbitrary solar conditions can be estimated following the same calculation procedures of Φ_N . For muons, the numerical values of the parameters h_{5j} and h_{6j} in Eq. (3.21) for determining g_5 and g_6 in Eq. (3.25) were obtained from the least-squares fitting of the Monte Carlo-obtained energy-integrated for all force field potentials 400, 600, 900, 1200 and 1800 MV. The results of these least-squares fittings are summarized in table 3.9.

3.2 Cosmic ray dosimetry in the atmosphere

As what we have seen above cosmic radiation interacts with the molecules in atmosphere to create secondary particles, including photon, muons, pions electrons, protons, helium ions and neutrons. However, most of these particles will be absorbed or self decayed as penetrating deeper into the atmosphere. The energies of the particles will be reduced when approaching the ground, thus flying , especially at high altitudes, can expose aircrews to still greater doses of cosmic radiation than those at ground level.

3.2.1 Fluence to dose conversion coefficients

Ambient dose equivalent and effective dose are obtained by multiplying the fluence spectra by the energy dependent conversion coefficients of PARMA model. In the case of effective dose they were based on the radiation weighting factors recommended in ICRP publication 103 [21] and specific phantoms approximating the male and female bodies. Calculations were performed for fully isotropic radiation incidence, from semi-isotropic radiation source and with broad parallel beams with the following directions of incidence: anterior-posterior, posterior-anterior, right lateral, from the top and from the bottom. The medium between the source and phantom was assumed to be vacuum.

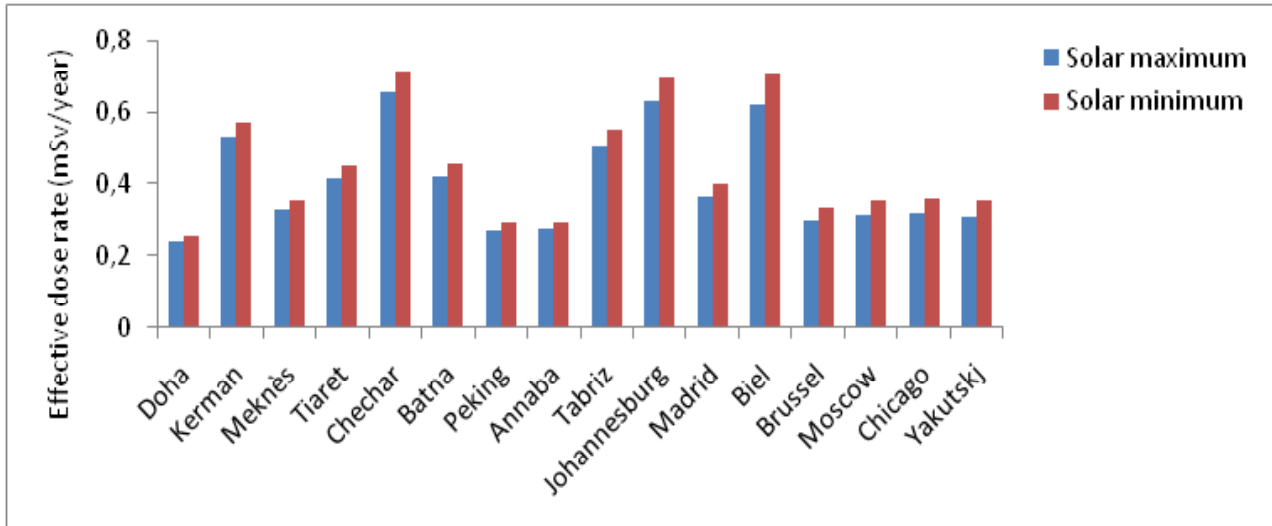


Figure 3.5: Effective dose rate of different places for solar minimum and maximum conditions at ground level.

In computing ambient dose equivalent the conversion coefficients were derived using the radiation quality factors, $Q(L)$, and the ICRU sphere defined in section 2.3.3. Thus, the geometry of the problem was very simple. The sphere was exposed to a parallel particle beam uniformly expanded over its front surface.

For aircrew dosimetry, the conversion coefficients for irradiation geometries closely representing the geometrical situations of aircrew exposure agree better with the corresponding data for the isotropic irradiation than the others.

3.2.2 Cosmic ray dosimetry at ground level

Cosmic radiation at ground level consists of a mixture of many different types of radiation, including muons, neutrons, electrons, positrons, photons, protons..., however the most of the dose comes from muons and neutrons. In figure 3.5 we calculate the total effective dose rate for a number of places from both south and north hemi sphere. The calculation were made for maximum and minimum solar activity. The altitude of these places extends from 18 m (Doha) to 2000 m (Chechar). The annual effective dose don't change greatly between

the solar maximum and solar minimum conditions and its average value for these places is about 0.41 mSv. It is roughly equal to the worldwide average dose (~ 0.4 mSv).

Most people live at low altitudes, and thus exposed to similar annual dose from cosmic radiation (apart from some variation with latitude), however there are some significant population centres at considerable altitude as Lhasa in Himalaya (~ 3.65 km) and La Paz in Andes (~ 3.95 km) where residents may receive an annual effective dose several times higher than those people living at sea level. The annual effective dose value for La Paz, for example, is four times the global average dose. There are also contribution from other natural sources of radiation in the ground such as: the radiation emitted from the soil and the construction materials that come from the ground (~ 0.46 mSv), Radon gas (~ 1.2 mSv), internal irradiation, mainly Potassium-40, (~ 0.3 mSv). The annual doses due to artificial sources are approximately 0.4 mSv from medical X-rays, 0.006 mSv from Atmospheric nuclear testing, and 0.008 mSv for the public from nuclear power industry. The percentage of the average annual radiation exposure contributed by each major source is illustrated in Figure 3.6.

3.2.3 Cosmic ray dosimetry at high altitude

The intensity of cosmic radiation increases with increasing altitude and varies with the geomagnetic coordinates (longitude and latitude) being larger towards the poles and smaller near the equator. It also depends on the solar activity, which has an alternating 11 cycle. Figure 3.7 shows a calculation of ambient dose equivalent rate as a function of flight altitudes. The calculations were made for conditions close to the solar maximum activity in December 1999 and close to the solar minimum activity in December 2009, both for the equatorial and polar regions. The Ambient equivalent dose rate at pole regions is several times higher than on equatorial ones especially on the high altitudes. This is because of

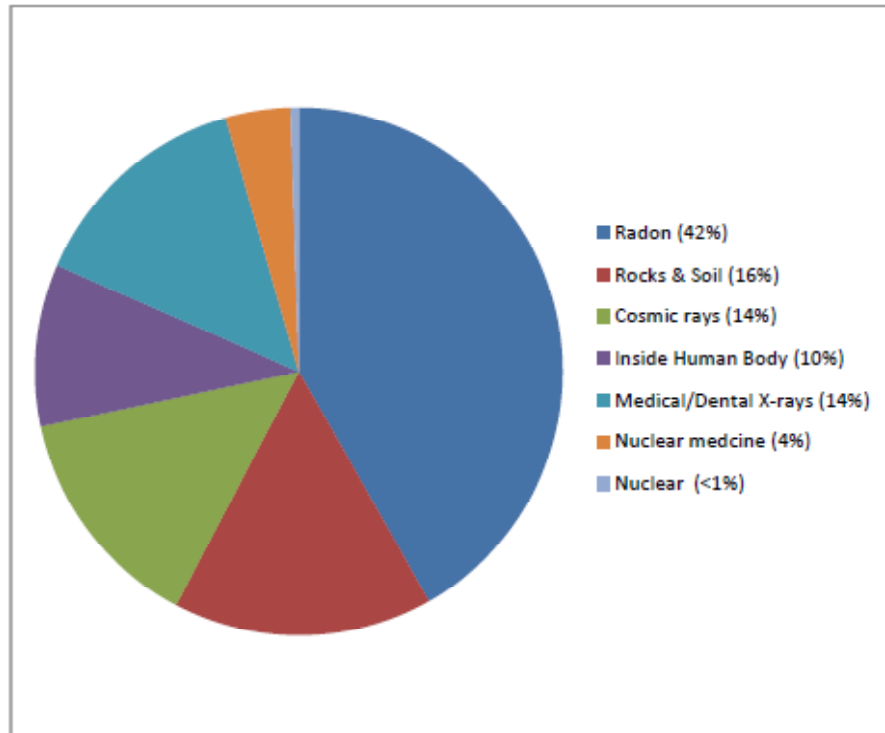


Figure 3.6: Average yearly Exposure to Ionizing Radiation.

the shielding ability of the magnetic field which is most efficient over the equator and least efficient over the poles. The difference between the solar minimum and solar maximum conditions in the poles is due to the sun's magnetic field which deflects the low cosmic rays away from the Earth.

Flying into high altitudes can expose aircrews (and passengers) to levels of cosmic radiation many times greater than they would receive on sea level. For example, for an altitude of 10 km the cosmic radiation dose is about 60 times greater than at sea level and on Concorde, which flies at 18 km, the effective dose rate is about twice as high as on subsonic planes. Figure 3.8 shows the effective dose rates as a function of altitudes calculated for 2010 using our program.

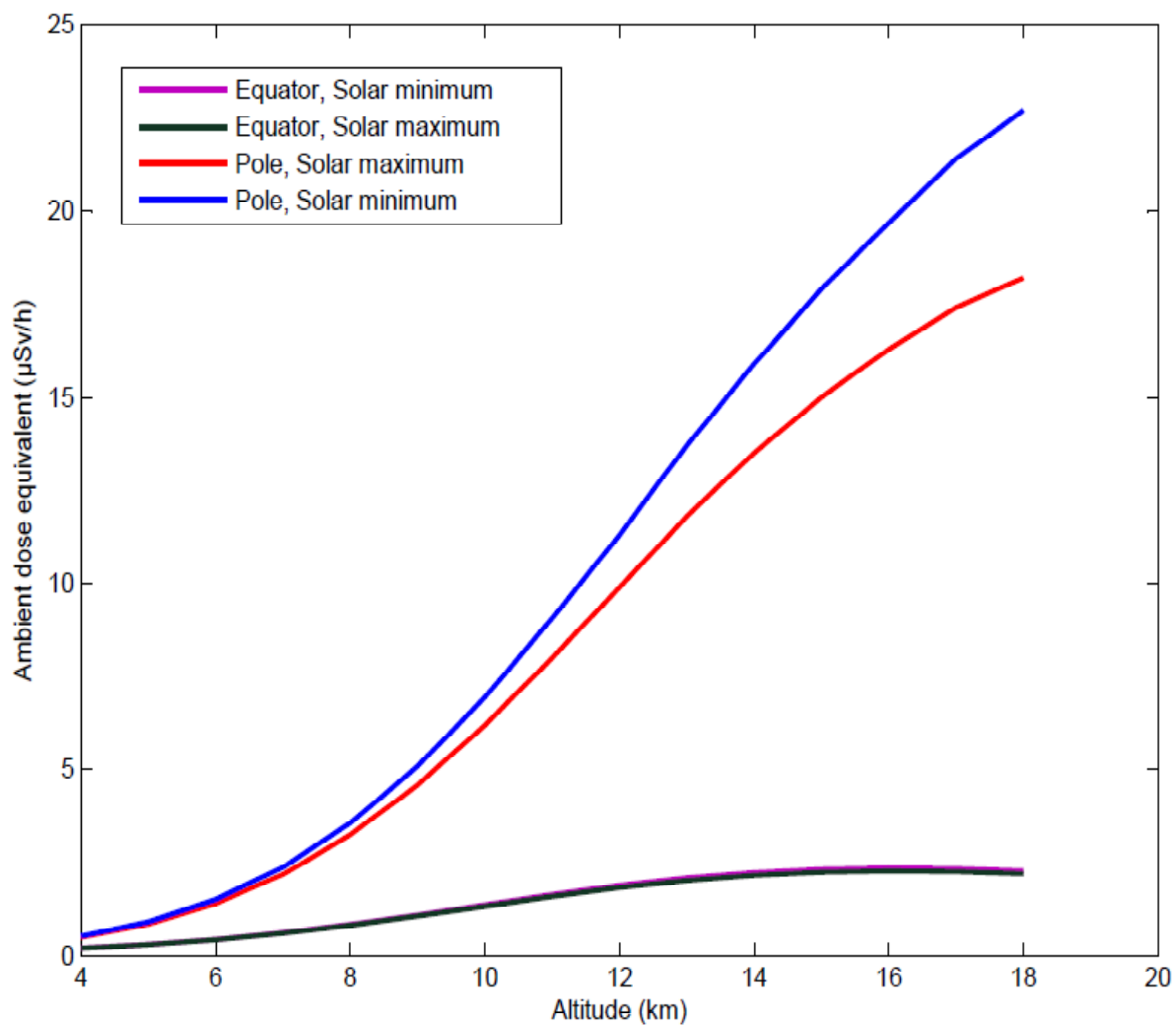


Figure 3.7: Calculated ambient dose equivalent rate, $dH^*(10)/dt$, for conditions close to solar maximum activity (December.1999) and close to solar minimum (December. 2009), both at equator and pole regions.

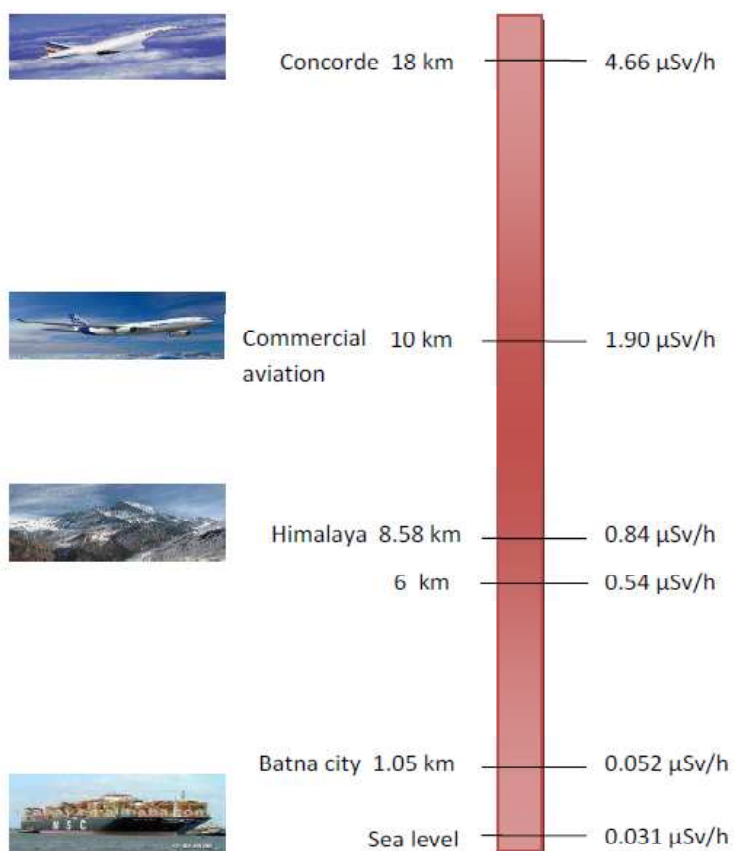


Figure 3.8: Effective dose rate as a function of altitude.

3.2.4 Comparison between the experimental and calculated data

Measurement of cosmic radiation doses have been carried out by many laboratories in the world, especially EURADOS, the European radiation dosimetry group, which is a network of more than 50 laboratories and more than 200 scientists from 31 European countries. It was established in September 1981 at Humburg (Germany) to advance the scientific understanding and to promote the technical development of dosimetry of ionizing radiation in the field of radiation protection, radiology, radiation therapy and medical diagnosis by the stimulation of collaboration between European laboratories, in particular those of the European communities. EURADOS is interested in various themes such as: dosimetry of ionizing radiation, radiation in the environment, internal and external dosimetry, the basic principles of dosimetry, radiobiological dosimetry, radiation physics in medicine, cosmic rays and control of aircrew protection against ionizing radiation. The work of EURADOS is done through working groups which are established to perform specific tasks and are usually dissolved after these tasks have been fulfilled. For the purpose of studying cosmic radiation dosimetry onboard aircraft a working group 5 was formed. The objective of this latter is to bring together all recent, available, preferably published, experimental data and results of calculations, with detailed descriptions of methods of measurements and calculation, in particular from European research groups. In this section we compare some of their data with our results under the same flight (altitude, longitude, latitude, and time) conditions.

Figures 3.9, 3.10 and 3.11 show the ambient dose equivalent rate as a function of the vertical cut off rigidity for different flight levels. Figures 3.12 and 3.13 show the ambient dose equivalent rate versus the altitude for ranges of vertical cut off rigidity of $r_c \leq 2$ GV and $r_c \geq 12$ GV respectively. The regions of $r_c \leq 2$ GV characterize the polar regions and

$r_c \geq 12$ GV the equatorial region. The in-flight measurements were reported for various instruments. Table 3.10 shows some of the instruments used from Working group 5 with their abbreviations and the measurement integration time. The calculations have been made for conditions close to solar maximum ($s = 1589.7$ MV) and solar minimum ($s = 391.7$ MV) activities between May 1992 and April 2003. The ambient dose equivalent rate is several times higher at the pole regions than on the equatorial one especially on the high altitudes. This is because of the shielding effect of the Earth's magnetic field and the absorption processes which dominate at the lower altitudes. The difference between solar minimum and solar maximum conditions is due to the Sun's magnetic field which deflects the low cosmic radiation away from the Earth.

Figure 3.14 compares the neutron ambient dose equivalent rate calculated by our program and the one measured by Kawatari et al., [32] on the mountain of Fujiyama by means of a Bonner multi-sphere neutron spectrometer in 2 September 2002. The graph shows that the altitude cosmic neutron variation shows the exponential increment as a function of the atmospheric altitude.

The comparison between the measured and calculated dose rate values shows a good agreement except some differences. The measurements are made at many various dates and the sun has daily variations in its activity. They are not taken into account by our program for calculation of dose rate. Such variations may increase the dose rate (at least 10%). The difference of the aircraft fabric from one to another influence on the shielding effect and is another explanation for differences. The ambient dose rate values in figures 3.12 and 3.13 are calculated for $r_c = 2$ GV and $r_c = 12$ GV respectively while the measured one are taken for regions of $r_c \leq 2$ GV and $r_c \geq 12$ GV respectively.

Table 3.10: List of dose assessment methods during in-flight investigations.

Abbreviation	Dose assessment method	Measurement intervals
TEPC	Tissue Equivalent Proportional Counter	25 min
NM+IC	Combined neutron monitor (NM) LB6411 and ionization chamber (IC)	5 min
NMX+Halle	Combined neutron monitor NE-NM2 with lead converter(NMX) and low level scintillation detector	6 min
NMX+IC	Combined neutron monitor NE-NM2 with lead converter (NMX) and ionization chamber	5 - 20 min

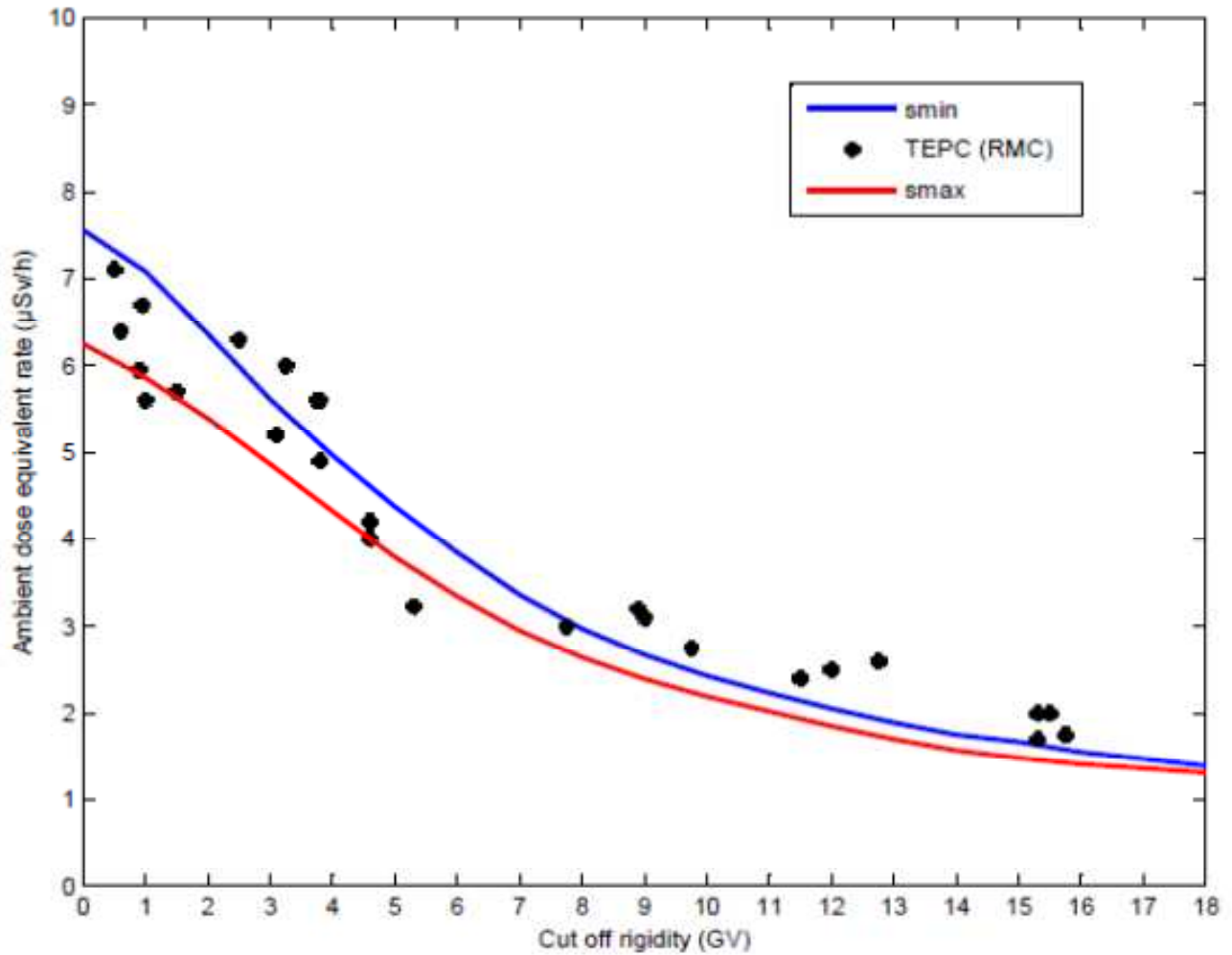


Figure 3.9: Ambient dose equivalent rate as a function of vertical cut off rigidity r_c between May 1992 and May 2003 for altitude 10668 m.

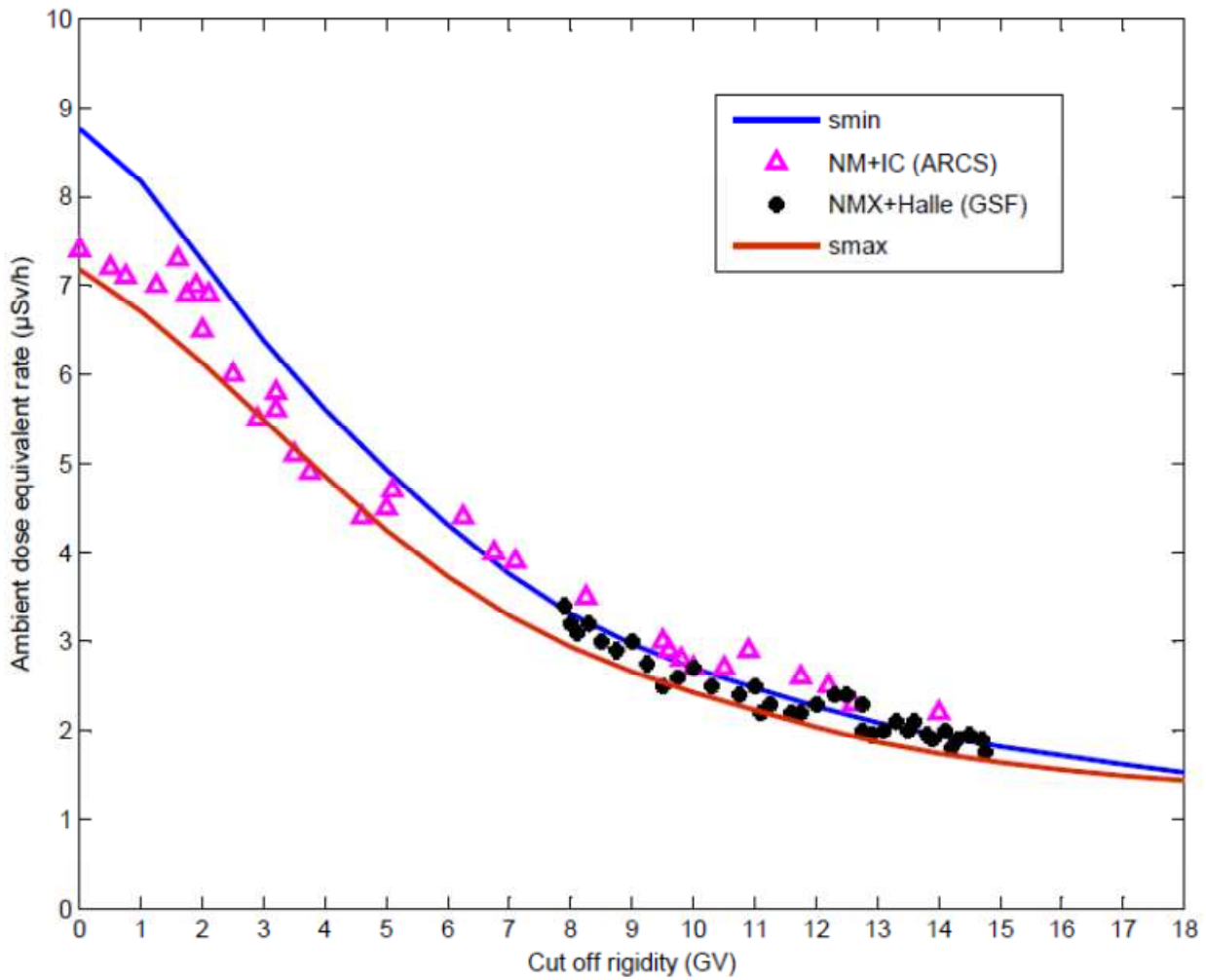


Figure 3.10: Ambient dose equivalent rate as a function of vertical cut off rigidity r_c between May 1992 and May 2003 for altitude 11277 m.

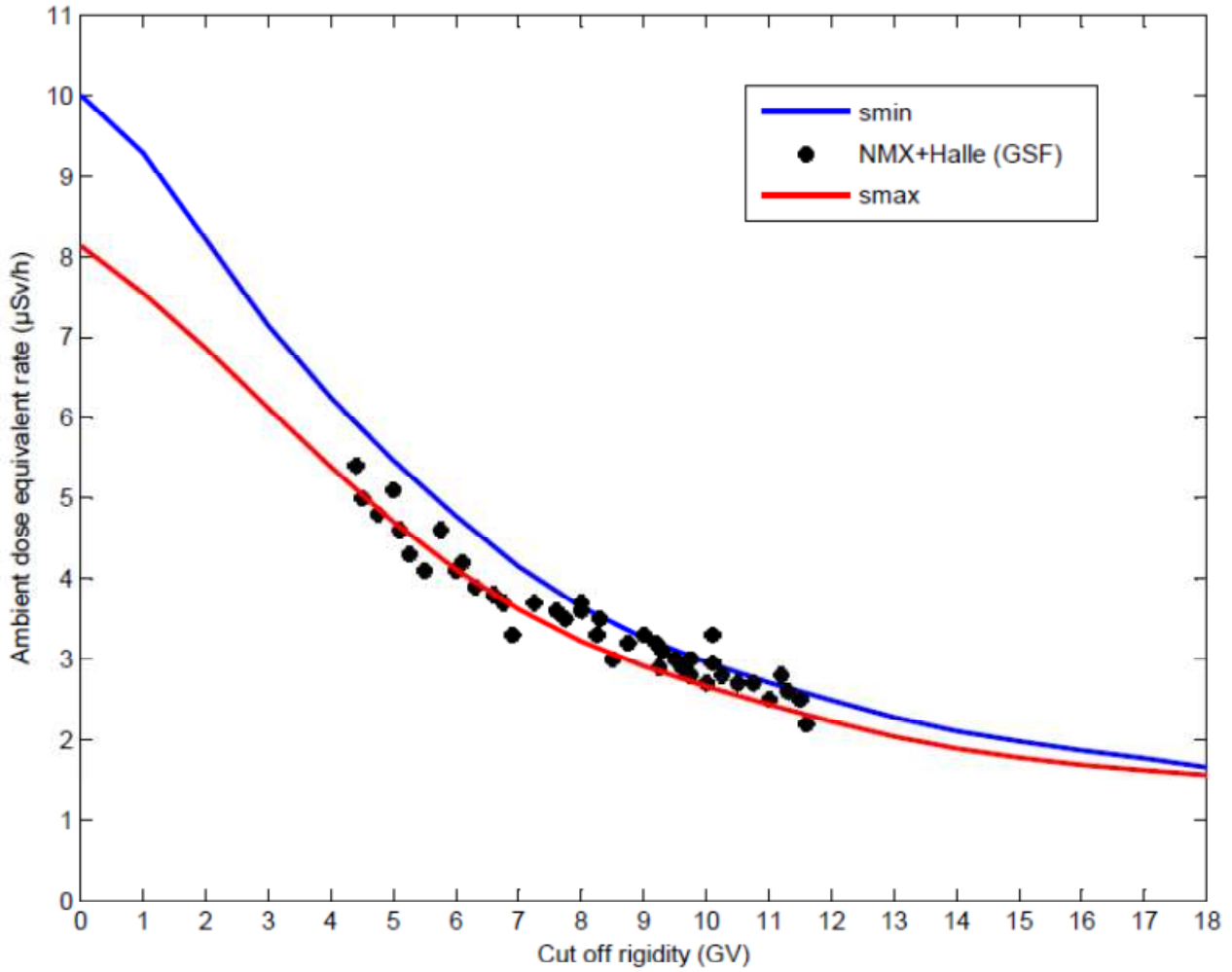


Figure 3.11: Ambient dose equivalent rate as a function of vertical cut off rigidity r_c between May 1992 and May 2003 for altitude 11887 m.

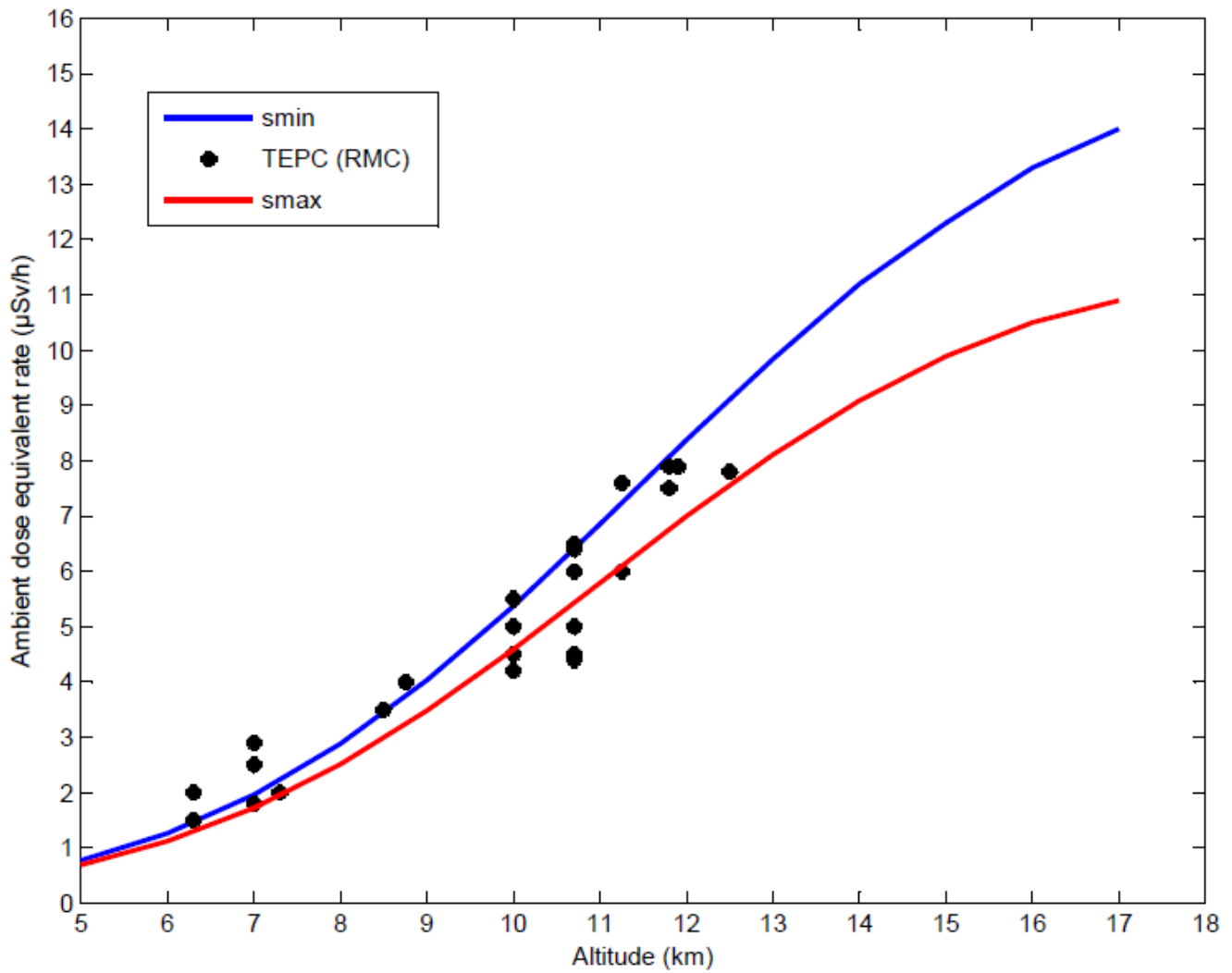


Figure 3.12: Ambient dose equivalent rate as a function of altitude d between May 1992 and May 2003 for vertical cut off rigidity $r_c \leq 2$ GV.

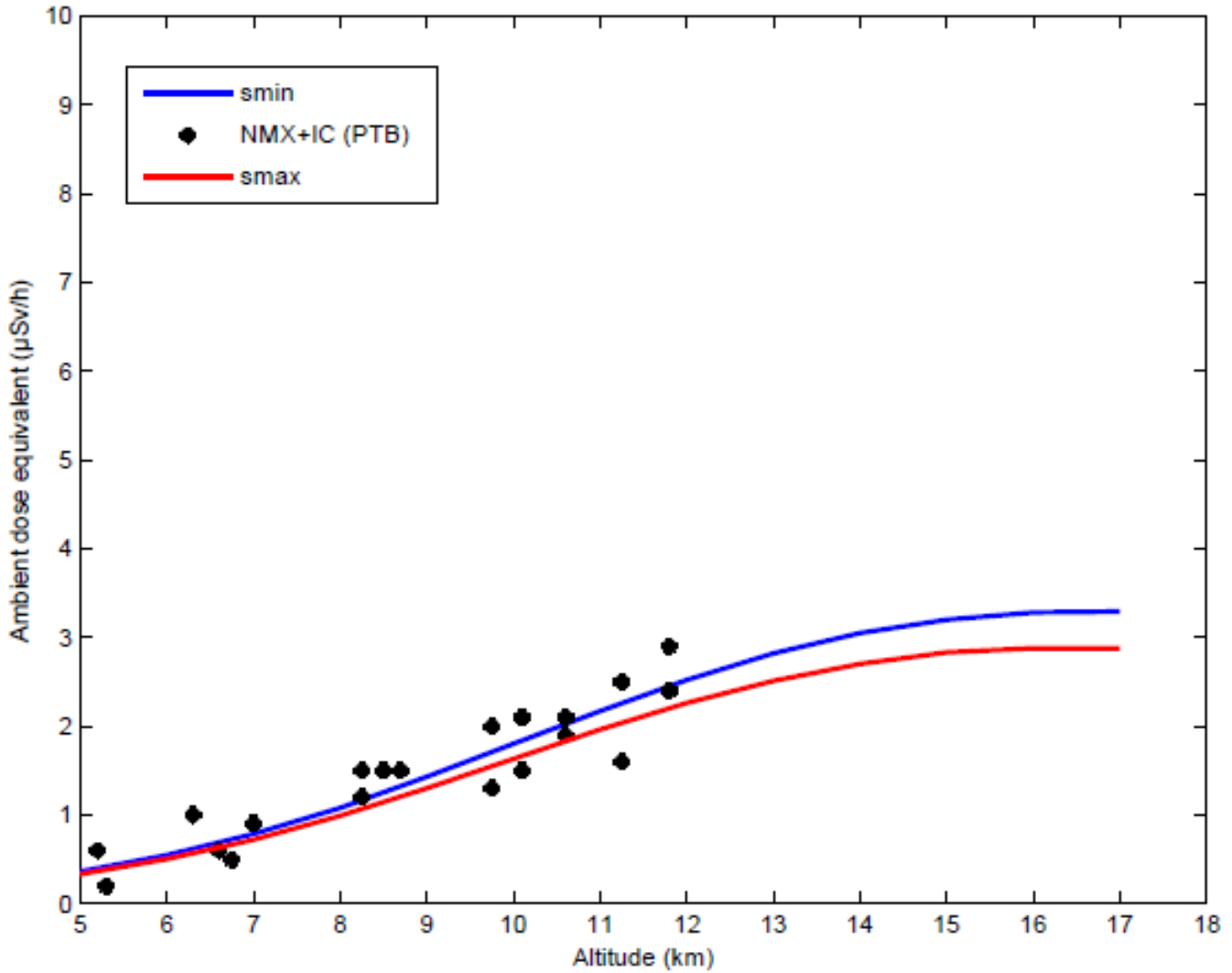


Figure 3.13: Ambient dose equivalent rate as a function of altitude d between May 1992 and May 2003 for vertical cut off rigidity $r_c \geq 12$ GV.

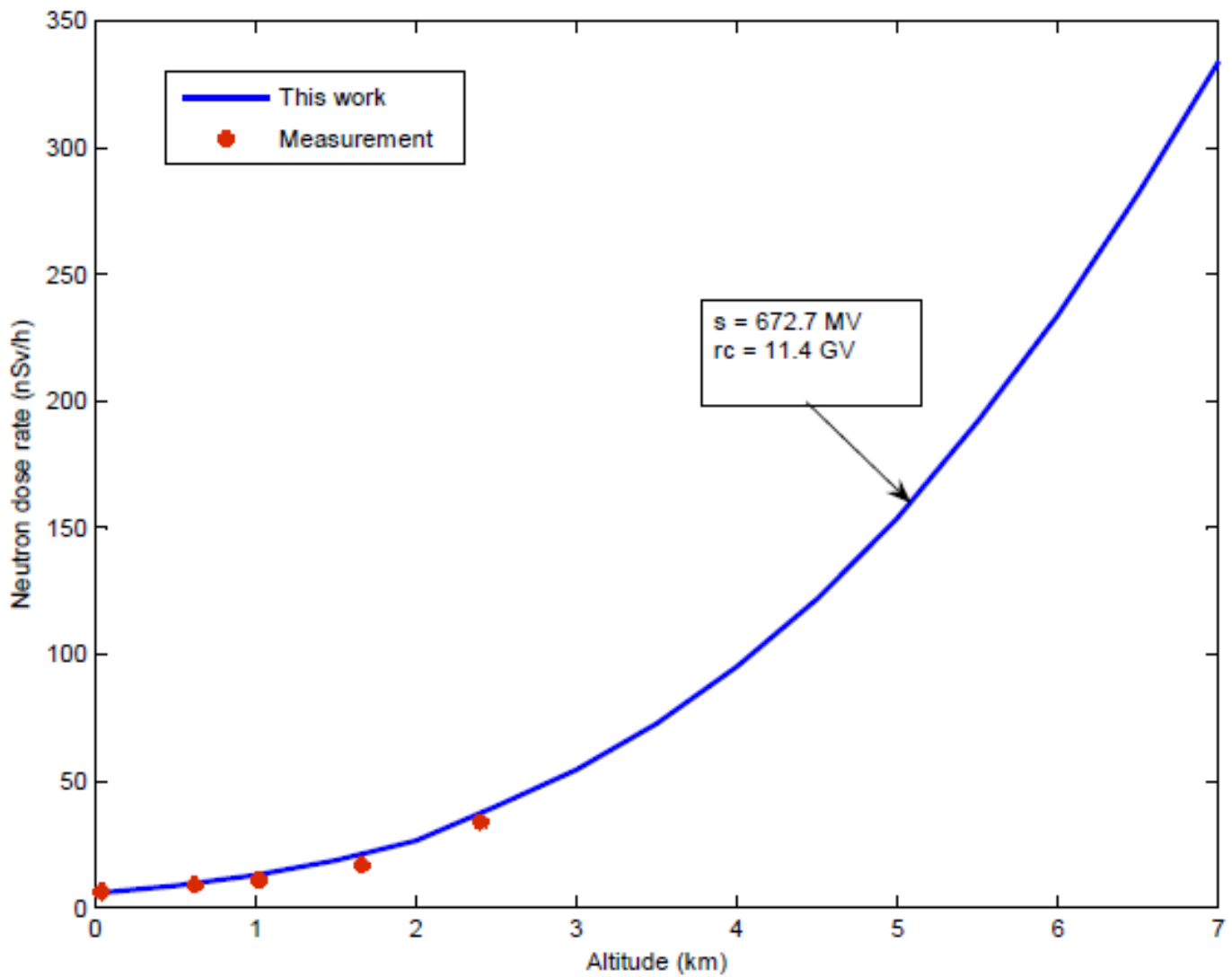


Figure 3.14: Ambient neutron dose equivalent rate as a function of altitude d in comparison with measured data of Kawatari et al.

Conclusion

The assessment of exposure to cosmic radiation in aircraft altitudes is one of the preoccupations of international organizations responsible for radiation protection. Several research programs have been established for the estimation of the natural exposure to ionizing radiation at aircraft altitudes.

The flux of cosmic rays in the atmosphere depends on three parameters. It increases with increasing altitude and varies with the cut-off rigidity of the Earth's magnetosphere being larger towards the poles and smaller near the equator. It also depends on the phase of solar activity (11-year cycle).

In our work, we have calculated the cosmic ray spectra of neutrons, protons, helium ions, electrons, positrons, photons, and muons then we have determined the doses induced by cosmic rays at any time and location in the atmosphere using the conversion coefficients from fluence to dose of PARMA model.

The annual effective dose rate of cosmic radiation at ground level is mainly from muons and neutrons and its value is about 0.041 mSv, which is roughly equal to the worldwide average dose. At high altitudes the radiation levels becomes larger than they would received on sea level. For commercial aircraft altitudes (~ 10 km), the cosmic radiation dose rate is about 60 times greater than at sea level and on Concorde altitude (~ 18 km), it is about twice as high as on subsonic level.

On the whole there is good agreement between our results and the experimental data. This gives support to the approach of basing determinations of effective dose rate for aircrew on theoretical calculations.

The developed program in this thesis can form the basis for future work consisting the calculation of the absorbed dose during a flight between two given airports.

Bibliography

- [1] J. Blümer *et al.*, Prog. Part. Nucl. Phys. **63**, 293 (2009) .
- [2] C. Grupen, *Astroparticle Physics*, Springer (2005).
- [3] M. Unger, in *Proc. 21st Int. European Cosmic Ray Symp.*, Kosice, SK (2008).
- [4] J. Cronin, T.K. Gaisser, and S.P. Swordy, Sci. Amer. **276**, 44 (1997)
- [5] C. AMSLER *et al.*, Phys. Lett. **B667**, 1 (2008).
- [6] Agasa Collaboration, <http://www-akeno.icrr.u-tokyo.ac.jp/AGASA/>.
- [7] Pierre Auger Collaboration, Sci. J. **318**, 938 (2007).
- [8] P. Bhattacharjee and G. Sigl, Phys. Rep. **327**, 109 (2000).
- [9] R. Diehl, Eur. Phys. J. **D55**, 509 (2009).
- [10] <http://hubblesite.org/>
- [11] <http://chandra.harvard.edu/>
- [12] E. Mocchiutti, Ph.D.Thesis, Stockholm University (2003).
- [13] A. Putze, Master thesis, Joseph Fourier University at Grenoble (2006).
- [14] G. Lefeuvre, Ph.D. Thesis, Université Paris 7 (2006).
- [15] G. Maurin, Ph.D. Thesis, Université Paris 7 (2005).
- [16] P. Colin, Ph.D. Thesis, Université Joseph Fourier de Grenoble (2005).
- [17] Pierre Auger Observatory, [<http://www.auger.org/>].
- [18] M. G. Stabin, *Fundamentals of Nuclear Medicine Dosimetry*, Springer (2008).
- [19] J. E. Turner, *Atoms, Radiation, and Radiation Protection*, Wiley (2007).
- [20] D. Blanc, *Les rayonnements ionisations: detection, dosimétrie, spectrométrie*. Masson (1997).
- [21] ICRP Publication 103, *The 2007 Recommendations of the International Commission on Radiological Protection, Annals of ICRP*, Elsevier (2007).

- [22] C. Wernli, *11th Int. Radiation Protection Cong.*, Madrid (2004).
- [23] International Atomic Energy Agency, *Calibration of Radiation Protection Monitoring Instrument*, IAEA (2000).
- [24] G. RAJAN and J. IZEWSKA, *Radiation oncology physics*, IAEA (2005).
- [25] M. R. Komor, *Radiat. Safety. Management.* **2**, 1347 (2003).
- [26] B. L. Justus *et al.*, *The measurement, Instrumentation and Sensors*, CRC Press LLC (1999).
- [27] C. K. Ross and N. V. Klassen, *Phys. Med. Biol.* **41**, 1 (1996).
- [28] T. Sato *et al.*, *Radiat. Res.* **170**, 244 (2008).
- [29] T. Sato and K. Niita, *Radiat. Res.* **166**, 544 (2006).
- [30] H. Iwase, K. Niita and T. Nakamura, *Nucl. J.* **39**, 1142 (2002)
- [31] R. A. Nymmik *et al.*, , *Nucl. Tracks. Radiat. Meas.* **20**, 427 (1992).
- [32] M. Kowatari *et al.*, *J. Nucl. Sci. Technol.* **42**, 495 (2005).

Abstract

Radiation levels at aircraft cruising altitudes are many times higher than at sea level. Thus, on average, a typical airline pilot receives a larger annual radiation dose than someone working in nuclear industry. The main source of this phenomenon comes from galactic cosmic rays, highly energetic charged particles created essentially by exploding stars within our own galaxy. This work aims to calculate the cosmic ray energy spectra in the atmosphere with the help of the analytical functions of the PARMA model, and then to estimate the doses induced by these particles in any location in the atmosphere using the fluence to dose conversion coefficients. The comparison of the obtained results with experimental data shows a good agreement.

Keywords: Cosmic rays; Dosimetry; Dose rate at aviation altitudes.

Résumé

Les niveaux de rayonnement aux altitudes de croisière des avions sont plusieurs fois supérieurs qu'au niveau de la mer. Ainsi, un pilote de ligne typique reçoit en moyenne une dose annuelle de rayonnement plus grande qu'une personne travaillant dans l'industrie nucléaire. La principale source de ce phénomène se trouve dans les rayons cosmiques galactiques, particules chargées très énergétiques créées essentiellement dans les explosions d'étoiles de notre galaxie. L'objectif principal de ce travail est de calculer les spectres d'énergie des rayons cosmiques dans l'atmosphère grâce aux fonctions analytiques du modèle PARMA, et estimer ensuite les doses induites par ces particules à n'importe quelle position dans l'atmosphère en utilisant les coefficients de conversion fluence-dose. La comparaison des résultats obtenus avec les données expérimentales montre un bon accord.

Mots clés : Rayons cosmiques ; Dosimétrie ; Taux de dose aux altitudes des avions.

الخلاصة

إن نسبة الإشعاع على مستوى ارتفاع الطائرات أكبر بكثير مما هو عليه على مستوى سطح البحر . هذه الجرعات المرتفعة تعني أن الطيار النموذجي يتلقى في المتوسط جرعة سنوية من الإشعاع أكبر بكثير من شخص يعمل في الصناعة النووية . المصدر الرئيسي لهذه الظاهرة يكمن في الأشعة الكونية المجرية ، و هي جسيمات مشحونة ذات طاقة عالية تتشكل في انفجار النجوم داخل مجرتنا . يهدف هذا العمل إلى حساب الأطياف الطاقية للأشعة الكونية في الغلاف الجوي بالاستعانة بالدوال التحليلية لنموذج PARMA ، ثم تقدير معدل الجرعة الناجمة عن هذه الجسيمات في أي مكان من الغلاف الجوي باستخدام معاملات التحويل من التدفق إلى الجرعة . مقارنة النتائج المحصل عليها مع النتائج التجريبية تظهر توافقا جيدا .